UNIVERSITY OF OKLAHOMA

GRADUATE COLLEGE

CHARACTERIZATION OF THERMAL PROPERTIES OF MATERIALS AND THERMAL TRANSPORT PHENOMENA USING THERMOREFLECTANCE METHOD AND FIRST PRINCIPLES STUDY

A DISSERTATION

SUBMITTED TO THE GRADUATE FACULTY

in partial fulfillment of the requirements for the

Degree of

DOCTOR OF PHILOSOPHY

By

ROSHAN SAMEER ANNAM

Norman, Oklahoma

2025

CHARACTERIZATION OF THERMAL PROPERTIES OF MATERIALS
AND THERMAL TRANSPORT PHENOMENA USING
THERMOREFLECTANCE METHOD AND FIRST PRINCIPLES STUDY

A DISSERTATION APPROVED FOR THE
SCHOOL OF AEROSPACE AND MECHANICAL ENGINEERING

BY THE COMMITTEE CONSISTING OF

Dr. Jivtesh Garg, Chair

Dr. Wilson Merchan-Merchan

Dr. Hamidreza Shabgard

Dr. Shouzhi Xu

Dr. Binbin Weng

Acknowledgments

This thesis is a culmination of the efforts of many people, who were involved and invested in my life, both personally and professionally, so please allow me to extend my acknowledge to the most important people, because of whom I am this position in my life. Firstly, I want to thank my advisor, Dr. Jivtesh Garg, who showed faith in my capability to work with complex 3D and 2D material systems using the Frequency Domain Thermoreflectance method, and also in exploring thermal transport phenomena in complex novel material systems using a first-principles study. It was an intense learning curve for both of us with constant disruptions in research progress due to the COVID-19 pandemic and various other factors beyond our control, but his faith in me never wavered and provided me with the right environment where I could flourish in my research endeavors. I admire him for his patience with me during my Ph.D. journey, and also for constantly encouraging me to be part of extra curricular activities and also for extending his support to me by recommending and nominating me for various awards in the School of Aerospace and Mechanical Engineering, and even in the Gallogly College of Engineering.

A huge thank you to my dissertation committee members Dr. Wilson Merchan-Merchan, Dr. Hamidreza Shabgard, Dr. Shuozhi Xu and Dr. Bibin Weng for committing their precious time in providing constructive comments during my Ph.D. journey. They have always been very warm and welcoming, by constantly checking in with me and making sure I was doing well and making progress toward my academic goals. Timely interactions with them have always provided me clarity in my thoughts and have been a source of renewed motivation, at the end of each interaction.

Words cannot express my gratitude for Professor Farrokh Mistree, who graciously inducted me into the Graduate Student Community, where I served in various roles, starting off as a publicity chair, and then promoting me to the position of Co-Chair in the organization. Being part of this amazing student organization provided me with countless leadership and mentorship opportunities and much-needed exposure for my professional development. I am appreciative of Dr. Ramkumar

Parthasarathy, who played a key role in pushing me to strive for excellence as a Graduate Teaching Assistant and as board member on the AME Board of Advisors, and also for nominating me for the Gallogly College of Engineering Graduate Student Pursuit of Excellence award. This award was a testament to my academic and professional activities and efforts in GCoE.

I am beyond grateful for the significant contributions made by our collaborators like Dr. Binbing Weng, Dr. Hanjong Paik, Dr. Byram Saparov, Dr. Ian Sellers (SUNY Buffalo), Dr. Joseph Ngai (UT Arlington), Dr. Fei Wang (University of Missouri) and Dr. Tribhuwan Pandey (University of Antwerp), with their important contributions in providing samples for the analysis conducted during this research endeavor and through constant support in reaching the desired research objectives. Their involvement is the reason why I am able to realize and present my thesis. A huge heartfelt thank you to my former and current lab mates Rajmohan Muthaiah, Fatema Tarannum, Swapneel Danayat, Avinash Nayal and Zarin Mona for being the most amazing support system personally and professionally. Rajmohan and Fatema were instrumental in getting me up to speed with the recent happening in the lab and helped me settle down in Norman. They wholeheartedly involved me in the projects they were working on, even delegating important tasks from their research work, helping me expand my knowledge and my skills in the field of graphene-based nanocomposites and applying first-principles computational work towards novel material discovery. Interactions with Swapneel and Avinash regarding research work in professional setting and sharing our love for sports through chatter about Cricket, Formula 1 or sports in general came as a welcome break during this journey. It is due to their enthusiasm that I started to get involved into playing Cricket again, which was an absolutely amazing stress buster. A few other people who immensely helped in my dissertation work were my dear friends Vishnu Kadiyala and Dr. Sumit Goswami, because of whom, I was able cross over a few hurdles that I incurred during my dissertation work.

Finally, I am deeply indebted to my parents Venkat Narayan Rao Annam and Raji Annam, my wife Allison Annam, and my dog-daughter Marshmallow. Their constant support for me through the best and the worst times, from differing timezones to the time lost from being apart, was influential in my commitment towards this goal of mine. This thesis dissertation document is a testament

to their sacrifices for the betterment of my career and towards my dream of securing a doctoral degree. I am pretty sure I have failed to acknowledge many more people here, but I am always thinking of them and thank them for their contributions in making my academic journey here at the University of Oklahoma, Norman, a memory of a lifetime.

Abstract

Understanding heat transport phenomena in nanoscale has gained more traction in the recent decade, especially in the last couple of years due to unprecedented innovation in the field of Artificial Intelligence and Machine Learning tools. Continuous progression of Moore's Law has led to the incorporation of billions of transistors into a smaller package as length scales decrease, but computational needs increase. This has accelerated our need to understand heat transport in nanoscale that can aid in designing efficient nano-structured and nano-engineered devices for effective thermal management or energy conversion applications.

Therefore, there is a pressing need to evaluate novel materials that can be potential candidates to meet the approaching demands of the future. Improvements in the capabilities of pump-probe measurement techniques such as Frequency Domain Thermoreflectance (FDTR) can allow accurate experimental determination of the thermal properties such as volumetric heat capacities, thermal conductivities, anisotropy, and thermal boundary conductance of novel 2D thin film and bulk materials. Additionally, the application of computational tools like Quantum ESPRESSO and ShengBTE have aided in developing insights on the effectiveness of a potential material system by evaluating its thermal transport properties. The work in this thesis will demonstrate that by establishing a high degree of agreement in the experimental and computational results, one can quantify the factors that contribute to the material's thermal properties.

Using FDTR, the bulk properties of ZnSe and ZnTe materials were measured, which demonstrated a good agreement between the results from the experimental and computational methods. Our experimentally measured thermal conductivities (17 $Wm^{-1}K^{-1}$ for ZnSe and 14 $Wm^{-1}K^{-1}$ for ZnTe) were consistent with first-principles predictions (23.2 $Wm^{-1}K^{-1}$ and 13.72 $Wm^{-1}K^{-1}$at 300 K). Computational results provided insights on the length-dependent thermal conductivity of both of the materials, further showing the effect of phonon–boundary scattering being present at modern device dimensions.

Another study involved an examination of STO thin films at varying thicknesses to show FDTR's sensitivity to nanoscale thermal transport, where a significant reduction of 93% from the bulk value was noticed for the 12 nm thin film. This indicated the consequence of boundary scattering and substrate effects. Sensitivity analysis showed the measurement to be sensitive to cross-plane thermal conductivity and volumetric heat capacity properties, which made their evaluation possible. The study illustrated the underlying mechanisms of thermal transport in the oxide perovskite thin films. It is important for understanding the thermal properties of oxide thin-film systems, especially those with silicon substrates, as they serve as an important platform for integration of these materials in microelectronic devices.

The computational study of intermetallic materials like $ReSi^{1.75}$, ReAlSi and ReGaSi becomes the first attempt to report the thermal properties of the materials through the first-principles calculations. This study develops an understanding in the thermal transport phenomena of bulk and nanoscale materials, as well as understanding their temperature dependent properties. This study was essential in proving the potential of the materials for thermoelectric applications and provides insights on how the material can be tuned for its application to developing efficient thermoelectric devices.

The final experimental chapter examined the effects of annealing of Strontium Chromate thin films under different environments — a process with limited literature due to the difficulty of computational modeling because of the strong electron correlations exhibited by the materials of this family. Measurements performed by FDTR showed that after annealing there were observable changes in thermal conductivity and heat capacity, that were consistent with observed electronic measurements that shows a transition towards metallic behavior. Further study is necessary to determine the microscopic origin of these changes but this work establishes a foundational background with regard to SCO thin films and the ability of FDTR to characterize thermally complex oxide systems grown on silicon, adding to the barely available literature.

The successful experimental analysis of STO enabled the experimental characterization of the thermal properties of Strontium Chromate (SCO) thin films on Si substrate. Here, an attempt was

made to characterize the effects of annealing environments on the thermal properties of the SCO thin films. The effects of annealing environments were quantified, along with validating the phase transition from semiconducting to metallic behavior, which was observed in the literature through electrical and structural characterizations.

Keywords: Thermal Conductivity, 2D Thin-Films Characterization, Frequency Domain Thermoreflectance Method, First-Principles Calculations, Quantum ESPRESSO, ShengBTE, Density Functional Theory, Nano-fabrication, Nanoscale Heat Transfer

Contents

List of Figures

List of Tables

Chapter 1

Introduction

Modern microelectronic performance and reliability depend heavily on thermal properties such as thermal conductivity. According to Moore's law, the number of transistors in an integrated circuit doubles every two years, causing the relevant length scales to diminish to nanometers. The material properties, in particular the thermal properties, may differ dramatically from their bulk counterparts at these nanoscale length scales, resulting in a larger than expected temperature rise in electronic devices. This phenomenon diminishes reliability and performance in microelectronics [1], increasing the attention on thermal management as an area of concern in the design of modern microelectronics [2, 3, 4, 5, 6, 7]. Low thermal conductivity can also be beneficial for applications such as thermoelectrics where lower lattice thermal conductivity minimizes heat loss through lattice vibrations, improving the energy conversion efficiency. Additionally, the heat conduction across nanoscale thin films is frequently constrained by material interfaces [8], which hinders the reliable operation of electronic devices such as developing wide-bandgap nitride material systems [9, 10], phase change memory, and heat-assisted magnetic recording.

A wide range of experimental approaches have been developed to comprehend fundamental elements of thermal transport at the nanoscale [8, 11]. These include scanning thermal microscopy (SThM), which is based on a heated atomic force microscope tip [12], 3ω method [13], and optical pump-probe methods such as Time-Domain Thermoreflectance (TDTR) [6, 14, 15] and Frequency-Domain Thermoreflectance (FDTR) [7]. All the methods mentioned above are reliable ways to understand the heat transport phenomena in the nanoscale and quantify thermal properties of micron/nanometer thin films and the resulting interfaces (as thin films need to be deposited on a substrate of choice). But all these techniques exhibit advantages and drawbacks, relative to each other's capabilities. For example, 3ω methods are one of the reliable ways to measure the cross-plane thermal conductivity of material; however, the method involves very intricate

microfabrication of electrical contacts, and subsequently loses spatial resolution, due to the size of the strip heater. In the case of SThM, the method can provide images of thermal properties with nanometer-scale spatial resolution, which is highly sensitive to sample and tip morphology. However, SThM involves complex tip fabrication.

This is where pump probe methods such as TDTR and FDTR have been gaining popularity, to measure the thermal properties for a variety of material systems such as solids [7, 14, 16, 17], liquids [18, 19], thin films [20, 21, 22], and the thermal conductance of interfaces [23, 24, 25, 26].

For several decades, photothermal and photoacoustic phenomena have been active research fields due to the need for a quick and practical method to assess thermal and electrical transport properties, particularly those of thin films that are common in contemporary integrated circuits. Today, there are several different non-contact measurement methods available that rely on how optical characteristics change with temperature. All these methods generate heat and/or measure temperature using light waves.

The development work began in 1970 with contributions from Rosencwaig and Gersho [27], Rosencwaig [28], Opsal et al. [29], and Rosencwaig et al. [30], which utilized continuous-wave (CW) light sources for the heating of the sample surface. To study nonequilibrium electron-phonon dynamics in metals, [31, 32, 33] that generate coherent phonons and to measure the heat diffusion in thin films and across the interfaces, measurement methods utilizing pico and femtosecond pulsed laser sources were developed in the 1980's. Thermoreflectance microscopy systems were also being used to develop heat dissipation maps in microelectronic devices. Pump-probe thermoreflectance methods, in recent years, have been developed by fitting them with motorized stages for imaging systems and scanning mirrors. [34]

Here, we first go through the fundamentals of TDTR and FDTR procedures. The measurement geometry used by both methods is the same as that depicted in Figs. 1.1a and 1.1c. A probe laser beam is focused on the same spot as a pump laser beam to measure the change in reflectivity while a pump laser beam creates a Gaussian-shaped heat source on the sample surface. Through the coefficient of thermoreflectance, the change in reflectivity is proportional to the change in

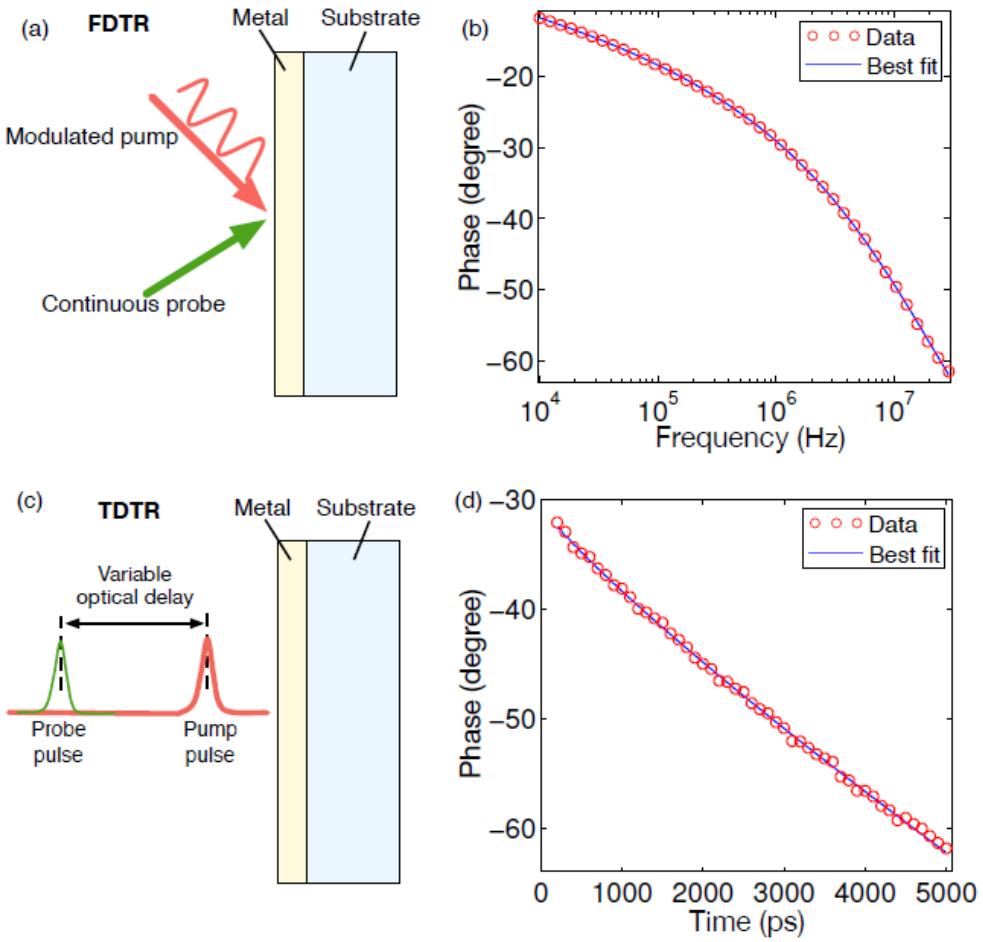

Figure 1.1: a) Schematic diagram of basic FDTR principle, b) FDTR Phase data and best fit curve, c) Schematic diagram of basic TDTR principle, d) TDTR Phase data and best fit curve.

surface temperature for minor temperature changes [35]. The sample is often covered with a thin transducer layer, such as a layer of metal, which has a high coefficient of thermoreflectance at the probe wavelength, improving system's signal to noise ratio and a substantial absorption at the pump wavelength, ensuring efficient heating of the sample surface, minimizing any losses in the system, while also aiding in improving the confidence of material property extraction. Typically, a 532 nm probe laser and an 800 nm probe laser are utilized for gold and aluminum transducers, respectively [36] [19]. In FDTR, the pump beam is modulated at various frequencies, and a lock-in amplifier is used to measure the phase delay between the pump beam and probe beam. The pump and probe beams in TDTR are separated by a configurable optical delay and originate from

a pulsed laser source. The pump pulses heat the sample, while the probe pulses measure the change in surface reflectivity as a function of time. To enable lock-in detection, the pump beam's pulse train is subjected to extra periodic modulation at one or more frequencies. The observable parameter might be the amplitude, phase, or the ratio of the in-phase to out-of-phase components of the lock-in amplifier signal.

While TDTR studies can probe frequencies up to the GHz range, FDTR experiments primarily access the frequency response of the sample in the kHz to MHz range [37]. The measurement of thermal characteristics is carried out as an inverse problem in both TDTR and FDTR by minimizing the difference between the calculated and actual probe phase or amplitude and by modifying the relevant parameters in a heat transfer model. Fig. 1.1b illustrates sample data from a typical FDTR measurement of fused silica coated with 80 nm of gold and the best heat transfer model fit, while Fig. 1.1d illustrates sample phase data and the best model fit from a TDTR measurement of fused silica coated with 70 nm of aluminum.

The capacity to resolve non-equilibrium dynamics among energy carriers, picosecond temporal precision, and for some samples, greater sensitivity to thermal interface conductance and the thermal characteristics of thin films are all benefits of TDTR [38]. In contrast, FDTR eliminates the difficulty of a mechanical delay stage and the high expense of a pulsed laser system, and with the appropriate range of modulation frequencies, FDTR provides comparable or increased sensitivity for many kinds of thin-film thermal measurements [16, 21, 25, 39, 40]. Another advantage of this experimental system is that it can reliably characterize the thermal properties of the material system under investigation, as well as providing an insight on the real-life consequences on the material properties such as interfacial properties like boundary conductance through various material tuning techniques such as doping, creating superlattice (lattice matching or mismatch) and growing on various substrates.

But, the biggest bottleneck to novel material discovery through experimental research arises from the grave difficulty to synthesize the material physically, especially the synthesis of pure single crystals and thin-film material systems on a substrate. Material synthesis involves an intense

trial and error process, through the use of expensive techniques like pulsed layer deposition (PLD) or molecular beam epitaxy (MBE), along with an extensive characterization process, implemented through a variety of complex instruments, which is not an efficient use of either time or resources. It therefore stands to reason that there must be a better way one can evaluate the material properties without having to grow these systems for experimental evaluation physically. In particular, to the expected level of confidence, while also being able to verify the potential of the material system, before experimental analysis proceeds so that we can better enhance the desired properties of the material for a specific application.

In the case of semiconductors and thermoelectrics, the approach to the design of high and low thermal conductivity materials through nano-engineering for the respective applications requires an understanding of how phonon scattering can be used to reach these desired goals. Phonon mean free path or MFP is one of those important parameters that influences the thermal conductivity of the material. MFP is defined as the product of the phonon group velocity and phonon relaxation time. The significance of a mean free path for phonon is that it determines how far it can travel without scattering. Scattering occurs when a phonon interacts with other phonon(s), or it interacts with grain boundaries at nanometer length scales, thus obstructing its free flow in the system. Therefore, if the phonon mean free path is longer, that is, in the order of 1 micron or larger, then the material will exhibit high thermal conductivity, and materials with lower mean free path exhibit lower thermal conductivity. Applying this knowledge to our material analysis can help in reducing costs involved in developing nano-engineered materials for desired applications, which can be achieved by applying first principles approach, based on density functional perturbation theory to solve the phonon Boltzmann transport equation (PBTE).

The work in this thesis is aimed at attempting to characterize thermal properties of the materials through both experimental and computational methods, where an agreement in the computational and experimental results helps us understand the thermal transport phenomena in both bulk scale and nanoscale. Chapters 2 and 3 discuss,in brief, the fundamentals of thermal analysis using FDTR and tools like Quantum ESPRESSO and ShengBTE. Chapter 4 is dedicated to applying the under-

standings from chapter 2 towards characterization of GaX (X = P, As, Sb) materials, as the analysis of a well understood and a well researched system helps us solidify our methodology of applying FDTR towards the characterization of novel materials. From our analysis, the thermal conductivity values for GaX materials (X= As, Sb, P) were 39.3±1.97 $Wm^{-1}K^{-1}$, 29.4±1.47 $Wm^{-1}K^{-1}$ and 92.7±4.64 $Wm^{-1}K^{-1}$ respectively, which are in close agreement to the values widely mentioned in the literature. In chapter 5 we look at the degree of agreement in the thermal properties from both the methods in the bulk system and extend our analysis of the system in nanometer length scales, where we estimated the length dependent thermal conductivities of ZnSe and ZnTe. We found that using FDTR, the experimentally determined thermal conductivity values of natural occurring ZnSe and ZnTe are ∼17 $Wm^{-1}K^{-1}$ and 14 $Wm^{-1}K^{-1}$ respectively. The computed results of around 23.2 $Wm^{-1}K^{-1}$ and 14.2 $Wm^{-1}K^{-1}$ for naturally occurring ZnSe and ZnTe respectively at 300K were achieved using first-principles.

Chapter 6 is dedicated towards understanding the effects of varying length scales and substrates on the thermal conductivity of Strontium Titanate thin films. We characterize thickness dependent thermal properties of STO thin films on Si substrate, with film thickness of 200 nm, 80nm, 50nm and 12nm. The thermal conductivity values for these films were 7.4±0.74 $Wm^{-1}K^{-1}$, 3.86±0.43 $Wm^{-1}K^{-1}$, 2.35±0.26 $Wm^{-1}K^{-1}$ and 0.8±0.1 $Wm^{-1}K^{-1}$ respectively, and compare these results to the STO thin films grown on STO, LSA and DSO in literature. This work was also another step in the right direction towards understanding the analysis of thermal properties using FDTR, and contributing to the understanding of heat transfer phenomena in STO thin films across length scales and substrates.

We then attempt to characterize the thermal conductivity of $ReSi_{1.75}$, ReAlSi and ReGaSi materials through our work in chapter 7. Firstly, we verify the confirmation of our results across the two different methods for ReAlSi systems, indicating that the material properties thus evaluated are true. We then extend our analysis into ReGaSi and $ReSi_{1.75}$ using Quantum ESPRESSO and ShengBTE. This work is the first attempt at doing first-principles calculations for these material systems.

We also characterize the effects of annealing on the thermal properties of Strontium Chromate thin films on a silicon substrate, by varying the amount of oxygen present in the thin film, through annealing in different environments. Annealing in different environments demonstrated a dramatic increase in the thermal conductivity values for the thin films, as compared to unannealed ones. In chapter 8, we try to understand the phenomenon of increased thermal conductivity due to annealing.

Chapter 2

Fundamentals of Frequency Domain Thermoreflectance Technique

2.1 Experimental Setup Details

The FDTR[36, 41] system setup consists of two 75mW and 20mW TEM_{00} (Transverse Electronic Modes) continuous wave free space diode lasers (Coherent OBIS) where the pump laser works at the wavelength of 473 nm and the probe laser works at a wavelength of 532 nm. The operating wavelength represents the wavelength associated with visible spectrum range. Hence the pump laser at 473 nm is a blue light laser and the 532 nm probe laser is green in color. The output power of the pump laser is modulated digitally by modulating the pump laser's driving current, with the help of output reference of the Lock-In amplifier being used (Zurich Instruments HF2LI). The driving signal used for pump laser modulation is a sinusoidal signal with a 2V peak to peak voltage and the frequencies used for the modulation range from 500 Hz to 50 MHz. The beams from these lasers pass through optical isolators (Thorlabs IO-5-532-HP for 532nm, Thorlabs IO-3-488-HP for 473 nm), which prevent any back scattering of laser beam into the aperture of the laser, which in turn protects the laser from output power instabilities.

This setup also utilizes mirrors to appropriately direct the laser beam in the desired direction. Using a beam splitter, 1% of the pump laser beam is directed towards a photodetector which records the phase of the pump beam, referred to as pump phase or φ_{pump}. A dichroic mirror (Edmund Optics, hot mirror) reflects the pump beam onto the sample through the microscopic objective. This creates a periodic heat flux on the sample's surface with spot intensity being maximum in the middle and decaying towards the edges according to a Gaussian spatial distribution. Both the pump and probe beams are aligned coaxially, and the probe beam is used to measure the change in phase of the temperature response of the surface with respect to the phase of the input heat signal. This

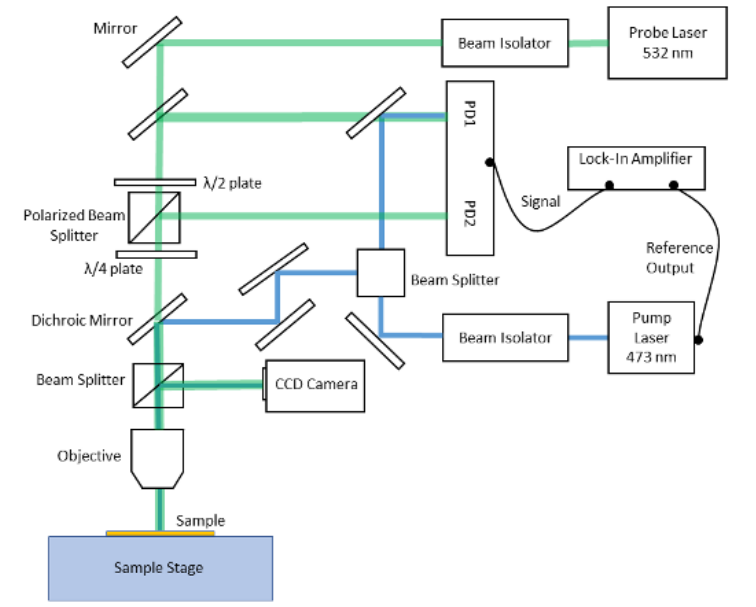

(a)

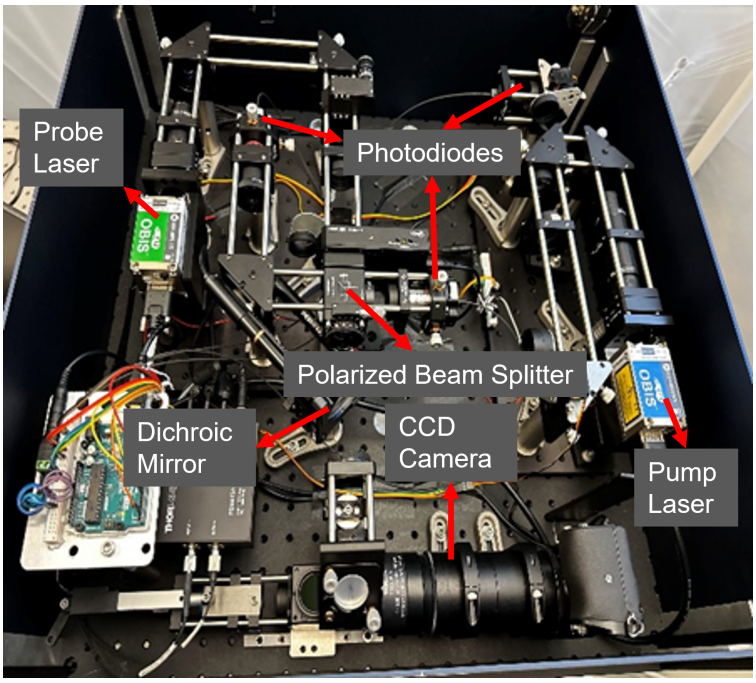

(b)

Figure 2.1: a) Frequency Domain Thermoreflectance (FDTR) experimental setup schematic and b) Experimental setup as seen in the laboratory at OU.

is achieved by measuring the surface temperature through a measurement of the intensity of the reflected probe beam (the two are correlated through the fact that surface reflectivity is a function

of surface temperature).

Every sample whose thermal properties are measured using FDTR utilizes a thin film of metal, whose thickness is in the range of 80-100 nm. The metal film maximizes the coefficient of thermoreflectance at the probe laser's operating wavelength. Balanced photodetection is implemented to improve the signal to noise ratios at the low frequencies of modulation for the pump laser. Balanced photodetector like Thorlabs PDB415A is used, as it consists of two well matched photodiodes namely, PD1 and PD 2. A polarizing beam splitter (PBS) is utilized to split the probe beam into a pre-sample beam and a post-sample beam. The pre-sample beam is reflected into PD 2 as shown in the schematic. The post-sample beam is reflected from the sample surface, reflected again using the dichroic mirror into PD 1. The optical path lengths to PD 1 and PD 2 need to be matched, to reduce the noise in the PD signal. The noise minimization is achieved by delicately balancing the pre and post sample beams, by adjusting the half-wave plate. Another way of noise rejection that has been implemented is by letting the PD 1 and PD 2 subtracted signal pass through a low noise transimpedance amplifier. This method helps eliminate noise from the probe beam, which is a common problem. To prevent the thermal signal from getting overwhelmed by the back scattering of the pump beam, two band pass filters (FGB37) are used before the photodetectors.

The measurement of FDTR in our case works by comparing the phase lag of probe beam's post-sample beam (which is measured with respect to a reference signal from the lock in amplifier) with respect to the calculated phase lag of the surface temperature of the sample surface to a periodic Gaussian heat source (pump laser) at the sample surface. It is important to note that all the components within the experimental setup along with the path lengths traversed by both the pump and probe beams, driving electronics and photodetectors are responsible for introducing a frequency-dependent phase shift to the signal which is denoted by φ_{ext}. The way this phase shift is accounted for is by sampling 1% of the pump beam and directing it into the post-sample photodetector. φ_{ext} is then measured over a range of the modulation frequencies for the pump beam and is then subtracted from the phase signal that has been measured, before fitting the measured data to a thermal model. In the setup, we also use a translation stage to adjust the sample height

which keeps the sample in sharp focus i.e., the sample is in the depth of focus of the objective lens being used. This step is of utmost importance as a sharp image of a focused sample helps in the accurate determination of the spot size, which is a vital input parameter for the thermal model. The image of the sample being focused is done by using the CCD (charge-coupled device) camera.

2.2 Spot Size Characterization

One of the primary sources of experimental uncertainty in FDTR is estimation of laser spot size [7] [39]. To measure the spot size, a two-dimensional knife edge technique is used to determine the laser spot size [36]. A knife-edge sample as shown in the Fig. 2.2 is fabricated for this purpose. This knife edge sample is then mounted on a piezoelectric sample stage, which is used to position

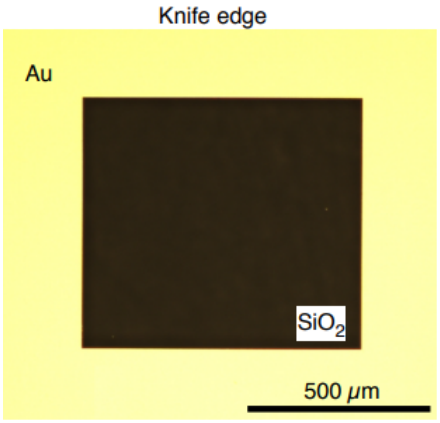

Figure 2.2: Example of knife-edge sample for spot size measurement

the knife-edge sample in the focal plane of the objective lens. The sample is then scanned in two directions, while measuring the transmitted light, by placing a photodetector underneath.

$$I(r) = \frac{2A_0}{\pi w_0} \exp\left(\frac{-2r^2}{w_0^2}\right) \tag{2.1}$$

Gaussian intensity profile of a laser spot is determined by where, A_0 is the total power and w_0 is the $\frac{1}{e^2}$ radius. The total power transmitted by the photodetector is given by

$$P(x) = \frac{2A_0}{\pi w_0} \int_{-\infty}^{\infty} dy \exp(\frac{-2y^2}{w_0^2}) \int_{-\infty}^{x} dx \exp(\frac{-2x^2}{w_0^2}) \tag{2.2}$$

when the knife edge is scanning in the x direction. We now fit the Gaussian profile with the spatial derivative of the photodetector output in x and y directions to get the pump and probe spot radius. To measure the spot size using the knife edge method, one requires a piezo stage which can move in both x and y direction. Such a stage is expensive and hence an effective way to calculate the spot size on a stationary stage needed to be introduced. This is achieved by measuring the spot size using Gaussian beam optics. The minimum spot size for both pump and probe beams are determined by $w_0 = 0.61\lambda/NA$ where λ is the operating wavelength of the laser and the NA [42] is the numerical aperture of the objective being used for the measurement. Using this information, we can calculate w_1 and w_2 for both the lasers respectively. The w_0 is the root mean squared value of w_1 and w_2 where $w_0 = \sqrt{(w_1^2 + w_2^2)/2}$.

2.3 Signal Analysis

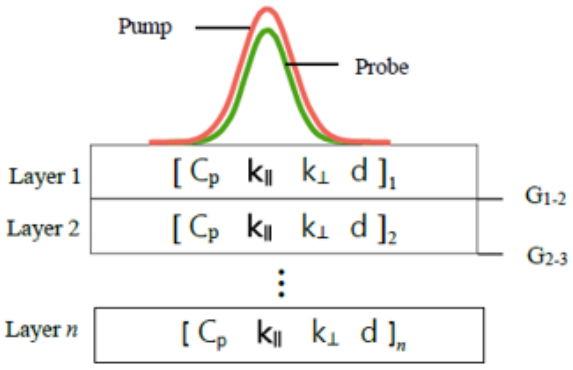

Figure 2.3: Multiple layer sample with Gaussian pump and probe spots

In FDTR, the thermal properties are measured using an inverse problem, which is done by minimizing the error between the phase lag that is measured using the current setup and the phase lag that is calculated at different frequencies of modulation, by adjusting the parameters of our

interest in a thermal model. As described in literature, the model gives us a frequency response of the surface temperature of the sample in the diffusion regime, which is the result of the sample's response to a Gaussian heat source (pump laser) on a stack of materials, comprising of multiple layers. For each layer of the sample, we utilize five physical parameters namely, the cross-plane and in-plane thermal conductivities of the layer ($k_\perp$ and $k_\parallel$), thickness of the layer, d, volumetric heat capacity, C_p and the thermal boundary conductance with respect to the next layer, *G*.

Therefore, for a sample with n layers, the number of physical parameters associated with the material system are 5*n*-1. Semi-infinite boundary condition can be considered for the bottom-most layer within the stack, if the thermal penetration depth for the material system at the lowest frequency of modulation is smaller than the thickness of the bottom layer. If not, then the actual thickness of the final layer is to be considered for the solution using the thermal model. The bottom layer can be considered adiabatic, isothermal, or convective depending on the way it is mounted.

Thermal penetration depth is given by Eq. 2.3,

$$\delta_t = \sqrt{\frac{2\alpha}{\omega_0}} \tag{2.3}$$

where ω_0 is the lowest frequency of modulations and α is the thermal diffusivity of the bottommost layer. The optical power of the pump beam which is falling on the sample surface is determined by Eq. 2.4,

$$Q_{modulation} = \frac{1}{2} Q_{pump}(1 + \cos\omega t) \tag{2.4}$$

where Q_{pump} is the maximum DC output of the pump laser. The harmonic component of the probe signal is detected by the lock-in amplifier and the frequency ω. The amplitude of the lock-in voltage is given by

$$|V_{LI}| = \frac{1}{2} Q_{pump} Q_{probe} \left(1 - R_{\lambda_{pump}}\right) \left(\frac{dR}{dT}_{\lambda_{probe}}\right) G_{\mathrm{det}} |H(\omega)| \tag{2.5}$$

where Q_{probe} is the power of the probe beam, which is hitting the sample surface, $R_{\lambda_{pump}}$ is the reflectivity of the sample surface and the co-efficient of thermoreflectance is $\frac{dR}{dT}_{\lambda_{probe}}$ at the probe wavelength. G_{det} is the product of transimpedance amplifier gain and the responsivity of the photodiode at the probe wavelength. The frequency response of the sample surface temperature to a periodic Gaussian heat flux absorbed at the sample surface, which is weighted by the intensity distribution of the probe beam, is represented by a complex number $H\left(\omega\right)$. We now derive an expression for $H\left(\omega\right)$ for the geometry depicted in Fig 2.3. In this derivation, *k* is considered to be the Henkel transform variable, which is not to be confused with the thermal conductivity for this derivation specifically. In cylindrical co-ordinates, the heat conduction for each layer of material is given by

$$\frac{\Lambda_r}{r}\frac{\partial}{\partial r}(r\frac{\partial\theta}{\partial r})+\Lambda_z\frac{\partial^2\theta}{\partial z^2}=C_p\frac{\partial\theta}{\partial t} \tag{2.6}$$

where C_p is the volumetric heat capacity, Λ_r and Λ_z is the in-plane and cross-plane thermal conductivities of the layer. The approach to the solution for the above equation in the frequency domain is described by Carslaw and Jaeger [43]. Taking the Henkel transform, and Fourier transform of Eq. 2.6 gives us

$$\Lambda_z\frac{\partial^2\theta(\omega,k,z)}{\partial z^2}=(\Lambda_r k^2+C_p i\omega)\theta(\omega,k,z) \tag{2.7}$$

and let us assume that

$$q^2=\frac{\Lambda_r k^2+C_p i\omega}{\Lambda_z} \tag{2.8}$$

for a layer of material n, the temperature, θ_n, and heat flux $f_{n,}$ on the top surface are related to the temperature and the heat flux of the bottom surface by

$$\begin{pmatrix} \theta_{n,b} \\ f_{n,b} \end{pmatrix} = \begin{pmatrix} \cosh(qd) & \frac{-\sinh(qd)}{\Lambda_z q} \\ -\Lambda_z q sinh(qd) & cosh(qd) \end{pmatrix} \begin{pmatrix} \theta_{n,t} \\ f_{n,t} \end{pmatrix} \tag{2.9}$$

where d is the thickness of the layer. Now there is a thermal boundary conductance *G* between the bottom surface of the layer n and the top surface of the layer n+1. This can also be written in a matrix form as

$$\begin{pmatrix} \theta_{n+1,t} \\ f_{n+1,t} \end{pmatrix} = \begin{pmatrix} 1 & -G^{-1} \\ 0 & 1 \end{pmatrix} \begin{pmatrix} \theta_{n,b} \\ f_{n,b} \end{pmatrix} \tag{2.10}$$

Combining Eqs. 2.9 and 2.10, we get a solution for a multilayer sample by the matrix multiplication of the above 2 equations

$$\begin{pmatrix} \theta_b \\ f_b \end{pmatrix} = M_N M_{N-1} \cdots M_2 M_1 \begin{pmatrix} \theta_t \\ f_t \end{pmatrix} \tag{2.11}$$

And from above equation, let us assume

$$M_N M_{N-1} \cdots M_2 M_1 = \begin{pmatrix} A & B \\ C & D \end{pmatrix} \tag{2.12}$$

If we consider an adiabatic and semi-infinite boundary condition to the bottom surface of the Nth layer, the surface temperature is given by

$$\theta_t = \frac{-D}{C} f_t \tag{2.13}$$

The radial heat flux distribution of the pump beam's top surface heat flux boundary condition is given by

$$I(r,t) = \frac{2P(t)}{\pi w_0^2} \exp\left(\frac{-2r^2}{w_0^2}\right) \tag{2.14}$$

where $P(t)$ is the total absorbed pump power in the time domain and w_0^2 is the $1/e^2$ radius of the pump beam on the top surface. Taking the Fourier transform, and Hankel transform of Eq. 2.14 and substituting it into Eq. 2.13, we get

$$\theta_t(\omega, k) = \left(\frac{-D}{C}\right) \frac{P(\omega)}{2\pi} exp(\frac{-k^2 w_0^2}{8}) \tag{2.15}$$

The temperature distribution in the real space is computed by taking the Hankel transform of Eq. 2.15,

$$\theta_t(\omega, r) = \int_0^\infty k J_0(kr) \left(\frac{-D}{C}\right) \frac{P(\omega)}{2\pi} exp(\frac{-k^2 w_0^2}{8}) dk \tag{2.16}$$

The reflected probe signal is proportional to the average surface temperature weighted by the Gaussian distribution of the probe intensity on the surface

$$\overline{\theta_t(\omega)} = \frac{P(\omega)}{2\pi} \int_0^\infty k \left(\frac{-D}{C}\right) \exp\left[\frac{-k^2(w_0^2 + w_1^2)}{8}\right] dk \tag{2.17}$$

where w_1 is the $1/e^2$ radius of the probe beam on the surface. Frequency response of the sample is inserted into Eq. 2.5 by dividing $\overline{\theta_t(\omega)}$by $P(\omega)$:

$$H(\omega) = \frac{1}{2\pi} \int_0^\infty k \left(\frac{-D}{C}\right) \exp\left[\frac{-k^2(w_0^2 + w_1^2)}{8}\right] dk \tag{2.18}$$

And then, phase is measured by the lock-in amplifier, given by

$$\phi_{LI} = \tan^{-1} \frac{\Im(H(\omega))}{\Re(H(\omega))} + \phi_{ext} \tag{2.19}$$

where ϕ_{ext} is introduced in the beam because of it moving through the optical and electronic components in the set-up. $\phi_{ext}$is measured at each frequency of modulation before fitting the lock-in data with the $H(\omega)$ derived from the thermal model. In Eq. 2.19, $\Im(H(\omega))$ is the imaginary part of $H(\omega)$ and $\Re(H(\omega))$ is the real part of $H(\omega)$.

2.4 Sensitivity Analysis

To determine how sensitive the phase signal is to multiple properties in the thermal model, we use phase sensitivity $S(\omega)$, which is calculated by

$$S\left(\omega\right) = \frac{\partial \phi(\omega)}{\partial ln x} \tag{2.20}$$

where x is the parameter as a function of frequency. In Figure 2.4, we plot the sensitivity to various parameters such as cross-plane thermal conductivity, in-plane thermal conductivity and thermal boundary conductance for Sapphire and Si respectively.

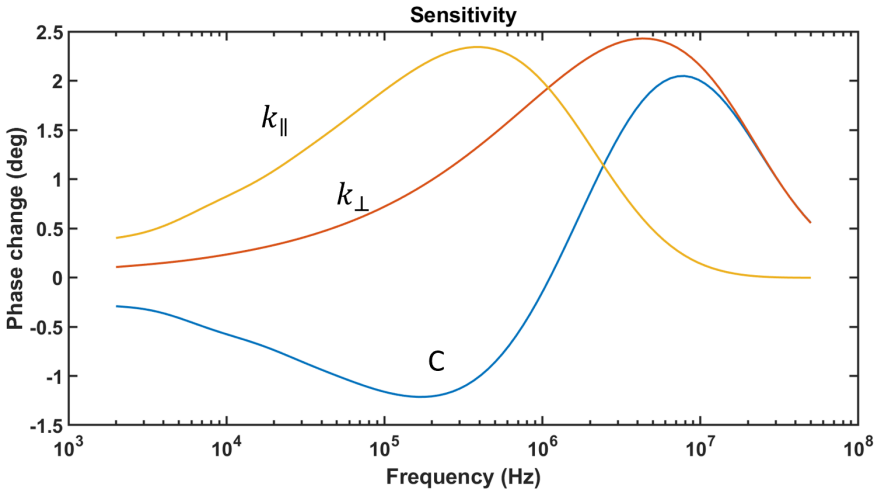

Figure 2.4: Plotting sensitivity for some known reference sample Si

In case of Sapphire, we can observe that the sensitivity to in-plane thermal conductivity is dominant in the low frequency regime, whereas sensitivity to cross-plane conductivity is higher in the high frequency regime, because of the transition in dimension of heat transfer from 2D to 1D occurs when we compare the penetration length with the spot size at various frequencies in the modulation frequency range, as explained in the introduction section. In case of Si, the in-plane conductivity is dominant in the mid-frequency range and cross-plane conductivity exhibits similar behavior like Sapphire. The peaks of sensitivity seem to be narrower for Si in comparison

to Sapphire. Another interesting aspect is that the curves for volumetric heat capacity and cross plane conductivity for both the materials tend to meet in frequency range greater than 10 MHz. The frequency range in which this happens for Si is smaller than for Sapphire. This behavior plays an important role in determining measurement methodology for materials using FDTR, as discussed in the following sections.

2.5 Uncertainty Analysis

This implementation of uncertainty analysis is based on FDTR where the system is equipped to record the phase lag in the probe beam due to the modulation of pump beam at various frequencies in a modulation frequency range. Let us assume that p unknown parameters, x_u, u = 1, 2, ..., *p*, have to be estimated by fitting the phase lag data calculated from a model to the measured phase lag. The model estimates the phase lag of the reflected probe signal, ϕ through a nonlinear function of the unknown parameters and the pump modulation frequency, ω represented as:

$$\phi = f(\omega, X_U) \tag{2.21}$$

where X_U, is a vector of unknown parameters (x_1, x_2, ..., x_p) with dimensions p $\times$ 1. The least squares estimate of the unknown parameter vector X_u minimizes the sum of squared R which is represented as $\widehat{X}_U$.

$$R = \sum_{i=1}^{M} [\phi_i - f(\omega_i, X_U)]^2 \tag{2.22}$$

where $\phi_i, i = 1, 2, \ldots, M$ are the M measured phase data points at frequencies ω_i. R is minimized by equating the first derivative or R with respect to each X_u to zero, as indicated below

$$\frac{\partial R(X_U)}{\partial x_u} | \widehat{X}_U = 0, u = 1, 2, \ldots, p \tag{2.23}$$

Taking the first order Taylor series expansion of $f(\omega_{i,}X_U)$ near the mean of $\widehat{X}_U$, denoted as $X_U^\star$, leads to [44]:

$$\widehat{X}_U = \left(J_U^{\star\prime} J_U^\star\right)^{-1} J_U^{\star\prime}(\Phi - F(X_U^\star)) + X_U^\star \tag{2.24}$$

where Φ is vector with dimensions M $\times$ 1, with measured phase data ϕ_i, The vector $F\left(X_U^\star\right)$ has dimensions M $\times$ 1 with calculated phases $f(\omega_i, X_U^\star)$, and $J_U^\star$ is the Jacobian Matrix:

$$J_U^\star = \begin{pmatrix} \frac{\partial f(\omega_1, X_U)}{\partial x_1}|X_U^\star & \cdots & \frac{\partial f(\omega_1, X_U)}{\partial x_p}|X_U^\star \\ \vdots & \ddots & \vdots \\ \frac{\partial f(\omega_M, X_U)}{\partial x_1}|X_U^\star & \cdots & \frac{\partial f(\omega_M, X_U)}{\partial x_p}|X_U^\star \end{pmatrix} \tag{2.25}$$

The unknown model parameters in $\widehat{X}_U$ variances are determined through the diagonal elements of the variance-covariance matrix in Eq. 2.25

The aforementioned procedure supports the uncertainty of multiple unknown parameters, $\widehat{X}_U$ for least squares estimate, to the uncertainty of the measured data, Φ. The same method is applied to consider the uncertainty in model parameters that are controlled. We start by establishing that the number of unknown parameters in this FDTR model are N. The N parameters are then divided two groups. The first group is the p unknown parameters x_u, where u = 1,2, . . .*p*, while the second group is the N-*p* controlled parameters x_c where c = p+1, p+2, . . ., N. Column vectors X_U with the elements x_1, x_2, x_3. . .x_N are used to indicate the unknown and controlled parameters respectively. The phase lag ϕ is then represented as:

$$\phi = f(\omega, X_U, X_C) \tag{2.26}$$

where the sum of square of errors is modeled as:

$$R = \sum_{i=1}^{M} [\phi_i - f(\omega_i, X_U, X_C)]^2 \tag{2.27}$$

where ϕ_i, i=1, 2, . . .M are still the M measured phase data points at frequencies ω_i. The least

squares estimate of X_U, which is still denoted as $\widehat{X}_U$, now satisfies

$$\frac{\partial R(X_U, X_C)}{\partial x_u} | \widehat{X}_U = 0, u = 1, 2, \ldots, p \tag{2.28}$$

From Eq. 2.27 and 2.28 we have,

$$\sum_{i=1}^{M} \left([\phi_i - f(\omega_i, X_U, X_C)] \frac{\partial f(\omega_i, X_U, X_C)}{\partial x_u} \right) | \widehat{X}_U = 0, u = 1, 2, ..p \tag{2.29}$$

where we denote the average values of $\widehat{X}_U$ and X_C as $X_U^\star$ and $X_C^\star$ respectively. The corresponding elements are denoted as $x_u^\star$, u=1,2, ... *p*, and $x_c^\star$, c = *p*+1, *p*+2, ...*N*, respectively. When X_U and X_c are in small neighbourhood $X_U^\star$ and $X_C^\star$, $f\left(\omega_i, X_U, X_C\right)$ could be approximated by a first order Taylor expansion around both $X_U^\star$ and $X_C^\star$:

$$\begin{aligned} f\left(\omega_i, X_U, X_C\right) \approx f\left(\omega_i, X_U^\star, X_C^\star\right) + \frac{\partial f(\omega_i, X_U, X_C)}{\partial x_u} | X_U^\star, X_C^\star (x_u - x_u^\star)) \\ + (\sum_{c=p+1}^{N} \frac{\partial f(\omega_i, X_U, X_C)}{\partial x_c} | X_U^\star, X_C^\star \left(x_c - x_c^\star\right), i = 1, 2 \ldots M \end{aligned} \tag{2.30}$$

Substituting $f\left(\omega_i, X_U, X_C\right)$from Eq. 2.29 into Eq. 2.30, we have

$$\begin{aligned} \sum_{i=1}^{M} ([\phi_i - f(\omega_i, X_U^\star, X_C^\star) - \sum_{u=1}^{p} \frac{\partial f(\omega_i, X_U, X_C)}{\partial x_u} | X_U^\star, X_C^\star (\widehat{x}_u - x_u^\star) \\ - \sum_{c=p+1}^{N} \frac{\partial f(\omega_i, X_U, X_C)}{\partial x_c} | X_U^\star, X_C^\star \left(x_c - x_{c^\star}\right)] \frac{\partial f(\omega_i, X_U, X_C)}{\partial x_u} | X_U^\star, X_C^\star) = 0 \end{aligned} \tag{2.31}$$

For u = 1,2, ... p, where $\widehat{x}_c$ are the elements of the least squares estimate vector $\widehat{x}_U$. We utilize matrix operations to simplify Eq 2.31. For i= 1, 2, ...M, we denote Φ as vector consisting of elements ϕ_i and $F(X_U^\star, X_C^\star)$ as a vector with elements $f\left(\omega_i, X_U^\star, X_C^\star\right)$. Jacobian matrices are used

to represent the first order derivatives of $f\left(\omega_i, X_U, X_C\right)$ in Eq. 2.31 so that

$$J_U^\star = \begin{pmatrix} \frac{\partial f(\omega_1, X_U, X_C)}{\partial x_1} | X_U^\star, X_C^\star & \dots & \frac{\partial f(\omega_1, X_U, X_C)}{\partial x_p} | X_U^\star, X_C^\star \\ \vdots & \ddots & \vdots \\ \frac{\partial f(\omega_M, X_U, X_C)}{\partial x_1} | X_U^\star, X_C^\star & \dots & \frac{\partial f(\omega_M, X_U, X_C)}{\partial x_p} | X_U^\star, X_C^\star \end{pmatrix} \tag{2.32}$$

$$\text{and } J_C^\star = \begin{pmatrix} \frac{\partial f(\omega_1, X_U, X_C)}{\partial x_{p+1}} | X_U^\star, X_C^\star & \dots & \frac{\partial f(\omega_1, X_U, X_C)}{\partial x_N} | X_U^\star, X_C^\star \\ \vdots & \ddots & \vdots \\ \frac{\partial f(\omega_M, X_U, X_C)}{\partial x_{p+1}} | X_U^\star, X_C^\star & \dots & \frac{\partial f(\omega_M, X_U, X_C)}{\partial x_N} | X_U^\star, X_C^\star \end{pmatrix}$$

Rewriting Eq. 2.31 in terms of Φ, $F\left(X_U^\star, X_C^\star\right)$ and Eq. 2.7, we get,

$$J_u^{\star'}\left(\Phi - F\left(X_U^\star, X_C^\star\right) - J_U^\star\left(\widehat{X}_U - X_U^\star\right) - J_C^\star\left(X_C - X_C^\star\right)\right) = 0 \tag{2.33}$$

With $J_U^{\star'} J_U^\star$ being nonsingular, Eq. 2.33 can be rearranged to express the least squares estimate $\widehat{X}_U$ in terms of the measured phase data Φ, the controlled parameters vector X_C, and the Jacobian matrices:

$$\widehat{X}_U = \left(J_U^{\star'} J_U^\star\right)^{-1} J_U^{\star'}\left(\Phi - F\left(X_U^\star, X_C^\star\right) - J_C^\star\left(X_C - X_C^\star\right)\right) + X_U^\star \tag{2.34}$$

Eq. 2.34, explains us about the uncertainty in the parameters of the model that are controlled as well, as compared to Eq. 2.24. Assuming that the experimental noise for each data point in Φ is normally distributed with zero mean, and that the elements of X_C are normally distributed around their mean values, the elements of $\widehat{X}_U$ will be asymptotically normally distributed around their mean values [45] We calculate the variance-covariance matrix of $\widehat{X}_U$ from Eq. 2.34 to obtain the variances of the individual elements of $\widehat{X}_U$, which we then use to determine the standard deviations for each of the unknown parameters. Given that Φ and X_C are independent vectors, the variance-covariance matrix of $\widehat{X}_U$ is given by,

$$Var[\widehat{X}_U] = (J_U^{\star'} J_U^{\star})^{-1} J_U^{\star'} (Var\left[\Phi\right] + J_C^{\star'} Var\left[X_C\right] J_C^{\star}) J_U^{\star} (J_U^{\star'} J_U^{\star})^{-1} \tag{2.35}$$

If we assume that the elements of Φ and X_C are all independent variables, we can write $Var\left[\Phi\right]$ and $Var\left[X_C\right]$ as

$$Var\left[\Phi\right] = \begin{pmatrix} \sigma_{\phi 1}^2 & 0 & 0 & \cdots \\ 0 & \sigma_{\phi 2}^2 & 0 & \cdots \\ 0 & 0 & \sigma_{\phi 3}^2 & \cdots \\ \vdots & \vdots & \vdots & \ddots \end{pmatrix} \tag{2.36}$$

$$Var\left[X_C\right] = \begin{pmatrix} \sigma_{c1}^2 & 0 & 0 & \cdots \\ 0 & \sigma_{c2}^2 & 0 & \cdots \\ 0 & 0 & \sigma_{c3}^2 & \cdots \\ \vdots & \vdots & \vdots & \ddots \end{pmatrix} \tag{2.37}$$

where $\sigma_{\phi k}^2$, k = 1,2,3. . ., are the variances of the measured phase data points ϕ_{k} at modulation frequencies ω_k and σ_{cl}^2, l = 1,2,3, . . . are the controlled parameters. Thus, using the experimentally determined variances in the phase data and the variances for the controlled parameters, we can determine the variances of the unknown parameters from the diagonal elements of Eq. 2.35

$$Var[\widehat{X}_U] = \begin{pmatrix} \sigma_{xu_1}^2 & cov[x_{u1}, x_{u2}] & cov[x_{u1}, x_{u3}] & \cdots \\ cov[x_{u2}, x_{u1}] & \sigma_{xu_2}^2 & cov[x_{u2}, x_{u3}] & \cdots \\ cov[x_{u3}, x_{u1}] & cov[x_{u3}, x_{u2}] & \sigma_{xu_3}^2 & \cdots \\ \vdots & \vdots & \vdots & \ddots \end{pmatrix} \tag{2.38}$$

where $cov[x_{u2}, x_{u1}]$ is the covariance of x_{ui} and x_{uj}. If we let P_{ij} be element (i, j) of $Var[\widehat{X}_U]$, the standard deviation of the i$^{\text{th}}$ element of $\widehat{X}_U$ will be $\sqrt{P_{ij}}$, which we take to be the uncertainty of that parameter. For the case of a single unknown fitting parameter and no experimental noise, Eq. 2.35 is equivalent to the uncertainty estimate for TDTR given in [6].

2.6 Sample Preparation and Transducer Characterization

To start the process of measuring thermal properties of a material using FDTR, key initial steps are required to be ready for the process. As discussed in the previous sections, it is imperative for us to know the values of as many variables as we can, so as to reduce the number of free parameters that need to be adjusted, leading to high confidence and low uncertainty results. Samples under study need to have an 80-100 nm thick transducer layer deposited on its surface. For our experimental setup, we use gold as our transducer layer. This is because at 473 nm wavelength, gold has high absorptivity, which is responsible for maximizing the heating of the sample surface by the pump laser beam. Gold also has high thermoreflectivity or coefficient of thermo reflectance at the probe laser beam at 532 nm wavelength. This is important to improve the quality of the signal and reduce the noise, in effect increasing the signal to noise ratio for the probe beam reflecting of the heated sample surface. The gold thin film is deposited using [36, 46, 47] Lesker Nano36 Evaporator thermal evaporator, (part of Microfabrication Research $\&$ Education Center at University of Oklahoma). The target gold pellet was purchased from Kurt. J Lesker Company (99$\%$ purity).

The gold is deposited at a very low deposition rate of 1 Å/s and at a target thickness of 100 nm. This process may require a proper characterization of thickness achieved during deposition as compared to the target thickness. This is because the gold thin film thickness values depend on the deposition rate as well as where the sample is placed on the sample holder in the thermal evaporator. Another important factor is the tooling percentage (the ratio between the film thickness, measured by the profilometer on the substrate to the thickness measured by the crystal monitor), which can also change the thickness acquired as compared to the target thickness. The reason for using very low deposition rate is because, it has been observed that the volumetric heat capacity of gold thin film, deposited on a substrate with known properties (like Fused Silica) computed using FDTR, varied from $\sim$80$\%$ of the bulk value for a deposition rate of 4 Å/s to a considerable $\sim$97$\%$ of its bulk value for a deposition rate of 0.5 Å/s as seen in Fig. 2.5. This is because of its

dependence on the grain size, deposition method and deposition rate. [41]

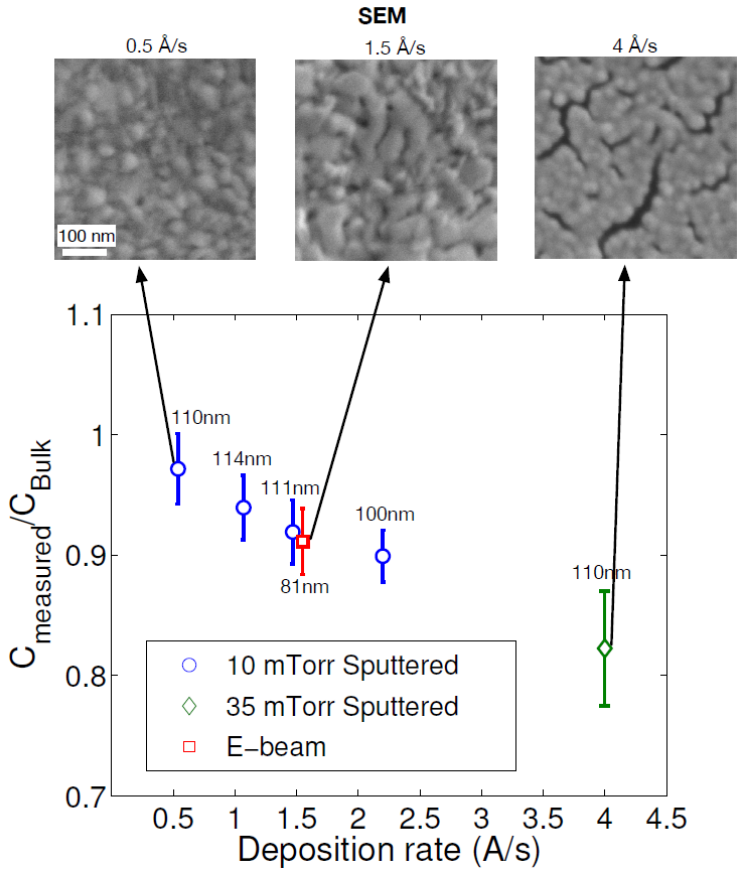

Figure 2.5: Measured over bulk C gold deposited at different deposition rates

To characterize the properties of gold thin film transducer, we place a reference sample like fused silica or silicon (because of their contrasting values of thermal conductivity) or both, very close to the sample under study in the evaporator. After deposition, the thermal conductivity of gold k_{Au} and thickness of the gold thin film are considered to be free parameters and are determined by FDTR measurements using the known properties of the reference sample. Another way to determine k_{Au} and t_{Au} is by measuring electrical resistivity of gold and converting it into thermal conductivity using Wiedemann-Franz Law and profilometer respectively [21]. demonstrated that the values obtained for k_{Au} and t_{Au} using both methods yielded similar results. Hence fitting of gold parameters with respect to known substrate parameters is an effective way of characterizing

transducer properties. Once gold properties are known, we can commence measurement using FDTR.

For the analysis of the materials in this report, we worked with 2 different codes, where the upgraded code includes transducer layer properties such as co-efficient of thermoreflectance (CTR), transducer absorptivity, along with calibrated pump laser power. The laser power is calibrated using a laser power meter. This is to ensure highest accuracy and account for the power loss in the pump beam in the time it travels from the laser and the reaches the sample surface. Another improvement in the code is the real time plotting of the uncertainty as well as the sensitivity plots. These improvements help in understanding whether a set of parameters chosen to be free/adjusted can give us reliable and certain data or not. This also tells us whether the parameters chosen for fitting are coupled in a way, which can lead to difficulty in distinguishing/isolating the properties for measurement.

Sensitivity plots also give us an idea whether the parameters are sensitive to the measurement in the modulation frequency range or not. Insensitive parameters do not affect the curve fitting or the

values of the fitted parameters, and hence can be assigned the highest value of the specific insensitive parameter and can be used as a fixed know input parameter. This helps in minimizing the number of parameters to be fitted as the curve fitting in FDTR yields desirable results for a set of 4 or less unknown/adjusted/free parameters. CTR value is fitted for the reference sample. This fitted value is assumed to be the CTR value of the transducer layer for the sample under study. Transducer absorptivity is a value that is used as a fixed input parameter from literature for a gold thin film layer. We can estimate this value by varying the value of absorptivity and by observing its effect on the curve fitting.

Once the best possible curve fitting is achieved, value of absorptivity can be considered fixed for the measurement. This specific example is of the Sapphire reference sample under analysis, to characterize the properties of the transducer layer for GaP measurement. During this step, we first consider that the gold transducer properties as mentioned above to be unknown. These values

are then measured by fitting this set of unknown parameters to the measured phase lag for the reference Sapphire sample, whose properties are known to us, yielding the best curve fit for the reference sample. By executing the aforementioned steps, the values for CTR are measured to be 3.202 X 10^{-4} K^{-1}, k_{Au} is 164 $Wm^{-1}K^{-1}$, t_{Au} is 164 nm and a thermal boundary conductance value of $\sim$77 $MWm^{-2}K^{-1}$ between the transducer layer and reference sample (Sapphire).

Chapter 3

Background on Quantum ESPRESSO and ShengBTE

3.1 Theory of Thermal Conductivity

Here, we build upon the theory of thermal conductivity using the foundation laid out in the ref. [48]. A crystal's unit cell defined by the vector ***l*** while the vector ***b*** describes the atomic positions in each unit cell, has a potential energy V. This potential energy can be defined as a Taylor series expansion in the powers of the atomic displacements ***u(lb)***. Writing the expansion up to the third order, it is represented as:

$$\begin{aligned} V = V_0 + \sum_{\boldsymbol{lb}\alpha} \left.\frac{\partial V}{\partial u_\alpha(\boldsymbol{lb})}\right|_0 u_\alpha(\boldsymbol{lb}) + \\ \frac{1}{2}\sum_{\boldsymbol{lb},\boldsymbol{l'b'}}\sum_{\alpha\beta} \left.\frac{\partial^2 V}{\partial u_\alpha(\boldsymbol{lb}) u_\beta(\boldsymbol{l'b'})}\right|_0 u_\alpha(\boldsymbol{lb}) u_\beta(\boldsymbol{l'b'}) + \\ \frac{1}{3!}\sum_{\boldsymbol{lb},\boldsymbol{l'b'},\boldsymbol{l''b''}}\sum_{\alpha\beta\gamma} \left.\frac{\partial^3 V}{\partial u_\alpha(\boldsymbol{lb}) u_\beta(\boldsymbol{l'b'}) u_\gamma(\boldsymbol{l''b''})}\right|_0 u_\alpha(\boldsymbol{lb}) u_\beta(\boldsymbol{l'b'}) u_\gamma(\boldsymbol{l''b''}). \end{aligned} \tag{3.1}$$

With the potential energy's first derivative with respect to atomic displacements being zero at equilibrium, it is defined as:

$$\left.\frac{\partial V}{\partial u_\alpha(\boldsymbol{lb})}\right|_0 = 0 \tag{3.2}$$

This is because of the energy being minimum in this specific configuration. To determine the second order force constants, we take the second order derivative of the crystal's potential energy with respect to the atomic displacements, defined as:

$$\Phi_{\alpha\beta}(\boldsymbol{lb}, \boldsymbol{l'b'}) = \left.\frac{\partial^2 V}{\partial u_\alpha(\boldsymbol{lb}) u_\beta(\boldsymbol{l'b'})}\right|_0 \tag{3.3}$$

and the third-order force constants are derived by taking the third order derivative of the crystal's potential energy with respect to the atomic displacements.

$$\Phi_{\alpha\beta\gamma}(\boldsymbol{lb}, \boldsymbol{l'b'}, \boldsymbol{l''b''}) = \frac{\partial^3 V}{\partial u_\alpha(\boldsymbol{lb}) u_\beta(\boldsymbol{l'b'}) u_\gamma(\boldsymbol{l''b''})}\bigg|_0 \tag{3.4}$$

Re-writing the potential energy in terms of the force constants, we get,

$$\begin{aligned} V = V_0 + \frac{1}{2} \sum_{\boldsymbol{lb}, \boldsymbol{l'b'}} \sum_{\alpha\beta} \Phi_{\alpha\beta}(\boldsymbol{lb}, \boldsymbol{l'b'}) u_\alpha(\boldsymbol{lb}) u_\beta(\boldsymbol{l'b'}) + \\ \frac{1}{3!} \sum_{\boldsymbol{lb}, \boldsymbol{l'b'}, \boldsymbol{l''b''}} \sum_{\alpha\beta\gamma} \Phi_{\alpha\beta\gamma}(\boldsymbol{lbl'b'l''b''}) u_\alpha(\boldsymbol{lb}) u_\beta(\boldsymbol{l'b'}) u_\gamma(\boldsymbol{l''b''}). \end{aligned} \tag{3.5}$$

3.1.1 Dynamical Matrix and Phonon Frequencies

It can be demonstrated that the displacements can be expressed in terms of fully decoupled vibration modes if the crystal potential expression is written up to the second-order with regard to atomic displacements. Since it produces no forces on atoms, the initial term in the potential energy V_0 is disregarded in order to get the equation of motion. The equation of motion can be expressed as:

$$m_b \ddot{u}_{\alpha\beta}(\boldsymbol{lb}) = -\sum_{\boldsymbol{l'b'}\beta} \Phi_{\alpha\beta}(\boldsymbol{lb}, \boldsymbol{l'b'}) u_\beta(\boldsymbol{l'b'}) \tag{3.6}$$

Re-writing the second-order force constants in terms of the relative positions between the unit cells $\boldsymbol{h} = \boldsymbol{l'} - \boldsymbol{l}$, due to translation symmetry, we get:

$$\Phi_{\alpha\beta}(\boldsymbol{lb}, \boldsymbol{l'b'}) = \Phi_{\alpha\beta}(\boldsymbol{0b}, (\boldsymbol{l'} - \boldsymbol{l})\boldsymbol{b'}) \tag{3.7}$$

Therefore, the equation of the motion becomes:

$$m_b \ddot{u}_\alpha(\boldsymbol{lb}) = -\sum_{\boldsymbol{l'b'}\beta} \Phi_{\alpha\beta}(\boldsymbol{0b}, \boldsymbol{l'b'}) u_\beta(\boldsymbol{l'b'}) \tag{3.8}$$

The above equation can be solved by writing the atomic displacements as:

$$u_\alpha(\boldsymbol{lb}) = \frac{1}{\sqrt{m_b}} \sum_q U_\alpha(\boldsymbol{q,b}) exp[i(\boldsymbol{q.l} - \omega t)], \tag{3.9}$$

where $\boldsymbol{q}$ is the vibrational mode's wave-vector in the first Brillouin zone, and ω being the vibrational mode's frequency. The result of substituting Eq. 3.9 into Eq. 3.8, we get:

$$\omega^2 U_\alpha(\boldsymbol{q,b}) = \sum_{\boldsymbol{b'}\beta} D_{\alpha\beta}(\boldsymbol{bb'})|\boldsymbol{q}) U_\beta(\boldsymbol{q}, \boldsymbol{b'}) \tag{3.10}$$

Where the above equation's determinant equation is determined as:

$$|D_{\alpha\beta}(\boldsymbol{bb'}|\boldsymbol{q}) - \omega^2 \delta_{\alpha\beta} \delta_{\boldsymbol{bb'}}| = 0 \tag{3.11}$$

where $D_{\alpha\beta}(\boldsymbol{bb'}|q)$ is the dynamical matrix and is given by the following expression:

$$D_{\alpha\beta}(\boldsymbol{bb'}|\boldsymbol{q}) = \frac{1}{\sqrt{m_b m_{b'}}} \sum_{\boldsymbol{l'}} \Phi_{\alpha\beta}(\boldsymbol{0b}, \boldsymbol{l'b'}) exp(i\boldsymbol{q}.\boldsymbol{l'}) \tag{3.12}$$

Phonon frequencies are obtained by diagonalizing the dynamical matrix. Therefore, the presence of completely de-coupled vibrational modes that do not interact with each other are a result of expanding the potential energy expression only up to the second-order. To show this more clearly, we observe that the crystal's Hamiltonian can be expressed as follows in the harmonic approximation,

which ignores the third-order term in the expansion of potential energy:

$$H = \sum_{\boldsymbol{lb}} \frac{\boldsymbol{p(lb).p(lb)}}{2m} + \frac{1}{2} \sum_{\boldsymbol{lb},\boldsymbol{l'b'}} \sum_{\alpha\beta} \Phi_{\alpha\beta}(\boldsymbol{lb},\boldsymbol{l'b'}) u_\alpha(\boldsymbol{lb}) u_\beta(\boldsymbol{l'b'}) \tag{3.13}$$

where the momentum operator of an atom located at ***l + b*** is denoted by ***p(lb)***. We then replace the Fourier representations ***X*** and ***P*** of displacement and momentum operators respectively, through series of transformations. This then allows the above equation to be re-written in terms of vibration wave-vectors ***q*** as:

$$\boldsymbol{u(lb)} = \frac{1}{\sqrt{N_0}} \sum_{q} \boldsymbol{X(q,b)} e^{\boldsymbol{iq.l}} \tag{3.14}$$

$$\boldsymbol{p(lb)} = \frac{1}{\sqrt{N_0}} \sum_{q} \boldsymbol{P(q,b)} e^{-\boldsymbol{iq.l}} \tag{3.15}$$

Here$N_o = N_1 N_2 N_3$ is the crystal size, N_1, N_2 and N_3 being the number of unit cells along the three lattice directions. Using the above transformations the Hamiltonian can be rewritten as,

$$H = \frac{1}{N_0} \sum_{\boldsymbol{qq'lb}} \frac{\boldsymbol{P(q,b).P(q',b)}}{2m_b} exp[-i(\boldsymbol{q}+\boldsymbol{q'}).\boldsymbol{l}] + \frac{1}{2}\frac{1}{N_0} \sum_{\boldsymbol{q},\boldsymbol{q'}} \sum_{\boldsymbol{lb},\boldsymbol{l'b'}} \sum_{\alpha\beta} \Phi_{\alpha\beta}(\boldsymbol{lb},\boldsymbol{l'b'}) X_\alpha(\boldsymbol{q,b}) X_\beta(\boldsymbol{q'},\boldsymbol{b'}) exp[i(\boldsymbol{q.l}+\boldsymbol{q'.l'})] \tag{3.16}$$

Simplifying the first term by summing over ***l,***

$$\begin{aligned} \text{First term} &= \sum_{\boldsymbol{q},\boldsymbol{q'b}} \frac{\boldsymbol{P(qb).P(q'b)}}{2m_b} \frac{1}{N_0} \sum_{\boldsymbol{l}} exp[-i(\boldsymbol{q}+\boldsymbol{q'}).\boldsymbol{l}] \\ &= \sum_{\boldsymbol{qq'b}} \frac{\boldsymbol{P(qb).P(q'b)}}{2m_b} \delta_{\boldsymbol{q}+\boldsymbol{q'},0} \\ &= \sum_{\boldsymbol{qb}} \frac{\boldsymbol{P(qb).P^\dagger(q'b)}}{2m_b} \end{aligned} \tag{3.17}$$

As indicated earlier, because of the translational symmetry, the second-order force constants

can be rewritten in terms of only the relative position between the unit cells $\boldsymbol{h} = \boldsymbol{l}' - \boldsymbol{l}$ as shown by Eq. 3.7. Using this the second term can be rewritten as:

$$\begin{aligned}
&= \frac{1}{2}\frac{1}{N_0}\sum_{\boldsymbol{q},\boldsymbol{q}'}\sum_{\boldsymbol{lb},\boldsymbol{l}'\boldsymbol{b}'}\sum_{\alpha\beta}\Phi_{\alpha\beta}(\boldsymbol{lb},\boldsymbol{l}'\boldsymbol{b}')X_\alpha(\boldsymbol{q},\boldsymbol{b})X_\beta(\boldsymbol{q}',\boldsymbol{b}')exp[i(\boldsymbol{q}.\boldsymbol{l}+\boldsymbol{q}'.\boldsymbol{l}')] \\
&= \frac{1}{2}\frac{1}{N_0}\sum_{\boldsymbol{q},\boldsymbol{q}'}\sum_{\boldsymbol{b},\boldsymbol{hb}'}\sum_{\alpha\beta}\Phi_{\alpha\beta}(\boldsymbol{0b},\boldsymbol{hb}')X_\alpha(\boldsymbol{q},\boldsymbol{b})X_\beta(\boldsymbol{q}',\boldsymbol{b}')exp[i\boldsymbol{q}'.\boldsymbol{h}]\sum_{\boldsymbol{l}}exp[i(\boldsymbol{q}+\boldsymbol{q}').\boldsymbol{l}'] \\
\text{Second Term} \quad &= \frac{1}{2}\sum_{\boldsymbol{q},\boldsymbol{q}'}\sum_{\boldsymbol{b},\boldsymbol{hb}'}\sum_{\alpha\beta}\Phi_{\alpha\beta}(\boldsymbol{0b},\boldsymbol{hb}')X_\alpha(\boldsymbol{q},\boldsymbol{b})X_\beta(\boldsymbol{q}',\boldsymbol{b}')exp[i\boldsymbol{q}'.\boldsymbol{h}]\delta_{\boldsymbol{q}+\boldsymbol{q}',\boldsymbol{0}} \\
&= \frac{1}{2}\sum_{\boldsymbol{q}}\sum_{\boldsymbol{b},\boldsymbol{hb}'}\sum_{\alpha\beta}\Phi_{\alpha\beta}(\boldsymbol{0b},\boldsymbol{hb}')X_\alpha(\boldsymbol{q},\boldsymbol{b})X_\beta(\boldsymbol{-q},\boldsymbol{b}')exp[-i\boldsymbol{q}.\boldsymbol{h}]
\end{aligned} \tag{3.18}$$

In the above use is made of $\sum_{\boldsymbol{l}} exp[i(\boldsymbol{q}+\boldsymbol{q}').\boldsymbol{l}] = N_0\delta_{\boldsymbol{q}+\boldsymbol{q}'.\boldsymbol{o}}$. Using

$$\Phi_{\alpha\beta}(\boldsymbol{bb}'|\boldsymbol{q}) = \sum_{\boldsymbol{h}}\Phi_{\alpha\beta}(\boldsymbol{0b},\boldsymbol{h}b')exp(-i\boldsymbol{q}.\boldsymbol{h}) = \sqrt{m_b m_{b'}}D_{\alpha\beta}(\boldsymbol{b}b'|\boldsymbol{-q}) \tag{3.19}$$

where D is a synamical matrix, the second term can now be written as

$$\text{Second Term} = \frac{1}{2}\sum_{\boldsymbol{q},\boldsymbol{b},\boldsymbol{b}'}\sum_{\alpha\beta}\Phi_{\alpha\beta}(\boldsymbol{bb}'|\boldsymbol{q})X_\alpha(\boldsymbol{q},\boldsymbol{b})X^\dagger{}_\beta(\boldsymbol{qb}') \tag{3.20}$$

Using Eqs. 3.17 and 3.20 crystal Hamiltonian in the harmonic approximation can now be written as a sum over the different vibration wave vectors $\boldsymbol{q}$,

$$H = \sum_{\boldsymbol{q}}\Big[\sum_{\boldsymbol{b}}\frac{\boldsymbol{P}(\boldsymbol{qb}).\boldsymbol{P}^\dagger(\boldsymbol{q},\boldsymbol{b})}{2m_b} + \frac{1}{2}\sum_{\boldsymbol{b},\boldsymbol{b}'}\sum_{\alpha\beta}\Phi_{\alpha\beta}(\boldsymbol{bb}'|\boldsymbol{q})X_\alpha(\boldsymbol{q},\boldsymbol{b})X^\dagger{}_\beta(\boldsymbol{qb}')\Big] \tag{3.21}$$

The above Hamiltonian is completely separable and therefore has independent eigen states or vibration modes. However it is shown next that the inclusion of the third-order anharmonic term in the potential energy expansion leads to coupling (scattering) between three vibration modes.

3.1.2 Anharmonic Potential

Including the third-order term in the expansion of the potential energy the crystal Hamiltonian can be written as:

$$\begin{aligned} H = & \sum_{\boldsymbol{lb}} \frac{\boldsymbol{p(lb).p(lb)}}{2m} + \\ & \frac{1}{2} \sum_{\boldsymbol{lb},\boldsymbol{l'b'}} \sum_{\alpha\beta} \Phi_{\alpha\beta}(\boldsymbol{lb},\boldsymbol{l'b'}) u_\alpha(\boldsymbol{lb}) u_\beta(\boldsymbol{l'b'}) + \\ & \frac{1}{3!} \sum_{\boldsymbol{lb},\boldsymbol{l'b'},\boldsymbol{l''b''}} \sum_{\alpha\beta\gamma} \Phi_{\alpha\beta\gamma}(\boldsymbol{lb},\boldsymbol{l'b'},\boldsymbol{l''b''}) u_\alpha(\boldsymbol{lb}) u_\beta(\boldsymbol{l'b'}) u_\gamma(\boldsymbol{l''b''}). \end{aligned} \tag{3.22}$$

We focus the discussion on rewriting of the third term V_3 to show how anharmonicity leads to three-phonon coupling. Using the transformations represented by Eqs. 3.14 and 3.15,V_3 can be rewritten as

$$\begin{aligned} V_3 = & \frac{1}{3!} \frac{1}{(N_0)^{3/2}} \sum_{\boldsymbol{qq'q''}} \sum_{\boldsymbol{lb},\boldsymbol{l'b'},\boldsymbol{l''b''}} \sum_{\alpha\beta\gamma} \Phi_{\alpha\beta\gamma}(\boldsymbol{lb},\boldsymbol{l'b'},\boldsymbol{l''b''}) \boldsymbol{X}_\alpha(\boldsymbol{q,b}) \boldsymbol{X}_\beta(\boldsymbol{q'},\boldsymbol{b'}) \boldsymbol{X}_\gamma(\boldsymbol{q''},\boldsymbol{b''}) \\ & \times exp[i(\boldsymbol{q}.\boldsymbol{l} + \boldsymbol{q'}.\boldsymbol{l'} + \boldsymbol{q''}.\boldsymbol{l''})] \end{aligned} \tag{3.23}$$

Defining $\boldsymbol{h'} = \boldsymbol{l'} - \boldsymbol{l}$ and $\boldsymbol{h''} = \boldsymbol{l''} - \boldsymbol{l}$ the cubic term V_3 can be further rewritten as

$$\begin{aligned} V_3 = & \frac{1}{3!} \frac{1}{(N_0)^{3/2}} \sum_{\boldsymbol{qb},\boldsymbol{q'b'},\boldsymbol{q''b''}} \sum_{\alpha\beta\gamma} \sum_{\boldsymbol{l}} exp[i(\boldsymbol{q} + \boldsymbol{q'} + \boldsymbol{q''}).\boldsymbol{l}] \\ & \times \Phi_{\alpha\beta\gamma}(\boldsymbol{qb},\boldsymbol{q'b'},\boldsymbol{q''b''}) \boldsymbol{X}_\alpha(\boldsymbol{q,b}) \boldsymbol{X}_\beta(\boldsymbol{q'},\boldsymbol{b'}) \boldsymbol{X}_\gamma(\boldsymbol{q''},\boldsymbol{b''}) \end{aligned} \tag{3.24}$$

where

$$\Phi_{\alpha\beta\gamma}(\boldsymbol{lbl'b'l''b''}) = \sum_{\boldsymbol{h'},\boldsymbol{h''}} \Phi_{\alpha\beta\gamma}(\boldsymbol{ob},\boldsymbol{h'b'},\boldsymbol{h''b''}) e^{i\boldsymbol{q'h'}} e^{i\boldsymbol{q''h''}} \tag{3.25}$$

Finally summing over $\boldsymbol{l}$ and realizing that $\sum_{\boldsymbol{l}} exp[i(\boldsymbol{q}+\boldsymbol{q'}+\boldsymbol{q''}).l] = N_0\delta_{\boldsymbol{G},\boldsymbol{q}+\boldsymbol{q'}+\boldsymbol{q''}}$ we obtain

$$\begin{aligned} V_3 = \frac{1}{3!}\frac{1}{\sqrt{N_0}} \sum_{\boldsymbol{qb},\boldsymbol{q'b'},\boldsymbol{q''b''}} \delta_{\boldsymbol{G},\boldsymbol{q}+\boldsymbol{q'}+\boldsymbol{q''}} \\ \times \sum_{\alpha\beta\gamma} \Phi_{\alpha\beta\gamma}(\boldsymbol{qb},\boldsymbol{q'b'},\boldsymbol{q''b''})\boldsymbol{X}_\alpha(\boldsymbol{q,b})\boldsymbol{X}_\beta(\boldsymbol{q'},\boldsymbol{b'})\boldsymbol{X}_\gamma(\boldsymbol{q''},\boldsymbol{b''}) \end{aligned} \tag{3.26}$$

$\boldsymbol{G}$ in the above equation is the reciprocal lattice vector. To explicitly show the three-phonon couplings and to convert the anharmonic term into a form where it can be used to compute the three-phonon scattering rates, two more transformations are performed. The second set of transformations allows the anharmonic term to be expressed in terms of the vibration eigenvectors $\boldsymbol{e}(\boldsymbol{b}|\boldsymbol{q}s)$, where s represents a particular vibration mode of the vibration characterized by wave-vector $\boldsymbol{q}$. The transformations are indicated below:

$$X(\boldsymbol{q}s) = \sum_{\boldsymbol{b}} \sqrt{m_b}\boldsymbol{e}^*(\boldsymbol{b}|\boldsymbol{q}s).\boldsymbol{X}(\boldsymbol{qb}) \tag{3.27}$$

$$P(\boldsymbol{q}s) = \sum_{\boldsymbol{b}} \frac{1}{\sqrt{m_b}}\boldsymbol{e}(\boldsymbol{b}|\boldsymbol{q}s).\boldsymbol{P}(\boldsymbol{qb}) \tag{3.28}$$

The vibration eigenvectors oney the following relationships

$$\sum_{\boldsymbol{b}} \boldsymbol{e}^*(\boldsymbol{b}|\boldsymbol{q}s).\boldsymbol{e}(\boldsymbol{b}|\boldsymbol{q}s') = \delta_{ss'} \tag{3.29}$$

$$\sum_{\boldsymbol{b}} \boldsymbol{e}^*_\alpha(\boldsymbol{b}|\boldsymbol{q}s).\boldsymbol{e}_\beta(\boldsymbol{b'}|\boldsymbol{q}s) = \delta_{\alpha\beta}\delta_{\boldsymbol{bb'}} \tag{3.30}$$

Finally, the last set of transformations involves the use of the creation and annihilation operators $a_{\boldsymbol{q}s}$, and $a^\dagger_{\boldsymbol{q}s}$.

$$a_{\boldsymbol{q}s} = \frac{1}{\sqrt{2\hbar\omega(\boldsymbol{q}s)}}P(\boldsymbol{q}s) - i\sqrt{\frac{\omega(\boldsymbol{q}s)}{2\hbar}}X^\dagger(\boldsymbol{q}s) \tag{3.31}$$

$$a^\dagger_{\boldsymbol{q}s} = \frac{1}{\sqrt{2\hbar\omega(\boldsymbol{q}s)}}P^\dagger(\boldsymbol{q}s) + i\sqrt{\frac{\omega(\boldsymbol{q}s)}{2\hbar}}X(\boldsymbol{q}s) \tag{3.32}$$

We discuss next some of the properties of creation and annihilation operators. Let a state with n phonons of wavevector $\boldsymbol{q}$ and polarisation s be denoted by $|n_{\boldsymbol{q}s}\rangle$; the effect of the creation and annihilation operators on such a state is summarized below:

$$a^{\dagger}_{\boldsymbol{q}s}|n_{\boldsymbol{q}s}\rangle = \sqrt{n_{\boldsymbol{q},s}+1}|n_{\boldsymbol{q}s}+1\rangle \tag{3.33}$$

$$a_{\boldsymbol{q}s}|n_{\boldsymbol{q}s}\rangle = \sqrt{n_{\boldsymbol{q},s}}|n_{\boldsymbol{q}s}-1\rangle \tag{3.34}$$

Inverting Eqs 3.31 and 3.32 allows the operators $X(\boldsymbol{q}s)$ and $P(\boldsymbol{q}s)$ to be written in terms of creation and annihilation operators:

$$X(\boldsymbol{q}s) = -i\sqrt{\frac{\hbar}{2\omega(\boldsymbol{q}s)}}(a^{\dagger}_{\boldsymbol{q}s} - a_{-\boldsymbol{q}s}) \tag{3.35}$$

$$P(\boldsymbol{q}s) = \sqrt{\frac{\hbar\omega(\boldsymbol{q}s)}{2}}(a^{\dagger}_{-\boldsymbol{q}s} + a_{\boldsymbol{q}s}) \tag{3.36}$$

Finally, using Eqs. 3.27 and 3.28, the operators $X(\boldsymbol{q}\boldsymbol{b})$ and $P(\boldsymbol{q}\boldsymbol{b})$ can now be written in terms of the vibration eigenvectors and the creation and annihilation operators:

$$\begin{aligned}\boldsymbol{X}(\boldsymbol{q}\boldsymbol{b}) &= \frac{1}{\sqrt{m_b}}\sum_s \boldsymbol{e}(\boldsymbol{b}|\boldsymbol{q}s)X(\boldsymbol{q}s) \\ &= -i\sum_s \sqrt{\frac{\hbar}{2m_b\omega(\boldsymbol{q}s)}}\boldsymbol{e}(\boldsymbol{b}|\boldsymbol{q}s)(a^{\dagger}_{\boldsymbol{q}s} - a_{-\boldsymbol{q}s})\end{aligned} \tag{3.37}$$

$$\begin{aligned}\boldsymbol{P}(\boldsymbol{q}\boldsymbol{b}) &= \sqrt{m_b}\sum_s \boldsymbol{e}^*(\boldsymbol{b}|\boldsymbol{q}s)P(\boldsymbol{q}s) \\ &= \sum_s \sqrt{\frac{m_b\hbar\omega(\boldsymbol{q}s)}{2}}\boldsymbol{e}^*(\boldsymbol{b}|\boldsymbol{q}s)(a^{\dagger}_{-\boldsymbol{q}s} + a_{\boldsymbol{q}s})\end{aligned} \tag{3.38}$$

Substituting the above in the expression for the cubic term in the crystal Hamiltonian yields

$$\begin{aligned} V_3 &= \frac{1}{3!}\frac{i}{\sqrt{N_0}} \sum_{\boldsymbol{qs},\boldsymbol{q's'},\boldsymbol{q''s''},\boldsymbol{bb'b''}} \sum_{\alpha\beta\gamma} \left(\frac{\hbar^3}{8m_{\boldsymbol{b}}m_{\boldsymbol{b'}}m_{\boldsymbol{b''}}\omega(\boldsymbol{qs})\omega(\boldsymbol{q's'})\omega(\boldsymbol{q''s''})} \right)^{1/2} \\ &\times \delta_{\boldsymbol{G},\boldsymbol{q}+\boldsymbol{q'}+\boldsymbol{q''}} e_\alpha(\boldsymbol{b}|\boldsymbol{qs}) e_\beta(\boldsymbol{b'}|\boldsymbol{q's'}) e_\gamma(\boldsymbol{b''}|\boldsymbol{q''s''}) \Phi_{\alpha\beta\gamma}(\boldsymbol{qb},\boldsymbol{q'b'},\boldsymbol{q''b''}) \\ &\times (a^\dagger_{\boldsymbol{qs}} - a_{-\boldsymbol{qs}})(a^\dagger_{\boldsymbol{q's'}} - a_{-\boldsymbol{q's'}})(a^\dagger_{\boldsymbol{q''s''}} - a_{-\boldsymbol{q''s''}}) \\ &= \frac{i\hbar}{3!} \sum_{\boldsymbol{qs},\boldsymbol{q's'},\boldsymbol{q''},s''} \delta_{\boldsymbol{G},\boldsymbol{q}+\boldsymbol{q'}+\boldsymbol{q''}} \tilde{V}(\boldsymbol{qs},\boldsymbol{q's'},\boldsymbol{q''},s'') \\ &\times (a^\dagger_{\boldsymbol{qs}} - a_{-\boldsymbol{qs}})(a^\dagger_{\boldsymbol{q's'}} - a_{-\boldsymbol{q's'}})(a^\dagger_{\boldsymbol{q''s''}} - a_{-\boldsymbol{q''s''}}) \end{aligned} \tag{3.39}$$

where

$$\begin{aligned} \tilde{V}_3(\boldsymbol{qs},\boldsymbol{q's'},\boldsymbol{q''s''}) = &\left(\frac{\hbar}{8N_0\omega(\boldsymbol{qs})\omega(\boldsymbol{q's'})\omega(\boldsymbol{q''s''})} \right)^{1/2} \\ &\sum_{\boldsymbol{b},\boldsymbol{b'},\boldsymbol{b''}} \sum_{\alpha\beta\gamma} \Phi_{\alpha\beta\gamma}(\boldsymbol{qb},\boldsymbol{q'b'},\boldsymbol{q''b''}) \\ &\times \frac{\boldsymbol{e}_\alpha(\boldsymbol{b}|\boldsymbol{qs})}{\sqrt{m_b}} \frac{\boldsymbol{e}_\beta(\boldsymbol{b'}|\boldsymbol{q's'})}{\sqrt{m_{b'}}} \frac{\boldsymbol{e}_\gamma(\boldsymbol{b''}|\boldsymbol{q''s''})}{\sqrt{m_{b''}}} \end{aligned} \tag{3.40}$$

Eq. 3.39 shows that an anharmonic term in the expansion of potential energy leads to scattering between three phonons such that $\boldsymbol{G} = \boldsymbol{q}+\boldsymbol{q'}+\boldsymbol{q''}$. We next compute the rates of phonon scattering due to anharmonicity and use them along with Boltzmann transport to compute thermal conductivity.

3.1.3 Boltzmann Transport Equation

In the absence of a temperature gradient, the heat flux in a material is zero and the phonon modes are in their equilibrium state with the phonon populations being determined by the Bose-Einstein distribution

$$\bar{n}_{\boldsymbol{qs}} = \frac{1}{e^{\hbar\omega(\boldsymbol{qs})/(k_B T)} - 1} \tag{3.41}$$

where $\bar{n}(\boldsymbol{qs})$ and $\omega(\boldsymbol{qs})$ are the equilibrium population and the frequency, respectively, of the phonon mode $\boldsymbol{qs}$, $\hbar$ is the Planck's constant and k_B is the Boltzmann constant. However, the presence of a temperature gradient in a material causes the phonon population of any mode $\boldsymbol{qs}$

to be perturbed out of equilibrium and establishes a heat flux $\boldsymbol{Q}$ than can be written in terms of phonon energies $\hbar\omega(\boldsymbol{q}s)$, perturbed phonon populations $n_{\boldsymbol{q}s}$, and phonon group velocities $\boldsymbol{c}(\boldsymbol{q}s)$ as

$$Q_\alpha = \frac{1}{N_0\Omega}\sum_{\boldsymbol{q}s}\hbar\omega(\boldsymbol{q}s)c_\alpha(\boldsymbol{q}s)n_{\boldsymbol{q}s} = -k_{\alpha\beta}|\nabla T|_\beta \tag{3.42}$$

where Ω is the volume of the unit-cell. As shown above the heat flux can be further written as the product of the thermal conductivity k and the temperature gradient ∇T. Thermal conductivity is a tensor whose components $k_{\alpha\beta}$ give the direction of heat flux along a direction α for a temperature gradient along direction β. Knowledge of the perturbed phonon populations allows heat flux and in turn thermal conductivity to be determined. As phonon populations are a function of temperature, a temperature gradient creates an imbalance in the flux of a phonon mode $\boldsymbol{q}s$ through an elemental volume in the material. If the phonon mode $\boldsymbol{q}s$ does not interact (scatter) with other phonon modes (i.e. $\partial n_{\boldsymbol{q}s}/\partial t_{scatt} = 0$) as is the case in a perfect harmonic crystal, such an imbalance creates a divergence in the perturbed phonon population leading to a divergence in the thermal conductivity. A perfect harmonic crystal therefore has infinite thermal conductivity. Through, three-phonon scattering processes anharmonicity allows for the perturbation due to the temperature gradient to be balanced by the change in phonon population by scattering, leading to a finite thermal conductivity. The resulting balance equation for the perturbed phonon population is called the phonon Boltzmann equation

$$-\boldsymbol{c}(\boldsymbol{q}s).\nabla T\left(\frac{\partial n_{\boldsymbol{q}s}}{\partial T}\right) + \left.\frac{\partial n_{\boldsymbol{q}s}}{\partial T}\right|_{scatt} = 0 \tag{3.43}$$

where $n_{\boldsymbol{q}s}$ and $\boldsymbol{c}_(\boldsymbol{q}s)$ are the perturbed phonon population and group velocity respectively of mode $\boldsymbol{q}s$. The first term on the left-hand side represents phonon diffusion induced by a temperature gradient and the second term represents the phonon scattering rate due to all scattering processes. Assuming that the perturbation from equilibrium is small, the temperature gradient of the perturbed phonon population can be replaced with the temperature gradient of the equilibrium phonon pop-

ulation, $\partial n_{\boldsymbol{q}s}/\partial T \approx \partial \bar{n}_{\boldsymbol{q}s}/\partial T$, leading to

$$-\boldsymbol{c}(\boldsymbol{q}s).\nabla T\left(\frac{\partial \bar{n}_{\boldsymbol{q}s}}{\partial T}\right) + \left.\frac{\partial n_{\boldsymbol{q}s}}{\partial T}\right|_{scatt} = 0 \tag{3.44}$$

where $\bar{n}_{\boldsymbol{q}s}$ is the equilibrium population of mode $\boldsymbol{q}s$ and is determined by the Bose einstein distribution Eq. 3.41.

As indicated in the previous section, in a pure material a phonon mode $\boldsymbol{q}s$ can scatter through anharmonic three-phonon scattering processes such that $\boldsymbol{G} = \boldsymbol{q} + \boldsymbol{q}' + \boldsymbol{q}''$. The three-phonon scattering can thus be classified into two types: 1. Normal processes: For these type of processes, $\boldsymbol{G} = 0$. For example, when a phonon $\boldsymbol{q}$ scatters by absorbing another phonon $\boldsymbol{q}'$ to yield phonon $\boldsymbol{q}''$ the momentum conservation for this process can be written as $-\boldsymbol{q} - \boldsymbol{q}' + \boldsymbol{q}'' = 0$. As can be seen, these processes preserve the direction of energy flow, since the resulting phonon is in the same direction as the combining phonon modes. Hence these processes do not contribute towards thermal resistance in a material. 2. The second type of processes are characterized by $\boldsymbol{G} \neq 0$. Here the momentum conservation for the process indicated above would be $\boldsymbol{q} + \boldsymbol{q}' = \boldsymbol{q}'' + \boldsymbol{G}$. As can be seen, in this process the direction of energy flow is reversed. These type of scattering processes were given the name "Umklapp" by Peierls[49], and they give rise to thermal resistance in a material. The scattering rate for a three-phonon scattering process can be computed using Fermi's golden rule [50, 51]:

$$P_i^f(3ph) = \frac{2\pi}{\hbar}|\langle f|V_3|i\rangle|^2\delta(E_f - E_i). \tag{3.45}$$

In the above equation i and f denote the initial and final state, V_3 is the three phonon coupling potential as expressed in Eq. 3.39, and $\delta(E_f - E_i)$ denotes energy conservation between the initial and final states. There are two types of events associated with three-phonon scattering. In the first type of events, called class 1 events or "coalescence processes", a phonon mode ($\boldsymbol{q}s$) scatters by absorbing another mode ($\boldsymbol{q}'s'$) to yield a third phonon mode ($\boldsymbol{q}''s''$). In the second type of

events, called class 2 events or "decay processes" a phonon mode ($\boldsymbol{q}s$) scatters by decaying into two phonon modes ($\boldsymbol{q}'s'$) and ($\boldsymbol{q}''s''$). Both processes satisfy momentum and energy conservation: For class 1 events, these are:

$$\boldsymbol{q} + \boldsymbol{q}' = \boldsymbol{q}'', \quad \hbar\omega(\boldsymbol{q}s) + \hbar\omega(\boldsymbol{q}'s') = \hbar\omega(\boldsymbol{q}''s''), \tag{3.46}$$

while class 2 events we have

$$\boldsymbol{q} = \boldsymbol{q}' + \vec{q}'', \quad \hbar\omega(\boldsymbol{q}s) = \hbar\omega(\boldsymbol{q}'s') + \hbar\omega(\boldsymbol{q}''s''), \tag{3.47}$$

The reciprocal lattice vector $\boldsymbol{G}$ is not explicitly written in the above equations. For class 1 events the scattering rate is given by

$$\begin{aligned} P^{\boldsymbol{q}''s''}_{\boldsymbol{q}s,\boldsymbol{q}'s'} = \frac{2\pi}{\hbar^2}|\langle n_{\boldsymbol{q}s} - 1, n_{\boldsymbol{q}'s'} - 1, n_{\boldsymbol{q}''s''} + 1|V_3|n_{\boldsymbol{q}s}, n_{\boldsymbol{q}'s'}, n_{\boldsymbol{q}''s''}\rangle|^2 \\ \times \delta(\omega(\boldsymbol{q}s) + \omega(\boldsymbol{q}'s') - \omega(\boldsymbol{q}''s'')) \end{aligned} \tag{3.48}$$

where n in the above equation represent the perturbed phonon populations. Substituting V_3 from Eq. 3.39, we obtain

$$\begin{aligned} P^{\boldsymbol{q}''s''}_{\boldsymbol{q}s,\boldsymbol{q}'s'} = 2\pi|\tilde{V}_3(-\boldsymbol{q}s, -\boldsymbol{q}'s', \boldsymbol{q}''s'')|^2 n_{\boldsymbol{q}s} n_{\boldsymbol{q}'s'}(n_{\boldsymbol{q}''s''} + 1) \\ \times \delta(\omega(\boldsymbol{q}s) + \omega(\boldsymbol{q}'s') - \omega(\boldsymbol{q}''s'')) \end{aligned} \tag{3.49}$$

The factor of $1/3!$ in the expression for V_3 is cancelled by the presence of $3!$ equivalent terms involved in the summation over $\boldsymbol{q}, \boldsymbol{q}', \boldsymbol{q}''$. This is due to the fact that the expression for V_3 is cyclically symmetric in $\boldsymbol{q}, \boldsymbol{q}', \boldsymbol{q}''$. Secondly in the expansion of $(a^\dagger_{\boldsymbol{q}s} - a_{-\boldsymbol{q}s})(a^\dagger_{\boldsymbol{q}'s'} - a_{-\boldsymbol{q}'s'})(a^\dagger_{\boldsymbol{q}''s''} - a_{-\boldsymbol{q}''s''})$ only one term, $a_{-\boldsymbol{q}s}a_{-\boldsymbol{q}'s'}a^\dagger_{\boldsymbol{q}''s''}$, survives, as this is the only term that couples the initial state $|n_{\boldsymbol{q}s}, n_{\boldsymbol{q}'s'}, n_{\boldsymbol{q}''s''}\rangle$ with the final state $|n_{\boldsymbol{q}s} - 1, n_{\boldsymbol{q}'s'} - 1, n_{\boldsymbol{q}''s''} + 1\rangle$. The net scattering rate involving a class 1 event can be written as the difference of the forward and back scattering processes. The

expression is given below:

$$P^{\boldsymbol{q}''s''}_{\boldsymbol{q}s,\boldsymbol{q}'s'} - P^{\boldsymbol{q}s,\boldsymbol{q}'s'}_{\boldsymbol{q}''s''} = 2\pi\delta(\omega(\boldsymbol{q}s) + \omega(\boldsymbol{q}'s') - \omega(\boldsymbol{q}''s''))|\tilde{V}_3(-\boldsymbol{q}s, -\boldsymbol{q}'s', \boldsymbol{q}''s'')|^2 \\ [n_{\boldsymbol{q}s}n_{\boldsymbol{q}'s'}(n_{\boldsymbol{q}''s''}+1) - (n_{\boldsymbol{q}s}+1)(n_{\boldsymbol{q}'s'}+1)n_{\boldsymbol{q}''s''}] \tag{3.50}$$

At equilibrium and in the absence of a temperature gradient, the net scattering rate is zero. This yields the principle of detailed balance for the class 1 events:

$$\bar{n}_{\boldsymbol{q}s}\bar{n}_{\boldsymbol{q}'s'}(\bar{n}_{\boldsymbol{q}''s''}+1) = (\bar{n}_{\boldsymbol{q}s}+1)(\bar{n}_{\boldsymbol{q}'s'}+1)\bar{n}_{\boldsymbol{q}''s''} \tag{3.51}$$

that can be written as

$$\bar{n}_{\boldsymbol{q}'s'} - \bar{n}_{\boldsymbol{q}''s''} = \frac{\bar{n}_{\boldsymbol{q}'s'}(\bar{n}_{\boldsymbol{q}''s''}+1)}{(\bar{n}_{\boldsymbol{q}s}+1)} \tag{3.52}$$

To linearize the scattering rates in Eq. 3.50, we expand the perturbed phonon population $n_{\boldsymbol{q}s}$ about the equilibrium in terms of a first order perturbation $\Psi_{\boldsymbol{q}s}$ defined as

$$n_{\boldsymbol{q}s} = \bar{n}_{\boldsymbol{q}s} - \frac{k_B T}{\hbar}\frac{\partial \bar{n}_{\boldsymbol{q}s}}{\partial \omega(\boldsymbol{q}s)}\Psi_{\boldsymbol{q}s} \tag{3.53}$$

leading to

$$n_{\boldsymbol{q}s} = \bar{n}_{\boldsymbol{q}s} + \bar{n}_{\boldsymbol{q}s}(\bar{n}_{\boldsymbol{q}s}+1)\Psi_{\boldsymbol{q}s} \tag{3.54}$$

Substituting Eq. 3.54 into Eq. 3.50, the net scattering rate due to class 1 events can be written as :

$$P^{\boldsymbol{q}''s''}_{\boldsymbol{q}s,\boldsymbol{q}'s'} - P^{\boldsymbol{q}s,\boldsymbol{q}'s'}_{\boldsymbol{q}''s''} = \tilde{P}^{\boldsymbol{q}''s''}_{\boldsymbol{q}s,\boldsymbol{q}'s'}(\Psi^{s}_{\boldsymbol{q}} + \Psi^{s'}_{\boldsymbol{q}'} - \Psi^{s''}_{\boldsymbol{q}''}) \tag{3.55}$$

where

$$\tilde{P}^{\boldsymbol{q}''s''}_{\boldsymbol{q}s,\boldsymbol{q}'s'} = 2\pi\bar{n}_{\boldsymbol{q}s}\bar{n}_{\boldsymbol{q}'s'}(\bar{n}_{\boldsymbol{q}''s''}+1)|\tilde{V}_3(-\boldsymbol{q}s, -\boldsymbol{q}'s', \boldsymbol{q}''s'')|^2 \\ \times \delta(\omega(\boldsymbol{q}s) + \omega(\boldsymbol{q}'s') - \omega(\boldsymbol{q}''s'')) \tag{3.56}$$

Similarly the scattering rate due to class 2 events is expressed as

$$\begin{aligned} P_{\boldsymbol{q}''s''}^{\boldsymbol{q}s,\boldsymbol{q}'s'} &= \frac{2\pi}{\hbar^2}|\langle n_{\boldsymbol{q}s}-1, n_{\boldsymbol{q}'s'}+1, n_{\boldsymbol{q}''s''}+1|\tilde{V}_3|n_{\boldsymbol{q}s}, n_{\boldsymbol{q}'s'}, n_{\boldsymbol{q}''s''}\rangle|^2 \\ &\times \delta(\omega(\boldsymbol{q}s)-\omega(\boldsymbol{q}'s')-\omega(\boldsymbol{q}''s'')) \end{aligned} \tag{3.57}$$

Substituting V_3 from 3.39 we obtain

$$\begin{aligned} P_{\boldsymbol{q}''s''}^{\boldsymbol{q}s,\boldsymbol{q}'s'} &= 2\pi|\tilde{V}_3(-\boldsymbol{q}s,-\boldsymbol{q}'s',\boldsymbol{q}''s'')|^2 n_{\boldsymbol{q}s}(n_{\boldsymbol{q}'s'}+1)(n_{\boldsymbol{q}''s''}+1) \\ &\times \delta(\omega(\boldsymbol{q}s)+\omega(\boldsymbol{q}'s')-\omega(\boldsymbol{q}''s'')) \end{aligned} \tag{3.58}$$

The net scattering rate involvng a class 2 event is

$$\begin{aligned} P_{\boldsymbol{q}s}^{\boldsymbol{q}'s',\boldsymbol{q}''s''} - P_{\boldsymbol{q}'s',\boldsymbol{q}''s''}^{\boldsymbol{q}s} &= 2\pi\delta(\omega(\boldsymbol{q}s)-\omega(\boldsymbol{q}'s')-\omega(\boldsymbol{q}''s''))|\tilde{V}_3(-\boldsymbol{q}s,\boldsymbol{q}'s',\boldsymbol{q}''s'')|^2 \\ &[n_{\boldsymbol{q}s}(n_{\boldsymbol{q}'s'}+1)(n_{\boldsymbol{q}''s''}+1)-(n_{\boldsymbol{q}s}+1)n_{\boldsymbol{q}'s'}n_{\boldsymbol{q}''s''}] \end{aligned} \tag{3.59}$$

Again at equillibrium, the net scattering rate for calss 2 events i zero, yeilding the following the identity for class 2 events

$$\bar{n}_{\boldsymbol{q}s}(\bar{n}_{\boldsymbol{q}'s'}+1)(\bar{n}_{\boldsymbol{q}''s''}+1) = (\bar{n}_{\boldsymbol{q}s}+1)\bar{n}_{\boldsymbol{q}'s'}\bar{n}_{\boldsymbol{q}''s''} \tag{3.60}$$

that can be written as

$$1+\bar{n}_{\boldsymbol{q}'s'}+\bar{n}_{\boldsymbol{q}''s''} = \frac{\bar{n}_{\boldsymbol{q}'s'}\bar{n}_{\boldsymbol{q}''s''}}{\bar{n}_{\boldsymbol{q}s}} \tag{3.61}$$

making use of 3.54, the scattering rate due to class 2 events becomes

$$P_{\boldsymbol{q}s}^{\boldsymbol{q}'s',\boldsymbol{q}''s''} - P_{\boldsymbol{q}'s',\boldsymbol{q}''s''}^{\boldsymbol{q}s} = \tilde{P}_{\boldsymbol{q}s}^{\boldsymbol{q}'s',\boldsymbol{q}''s''}(\Psi_{\boldsymbol{q}}^{s}-\Psi_{\boldsymbol{q}'}^{s'}-\Psi_{\boldsymbol{q}''}^{s''}) \tag{3.62}$$

where

$$\begin{aligned} \tilde{P}_{\boldsymbol{q}s}^{\boldsymbol{q}'s',\boldsymbol{q}''s''} &= 2\pi\bar{n}_{\boldsymbol{q}s}(\bar{n}_{\boldsymbol{q}'s'}+1)(\bar{n}_{\boldsymbol{q}''s''}+1)|\Phi(-\boldsymbol{q}s,\boldsymbol{q}'s',\boldsymbol{q}''s'')|^2 \\ &\times \delta(\omega(\boldsymbol{q}s)-\omega(\boldsymbol{q}'s')-\omega(\boldsymbol{q}''s'')) \end{aligned} \tag{3.63}$$

The net scattering rate involving a class 2 event is

$$
\begin{aligned}
-\frac{\partial n_{\boldsymbol{q}s}}{\partial t}\bigg|_{scatt} &= \sum_{\boldsymbol{q}'s',s''} \Big[(P^{\boldsymbol{q}''s''}_{\boldsymbol{q}s,\boldsymbol{q}'s'} - P^{\boldsymbol{q}s,\boldsymbol{q}'s'}_{\boldsymbol{q}''s''}) + \frac{1}{2}(P^{\boldsymbol{q}'s',\boldsymbol{q}''s''}_{\boldsymbol{q}s} - P^{\boldsymbol{q}s}_{\boldsymbol{q}'s',\boldsymbol{q}''s''}) \Big] \\
&= \sum_{\boldsymbol{q}'s',s''} \Big[\tilde{P}^{\boldsymbol{q}''s''}_{\boldsymbol{q}s,\boldsymbol{q}'s'}(\Psi^{s}_{\boldsymbol{q}} + \Psi^{s'}_{\boldsymbol{q}'} - \Psi^{s''}_{\boldsymbol{q}''}) + \frac{1}{2}\tilde{P}^{\boldsymbol{q}'s',\boldsymbol{q}''s''}_{\boldsymbol{q}s}(\Psi^{s}_{\boldsymbol{q}} - \Psi^{s'}_{\boldsymbol{q}'} - \Psi^{s''}_{\boldsymbol{q}''}) \Big]
\end{aligned}
\tag{3.64}
$$

Substituting the above expression for net scattering rate into Eq. 3.44, the PBE can now be rewritten as

$$
-\boldsymbol{c}(\boldsymbol{q}s).\nabla T\left(\frac{\partial \bar{n}_{\boldsymbol{q}s}}{\partial T}\right) = \sum_{\boldsymbol{q}'s',s''} \Big[\tilde{P}^{\boldsymbol{q}''s''}_{\boldsymbol{q}s,\boldsymbol{q}'s'}(\Psi^{s}_{\boldsymbol{q}} + \Psi^{s'}_{\boldsymbol{q}'} - \Psi^{s''}_{\boldsymbol{q}''}) + \frac{1}{2}\tilde{P}^{\boldsymbol{q}'s',\boldsymbol{q}''s''}_{\boldsymbol{q}s}(\Psi^{s}_{\boldsymbol{q}} - \Psi^{s'}_{\boldsymbol{q}'} - \Psi^{s''}_{\boldsymbol{q}''}) \Big] \tag{3.65}
$$

3.1.4 Single Mode Relaxation Time Approximation

Eq. 3.65 shows that the PBE for the unknown $\Psi^{s}_{\boldsymbol{q}}$ is coupled together with the unknown phonon populations of all other modes ($\Psi^{s'}_{\boldsymbol{q}'}$, $\Psi^{s''}_{\boldsymbol{q}''}$) all over the Brillouin zone. The complexity involved in solving the phonon Boltzmann equation (PBE) based on the three phonon processes lies in the dependence of the distribution function $n_{\boldsymbol{q}s}$ on the occupation of all other states, allowed by energy and momentum conservation. The scattering rate of a mode when the entire system relaxes to equilibrium would in general not be the same as when all other modes are in equilibrium. In the first situation the PBE's of all the different modes $\boldsymbol{q}$s are coupled together and have to be solved simultaneously in a self consistent way [52, 53]. The second situation corresponds to the single mode relaxation time approximation [54, 55, 48, 56, 57]. In this approximation, the PBE is solved for $n_{\boldsymbol{q}s}$ by assuming that $\Psi^{s'}_{\boldsymbol{q}'}$, $\Psi^{s''}_{\boldsymbol{q}''}$ are zero where $\boldsymbol{q}'s'$ and $\boldsymbol{q}''s''$ are modes involved in the scattering of mode $\boldsymbol{q}$s. We first calculate the thermal conductivity in the single mode relaxation time approximation and later compare it with the result obtained from the full self consistent solution of the Boltzmann transport equation. In the single-mode relaxation time approximation, by setting

$\Psi^{s'}_{\boldsymbol{q}'}$, $\Psi^{s''}_{\boldsymbol{q}''} = 0$ and using identities represented by Eqs. 3.52 and 3.61, Eq. 3.64 can be rewritten as,

$$\begin{aligned}-\frac{\partial n_{\boldsymbol{q}s}}{\partial t}\bigg|_{scatt} &= \bar{n}_{\boldsymbol{q}s}(\bar{n}_{\boldsymbol{q}s}+1)\Phi^{s}_{\boldsymbol{q}}\pi \sum_{\boldsymbol{q}'s',s''} \tilde{V}_3(-\boldsymbol{q}s,\boldsymbol{q}'s',\boldsymbol{q}''s'')|^2 \\ &\Big[2(\bar{n}_{\boldsymbol{q}',s'}-\bar{n}_{\boldsymbol{q}''s''})\delta(\omega(\boldsymbol{q}s)+\omega(\boldsymbol{q}'s')-\omega(\boldsymbol{q}''s''))+ \\ &(1+\bar{n}_{\boldsymbol{q}'s'}+\bar{n}_{\boldsymbol{q}''s''})]\delta(\omega(\boldsymbol{q}s)-\omega(\boldsymbol{q}'s')-\omega(\boldsymbol{q}''s''))\Big]\end{aligned} \tag{3.66}$$

Using 3.54, the above equation can be rewritten as

$$-\frac{\partial n_{\boldsymbol{q}s}}{\partial t}\bigg|_{scatt} = \frac{n_{\boldsymbol{q}s}-\bar{n}_{\boldsymbol{q}s}}{\tau_{\boldsymbol{q}s}} \tag{3.67}$$

where $\tau_{\boldsymbol{q}s}$ is the phonon relaxation time and is given by the following expression

$$\begin{aligned}\frac{1}{\tau_{\boldsymbol{q}s}} = 2\Gamma_{\boldsymbol{q}s} =& \pi \sum_{\boldsymbol{q}'s',s''} |\tilde{V}_3(-\boldsymbol{q}s,\boldsymbol{q}'s',\boldsymbol{q}''s'')|^2 \\ &\times \Big[2(\bar{n}_{\boldsymbol{q}',s'}-\bar{n}_{\boldsymbol{q}''s''})\delta(\omega(\boldsymbol{q}s)+\omega(\boldsymbol{q}'s')-\omega(\boldsymbol{q}''s''))+ \\ &(1+\bar{n}_{\boldsymbol{q}'s'}+\bar{n}_{\boldsymbol{q}''s''})]\delta(\omega(\boldsymbol{q}s)-\omega(\boldsymbol{q}'s')-\omega(\boldsymbol{q}''s''))\end{aligned} \tag{3.68}$$

In the above expression $\Gamma_{\boldsymbol{q}s}$ is the full linewidth at half maximum (FWHM). Now solving the PBE assuming a temperature gradient along direction β, we get

$$-\boldsymbol{c}(\boldsymbol{q}s).|\nabla T|_{\beta}\left(\frac{\partial \bar{n}_{\boldsymbol{q}s}}{\partial T}\right) = -\frac{\partial n_{\boldsymbol{q}s}}{\partial t}\bigg|_{scatt} = \frac{n_{\boldsymbol{q}s}-\bar{n}_{\boldsymbol{q}s}}{\tau_{\boldsymbol{q}s}} \tag{3.69}$$

Therefore

$$\begin{aligned}n_{\boldsymbol{q}s}-\bar{n}_{\boldsymbol{q}s} &= -\boldsymbol{c}_{\beta}(\boldsymbol{q}s).|\nabla T|_{\beta}\left(\frac{\partial \bar{n}_{\boldsymbol{q}s}}{\partial T}\right)\tau_{\boldsymbol{q}s} \\ &= -\boldsymbol{c}_{\beta}(\boldsymbol{q}s).|\nabla T|_{\beta}\bar{n}_{\boldsymbol{q}s}(\bar{n}_{\boldsymbol{q}s}+1)\frac{\hbar\omega(\boldsymbol{q}s)}{k_B T^2}\tau_{\boldsymbol{q}s}\end{aligned} \tag{3.70}$$

Substituting the perturbed phonon population obtained above into the expression for heat flux (Eq. 3.42) yields the following expression for thermal conductivity

$$k_{\alpha\beta} = \frac{\hbar^2}{N_0 \Omega k_B T^2} \sum_{\boldsymbol{q}s} c_\alpha(\boldsymbol{q}s) c_\beta(\boldsymbol{q}s) \omega^2(\boldsymbol{q}s) n_{\boldsymbol{q}s}(n_{\boldsymbol{q}s}+1)\tau_{\boldsymbol{q}s} \tag{3.71}$$

3.2 Implementation

Thus, in order to compute thermal conductivity in the single mode relaxation time approximation, the only inputs required are the second-order and the third-order interatomic force constants (IFCs).

Steps involved in the thermal conductivity calculation are outlined below:

1.) The second-order interatomic force constants (IFCs) $\Phi_{\alpha\beta}(\boldsymbol{ob,hb'})$ are obtained. The second-order IFC's allow computation of the dynamical matrix $D_{\alpha\beta}(\boldsymbol{bb'}|\boldsymbol{q})$, whose eigenvalues yield the phonon frequencies and the dispersion, from which the phonon group velocities and Bose-Einstein populations can be computed. The secondorder force constants yield the second derivative of energy with respect to two atomic displacements; as the distance between the atoms increases, these force constants diminish in magnitude. In order to ensure an accurate estimate of dynamical matrix, these force constants have to obtained in real space on a large enough supercell such that the force constants have decayed to negligibly small values. We find that a supercell size of 10x10x10 is enough to ensure this. However, direct calculation of force constants in real space is computationally expensive as it requires using a supercell with thousands of atoms. Instead, first the Brillouin zone is discretized into 10x10x10 grid of $\boldsymbol{q}$ points; then the force constants in $\boldsymbol{q}$ space $\Phi_{\alpha\beta}(\boldsymbol{bb'}|\boldsymbol{q})$ are computed for $\boldsymbol{q}$ belonging to this grid, using density-functional perturbation theory in reciprocal space. This calculation is computationally much cheaper as it involves using the primitive fec unit cell with only two atoms. The force constants in $\boldsymbol{q}$ space, $\Phi_{\alpha\beta}(\boldsymbol{bb'}|\boldsymbol{q})$, are then

inverse Fourier transformed to obtain the force constants in real space:

$$\Phi_{\alpha\beta}(\boldsymbol{ob,hb'}) = \sum_{\boldsymbol{q}} \Phi_{\alpha\beta}(\boldsymbol{bb'}|\boldsymbol{q}) exp(i\boldsymbol{q}.\boldsymbol{h}) \tag{3.72}$$

where $\boldsymbol{q}$ in the above equation now belongs to the 10x10x10 grid in the first Brillouin zone, and $\boldsymbol{h}$ is the lattice vector of a unit cell on a 10x10x10 supercell in real space. The dynamical matrix at any arbitrary $\boldsymbol{q}'$ can now be obtained by a simple Fourier transform of these real space force constants

$$D_{\alpha\beta}(\boldsymbol{bb'}|\boldsymbol{\text{-}q'}) = \frac{1}{\sqrt{m_b m_{b'}}} \sum_{\boldsymbol{h}} \Phi_{\alpha\beta}(\boldsymbol{ob}, \boldsymbol{hb'}) exp(-i\boldsymbol{q'}.\boldsymbol{h}) \tag{3.73}$$

2.) Next, the third-order interatomic force constants $\Phi_{\alpha\beta\gamma}(\boldsymbol{lb}, \boldsymbol{l'b'}, \boldsymbol{l''b''})$ are computed. The third-order IFC's are used to compute the three-phonon scattering matrix elements, which along with the phonon frequencies and populations yield the phonon relaxation times. As in the case of second-order force constants, the third order force constants decay with the distance between atoms and have to be computed on a large enough supercell such that for the farthest atoms in the supercell, these force constants have diminished to negligible values. In the case of second-order force constants this calculation was performed indirectly, the force constants were first obtained in q space and then inverse Fourier transformed to get them in real space. To repeat the same process for the third-order force constants, force constants in $\boldsymbol{q}$ space $\Phi_{\alpha\beta\gamma}(\boldsymbol{qb}, \boldsymbol{q'b'}, \boldsymbol{q''b''})$ need to determined for $\boldsymbol{q}$, $\boldsymbol{q}'$ and $\boldsymbol{q}$" belonging to a chosen grid in the first Brillouin zone. As in the case of second-order force constants, this approach would reduce computational cost as it would allow using the primitive fcc unit cell with only two atoms. The three-phonon matrix elements are then computed using these force constants through Eq. 3.39, which are then used to compute phonon relaxation times using Eq. 3.68.

3.) To compute the thermal conductivity, the first Brillouin zone is discretized into a grid of $\boldsymbol{q}$ points, and the thermal conductivity is computed using Eq. 3.71. At any $\boldsymbol{q}$ in the grid, the phonon frequencies are computed using the second-order force constants obtained in step 1, and the phonon

group velocities are computed from the derivative of the phonon dispersion $\partial\omega/\partial\boldsymbol{q}$, using the central difference technique

$$\boldsymbol{c}(\boldsymbol{q}s) = \frac{\partial\omega(\boldsymbol{q}s)}{\partial\boldsymbol{q}} = \frac{\omega(\boldsymbol{q}+\Delta\boldsymbol{q},s)-\omega(\boldsymbol{q}-\Delta\boldsymbol{q},s)}{2\Delta\boldsymbol{q}} \tag{3.74}$$

Finally, the phonon population is computed using the Bose-Einstein distribution (Eq. 3.41).

4.) To compute the relaxation time of any phonon mode $\boldsymbol{q}$, the Brillouin zone is again discretized into a grid of $\boldsymbol{q}'$. The relaxation time is then computed by evaluating the sum in Eq. 3.68. The convergence of the computed relaxation time with respect to the size of the $\boldsymbol{q}$' grid is studied. It is found that for a grid of size 30x30x30, relaxation times are sufficiently converged. Also to compute the relaxation time, the delta function for the energy conservation in Eq. 3.68 is replaced by a Gaussian

$$\delta(\omega) = \frac{1}{\sqrt{\pi}\epsilon} exp(-(\omega/\epsilon)^2) \tag{3.75}$$

$\epsilon = 2.5cm^{-1}$ along with a $\boldsymbol{q}'$ grid of size 30x30x30 is found to lead to reasonably converged relaxation times.

5.) Finally, the convergence of the computed thermal conductivity with respect to the size of the $\boldsymbol{q}$ grid in the first Brillouin zone is studied. The converged result is taken to be the thermal conductivity in the single mode relaxation time approximation. For all density-functional perturbation theory calculations a 8x8x8 Monkhorst- Pack [58] mesh is used to sample electronic states in the Brillouin zone and an energy cutoff of 20 Ry is used for the plane-wave expansion. Convergence of all quantities with respect to these parameters is carefully tested. First-principles calculations within density-functional theory are carried out using the PWscf and PHonon codes of the Quantum-ESPRESSO distribution [59] with norm-conserving pseudopotentials based on the approach of von Barth and Car [60].

Chapter 4

Understanding FDTR Measurement Procedure and Technique Through the Measurement of GaX (X = P, As, Sb)

4.1 Introduction

Group III phosphide compounds, because of their intriguing physical features, become very suitable for optoelectronic applications, and have been attracting massive attention in the research community [61, 62]. Gallium Phosphide (GaP) is one of the most commonly known materials from this group of materials and is being widely studied in comparison to other Group III phosphides [63, 64, 65, 66, 67, 68, 69, 70, 71, 72, 73]. GaP has been reported to exhibit Zinc-Blende structure. Due to its bandgap of 2.26 eV, it becomes an essential part in the high bandgap solar cell in multijunction systems. Its other applications are in the fields of optical devices, light emitting diodes, photocells and solar cells [74]. Gallium Arsenide (GaAs) is another well-known semi-conductor material with a direct bandgap of 1.42 eV, garnering attention to its applications towards device physics [75]. GaAs is considered to be a well-suited material for the fabrication of photovoltaic devices [76], heterostructures [77], semiconductor lasers [78] and light emitting diodes [79]. Gallium Antimonide (GaSb) is another member of the III-V compound semiconductor family, which has shown tremendous promise in the field of devices. It's commonly known to have shown potential in the areas of low threshold voltage laser diodes [80, 81], high quantum efficiency photodetectors [82], high frequency devices and as superlattices for improved optical and transport characteristics [83, 84]. It is also used in booster cells and thermophotovoltaic cells [85].

The analysis done in this chapter, serves as a practice exercise for us to gain more confidence and familiarity in defining and understanding the suitable procedure for thermal property characterization using FDTR. The prescribed approach to thermal analysis by this method is affirmed by

being able to replicate the thermal properties of GaX materials as mentioned in the literature, by the virtue of the materials having been studied and analyzed extensively for various applications. To commence our analysis, The GaP crystal substrate was procured from MTI Corporation [86] and the GaAs and GaSb crystal substrates we received from Dr. Sellers's lab. We used Sapphire (purchased from SPI Materials) polished on both the sides as the reference sample for transducer characterization.

4.2 Sample Preparation and Transducer Layer Characterization

As discussed in the above sections, the essential first step in this process was to deposit a thin transducer layer comprised of gold on top of the reference Sapphire sample as well as the samples under investigation. This was done using a Kurt J Lesker thermal evaporator, using a 99.9 percentage pure gold nugget as a target material. The deposition is done under a strong vacuum of 10^{-6} Torr and the deposition rate is kept at 1Angstrom/s. Some other parameters and settings are used to ensure a high quality uniform thin film is produced with a certain consistency, as this can be extremely influential in the characterization process. In the deposition chamber, there is a sample holder on to which the samples are mounted using a high temperature double sided Kapton tape, to keep the samples secured during the deposition process, as the sample holder is kept under a small rotational speed, which ensures the uniformity of the film, during the deposition process.

Another important consideration while placing the samples on the sample holder is that the reference Sapphire samples were kept as close as possible to the GaP, GaAs and GaSb respectively, leading us towards making an assumption that the transducer properties evaluated during the characterization of the reference samples, will exihibit similar properties on the sample under study. In our case ,the GaAs and GaSb samples were coated in the same run whereas GaP was coated in a different run. From Table 4.1, we can evidently see the difference in the gold thermal

conductivity (k_{Au}) and the gold film thickness (t_{Au}) values for the reference sample. Table 4.1 is also an indication of how all the runs are not the same and the effect of evaporator conditions in each run determines the properties of the transducer layer, making transducer characterization a significant first step towards thermal property characterization using FDTR.

Table 4.1: Transducer layer characterization for GaP, GaAs, and GaSb.

Material	**Au Transducer Layer** k $(W m^{-1} K^{-1})$	**Au Transducer Layer** t *(nm)*
GaP	164 ± 21.23	164 ± 11.48
GaAs	199 ± 23.88	120 ± 8.40
GaSb	199 ± 23.88	120 ± 8.40

4.3 Thermal Conductivity Results and Discussion

To obtain the transducer layer properties using the reference sample, we first measure the phase lag plot of the reference sample.

Through the model tab, we then replicate the reference sample and the transducer system in the model. Both the gold transducer layer and the Sapphire substrate, are characterized by their volumetric heat capacity (C_{p}), cross-plane thermal conductivity$(k_{\perp})$, in-plane thermal conductivity $(k_{\parallel})$, and thickness. Another important parameter in the fitting model is the thermal boundary conductance (TBC) at the Au/Sapphire thin film interface. Here in our case, the properties that are known to us are of the reference Sapphire sample i.e. its volumetric heat capacity, its thermal conductivity and its thickness. We consider these to be our fixed input parameters. The parameters that are unknown to us i.e. the thermal properties of the transducer, transducer CTR, its thickness and the boundary conductance will be evaluated by considering them as free parameters, whose values can be changed, until the theoretically computed phase lag from the set of fixed and free parameters fits to the measured phase lag. Another important parameter for the fitting analysis is

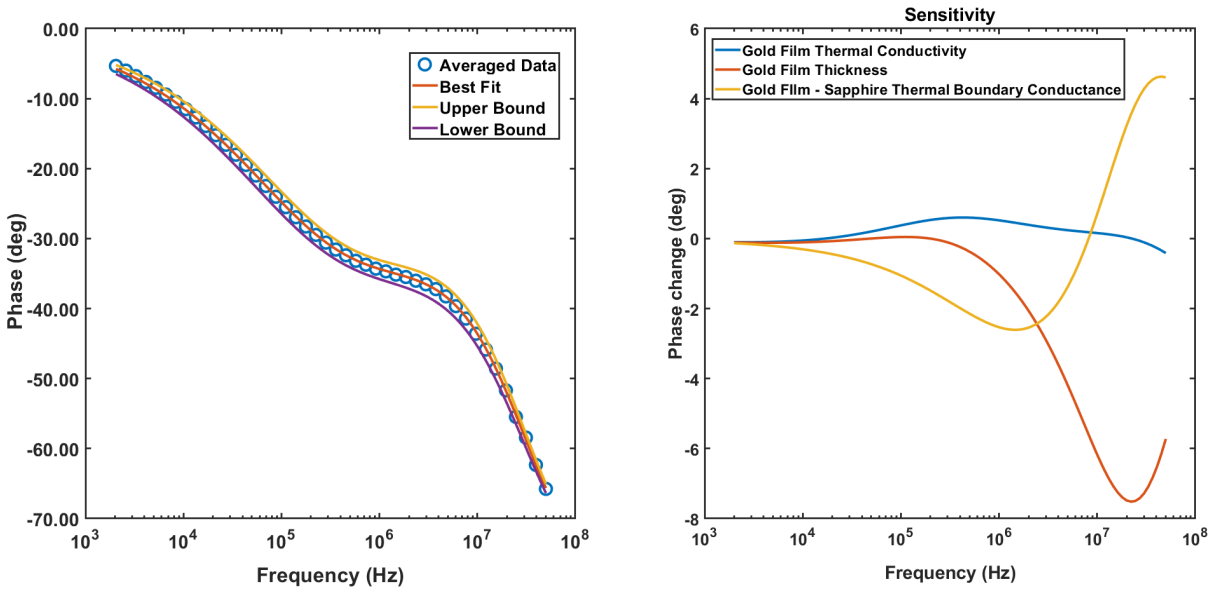

(a) (b)

Figure 4.1: Characterizing of Sapphire transducer involving a) phase lag plot b) sensitivity plot

the laser spot size. The laser spot size determines the size of the heat source on the sample surface, which is an important parameter used in the calculation of the phase lag using the 2D heat conduction model. Through this process, we are able to determine the properties of the transducer layer on the GaP, GaAs and GaSb samples.

We then measure and plot the phase lag of the probe laser with respect to the modulation frequency for all the GaX samples. By utilizing using the transducer parameters from Table 4.1, we then estimate the thermal properties of the respective crystals, through the curve fitting analysis by doing a 3-parameter curve fit where the fitted parameters for the samples are their cross-plane thermal conductivity, laser spot size and the thermal boundary conductance between the gold thin film and the GaP, GaAs and GaSb surfaces. Fig. 4.2 shows that the best curve fit for all the three samples, where the profile of the phase lag data for distinctly different samples seems to be very similar in nature. The figure also shows the variance in the curve fit line, if the thermal conductivity is varies by $\pm$ 20%. The significant difference in the curve fit profiles for both the thermal conductivities is the first indication the measurement done is sensitive to the property of

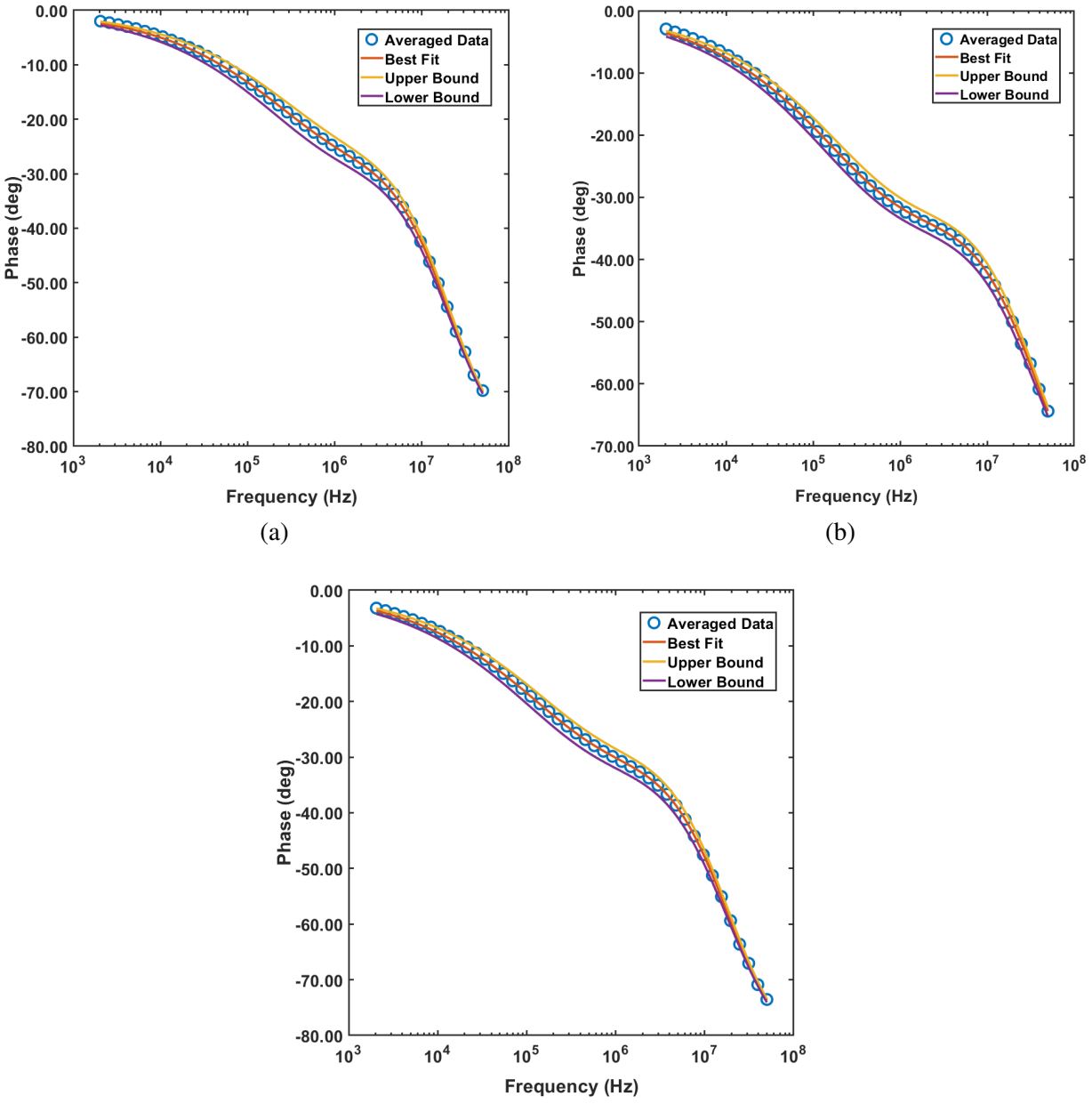

Figure 4.2: Best curve fitting analysis for a) GaP b) GaAs c) GaSb

cross-plane thermal conductivity. It is important that the measurement is sensitive to the parameters we desire to evaluate, which corresponds to the strength of the signal, and stronger the signal, the more confident we are on the value that has been estimated from the curve fit analysis. Also from Table 4.2, we can observe that the measured k values for GaP, GaAs and GaSb are in good

agreement to the values available in the literature.

Table 4.2: Curve fit solutions with their uncertainties for GaP, GaAs, and GaSb.

Material	$C_{\textbf{literature}}$ $(10^6\ J\,m^{-3}K^{-1})$	k $(W\,m^{-1}K^{-1})$	C $(10^6\ J\,m^{-3}K^{-1})$	**TBC** $(MW\,m^{-2}K^{-1})$
GaP	1.78	92.7 ± 4.64	1.83 ± 0.18	50.4 ± 5.04
GaAs	1.76	39.3 ± 1.97	1.51 ± 0.14	64.4 ± 5.80
GaSb	1.31	29.4 ± 1.47	1.51 ± 0.14	32.5 ± 3.25

Fig. 4.3 depicts an alternative method for the sensitivity analysis, where we plot the absolute change in the phase experienced by the parameters during our measurement. We observe that the GaX system is insensitive to k_{Au}'s cross-plane and in-plane thermal conductivities. Similar insensitivity towards k_{Au}'s cross-plane and in-plane thermal conductivities for the GaAs and GaSb was observed, hence they were not plotted in the figure, due to their insignificance. This insensitivity to the gold thin film's cross-plane and in-plane thermal conductivities on the GaX crystals arises because the thermal conductivities of these materials is greater than 10 $\text{Wm}^{-1}\text{K}^{-1}$. Due to this, the heat quickly diffuses from the transducer surface to the crystal, leading to no signal sensitivity to these parameters. This can be verified by varying the input values for k_{Au} in the curve fit analysis. When the input values for gold are varied, the fit does not change and the adjusted/fitted thermal conductivity values for the GaP, GaAs and GaSb remains unaffected. This does not negate the step for characterization of the transducer from the reference sample, as the initial guess for the best curve fit analysis.

For the cross-plane and in-plane thermal conductivities in all these materials, the solution is sensitive to these properties, with the phase change profiles across the modulation frequency range being distinct in comparison to one another. Their magnitude of phase change at the peak is similar, indicating that the crystals are isotropic in nature. This sensitivity is because in the low frequency range, the thermal penetration depth (121μm to 383 nm for GaSb, 141μm to 444 nm for GaAs and 199μm to 628 nm for GaP across the modulation frequency range of 500 Hz to 50 MHz) is larger

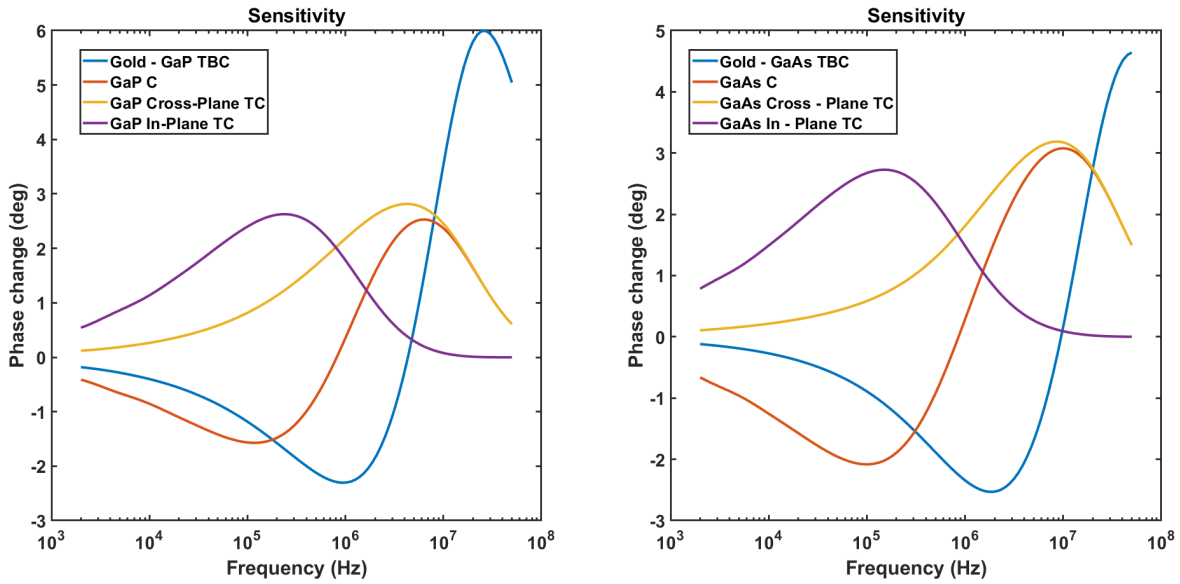

(a)

(b)

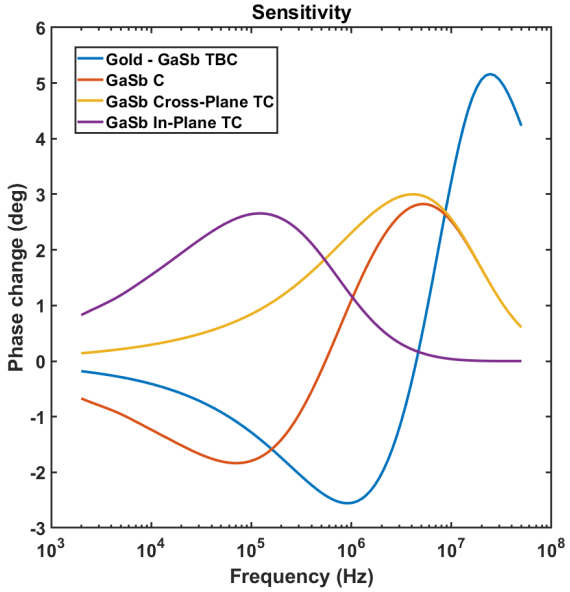

(c)

Figure 4.3: Plotting parameter sensitivities to the measurement as a function of probe beam phase change in degrees for a) GaP b) GaAs c) GaSb

than the spot size and the thermal transport regime is 2D, which leads to the solution's sensitivity to in-plane thermal conductivity.

When the modulation frequency range is high, the regime transitions to 1D as the thermal

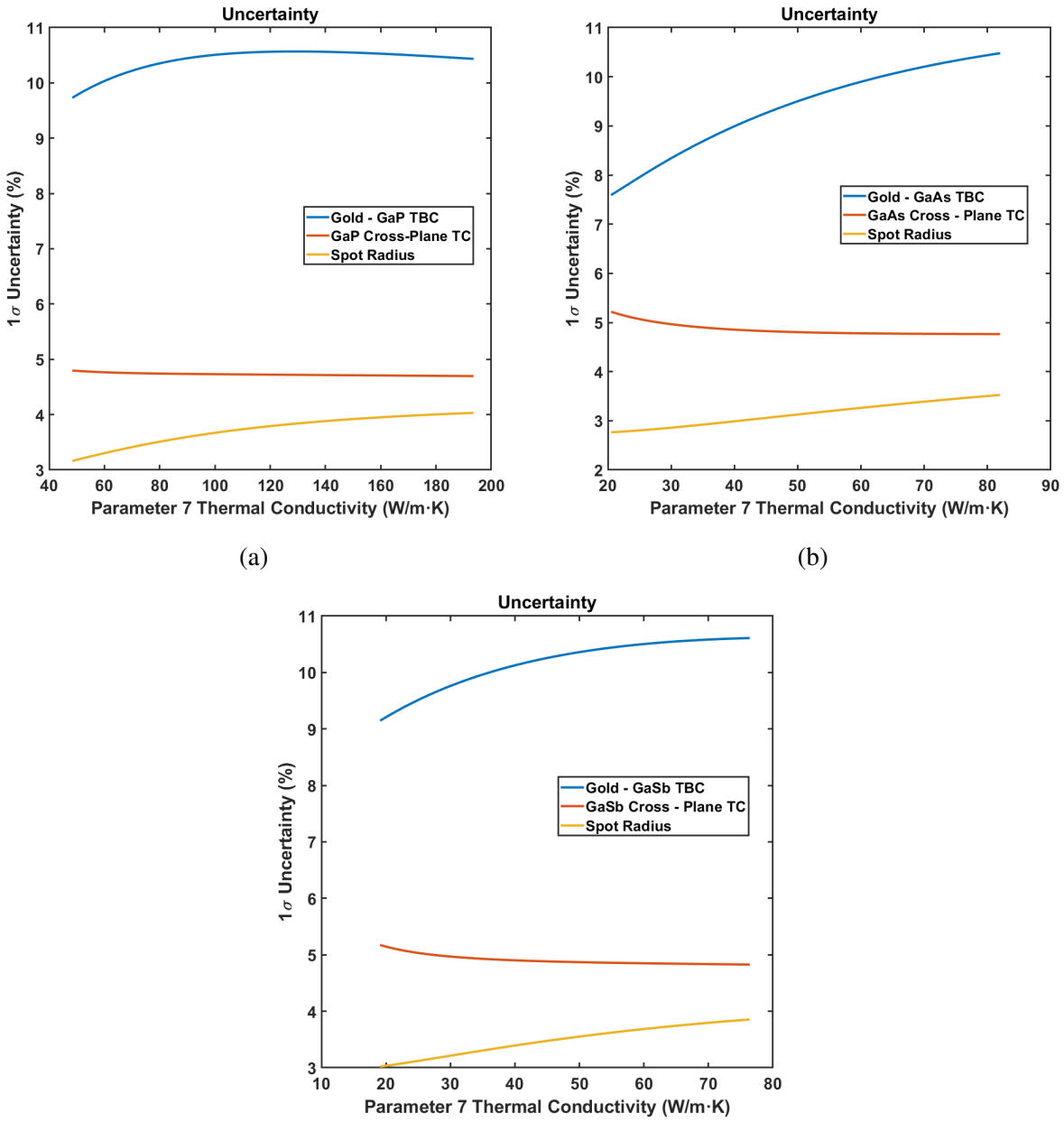

Figure 4.4: Determining the calculated uncertainty of fitted parameter in the best curve fit analysis of a) GaP b) GaAs c) GaSb with the thermal conductivity as a varying parameter

penetration depth becomes smaller than the spot size of the laser, which gives rise to the decrease in the sensitivity to the in-plane thermal conductivity and increased sensitivity to cross-plane thermal conductivity. Hence, we can measure both the in-plane and the cross-plane thermal conductivities

from this curve fit solution, independently.

Fig. 4.4 shows the change in uncertainty values of the fitted parameters, with respect to the thermal conductivity of the material under study. The uncertainty values for the measurements are mentioned in Table 4.2.

The results from the Monte-Carlo simulations for all the crystals are shown in Fig. 4.5. Here we assume that the parameters used in the analysis have a normal distribution about their mean with a standard deviation associated to their measurements separately. Now, FDTR data distributions for the fitted parameters are generated by randomly varying any of the input parameters. The response of the fitted parameter to the randomly changing initial guesses of the input parameter is also a normal distribution about a mean value. This global minima of the normal distribution is considered to be the best value of the fitted parameter that corresponds to the best curve fit in the analysis. This Monte-Carlo analysis corroborates the validity of the values we get for the fitted parameters.

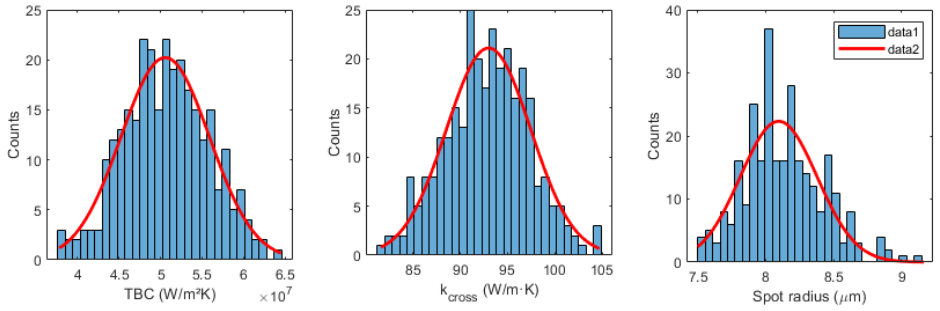

(a)

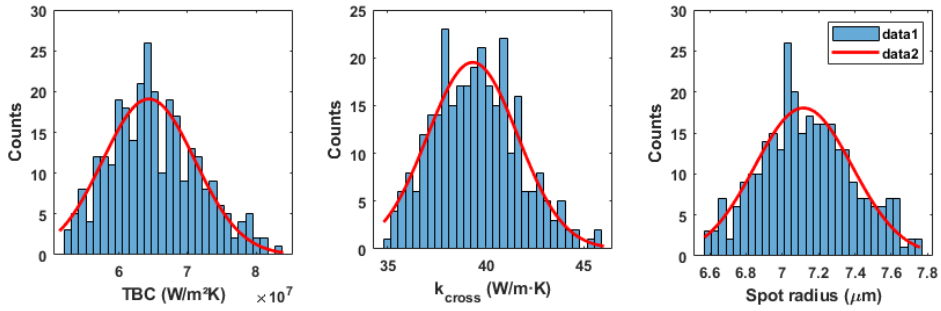

(b)

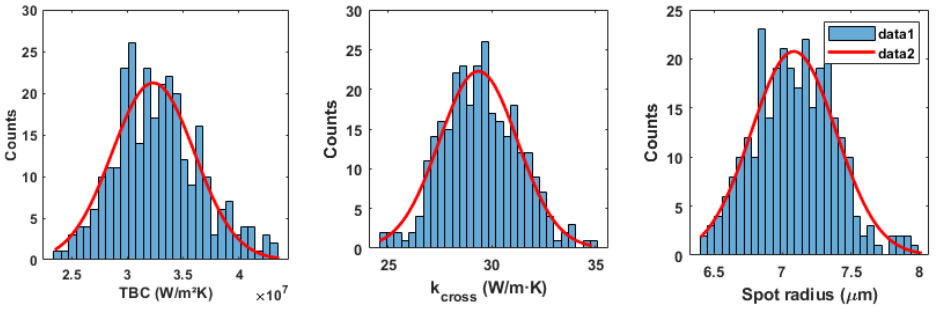

(c)

Figure 4.5: Monte Carlo simulation results for a) GaP b) GaAs c) GaSb

Chapter 5

Length Dependence Thermal Conductivity of Zinc Selenide (ZnSe) and Zinc Telluride (ZnTe) – A Combined First Principles and Frequency Domain ThermoReflectance (FDTR) Study)

5.1 Background

Zinc Chalcogenides (ZnX, X=S, Se and Te) are II-VI wide band gap semiconductors that crystallize in zinc-blende structure[87, 88, 89, 90, 91, 92] and are mainly studied for catalysis [93], electronic [94] [95], structural [95], opto-electronic [96], thermal [90] [97]and thermoelectric properties [96]. In recent times, thin films and nanostructured ZnSe have been widely investigated [89] [96], however, their thermal conductivity dependence on size is unknown. In this chapter, we quantify the bulk material thermal conductivity and length dependent lattice thermal conductivity (k) of ZnSe and ZnTe by solving phonon Boltzmann transport equation (PBTE) coupled with harmonic and anharmonic interatomic force interactions derived from density-functional theory [98, 99, 100]. The bulk material thermal conductivities for both the materials are measured experimentally using FDTR, and these results are then compared to the computational results for the thermal properties of the bulk system, to determine the degree of agreement between the two methods, applied in this analysis.

We first discuss the details of computation of bulk and length dependent k of ZnSe and ZnTe using first principles calculations where we explore the evaluation of various parameters such as phonon dispersions, phonon group velocities, phonon scattering rates, phonon meanfreepaths and mode dependent contribution of transverse acoustic (TA), longitudinal acoustic (LA) and optical phonons for both ZnSe and ZnTe, as well as the length dependence and meanfreepath accumulation of k for both the material systems under study. The details of analysis done using FDTR

measurement of *k* for polycrystalline ZnSe and ZnTe also discussed in detail in the results and discussion.

5.2 Computational Details

Thermal conductivity in this work is computed by solving the phonon Boltzmann transport equation (PBTE) described below,

$$-\mathbf{c}\left(\mathbf{q}s\right)\nabla T\left(\frac{\partial n_{\mathbf{q}s}}{\partial T}\right)+\frac{\partial n_{\mathbf{q}s}}{\partial T}|_{scatt}=0 \tag{5.1}$$

where, $n_{\mathbf{q}s}$ is the population of phonon mode with wave-vector $\mathbf{q}$ and polarization s, T is temperature and $\mathbf{c}\left(\mathbf{q}s\right)$ is the phonon group velocity computed using $\mathbf{c}\left(\mathbf{q}s\right)=\partial\omega_{\mathbf{q}s}/\partial\mathbf{q}$, ($\omega_{\mathbf{q}s}$ represents the frequency of phonon mode $\mathbf{q}s$). The equation represents a balance between change in phonon population due to temperature gradient (first term in the equation) and change in population due to scattering (second term). In this work, PBTE is solved exactly for phonon population using QUANTUM ESPRESSO thermal2 code (reference is needed). Knowledge of perturbed phonon populations allows computation of thermal conductivity.

The only ingredients required to compute all phonon properties involved in PBTE are the second order (harmonic) and third-order (anharmonic) interatomic force interactions. These force interactions were derived accurately in this work from first-principles. Harmonic force interactions are needed to compute phonon frequencies, group velocities and populations while anharmonic force interactions enable computation of phonon scattering. Harmonic interactions were derived using the PHONON code [101], while anharmonic interactions were derived using D3Q package [102] [103], both within the QUANTUM ESPRESSO density-functional theory (DFT) code.

All the first principles calculations were performed using plane-wave based QUANTUM ESPRESSO [59] package. We used local density approximation (LDA) [104] and norm-conserving pseudopotentials for electronic calculations. Calculations were carried out with plane-wave en-

(a) (b)

Figure 5.1: Crystal structure of a) ZnSe b) ZnTe

ergy cut-off of 80 Ry and Monkhorst-Pack [58] k-point mesh of 12 x 12 x 12 was used for integration over Brillouin zone. Crystal structure was relaxed until the total force acting on each atom diminished below 1e-5 eV/Å. Optimized lattice constants of *Zinc-blende* ZnSe and ZnTe were determined to be a=5.6 Å and a=6.138 Å. Dynamical matrices were computed on 8 x 8 x 8 **q**-grid mesh. Inverse Fourier transform was used to convert these matrices in **q**-space into 2^{nd} order force constants (harmonic) in real space on an 8 x 8 x 8 supercell. Anharmonic (3^{rd} order) interatomic force constants were similarly first computed on 4 x 4 x 4 **q**-grid using QUANTUM ESPRESSO D3Q [101, 102, 103] package and then inverse-Fourier transformed to obtain the force constants in real space. Lattice thermal conductivity is calculated by solving Peierls-Boltzmann transport equation (PBTE) [101] [103] [105]iteratively within QUANTUM ESPRESSO thermal2 code [101, 102, 103]with 30 x 30 x 30 **q**-mesh. Casimir scattering [106] is imposed for length dependence *k* calculations.

5.3 Sample Preparation

The ZnSe and ZnTe bulk crystals were purchased from MTI Corporation. The gold pellet for the deposition of gold [36] [46] [107]thin film on bulk polycrystalline ZnSe was purchased from Kurt. JLesker Company (99% purity). We use Lesker Nano36 Evaporator thermal evaporator, (part of Microfabrication Research & Education Center at University of Oklahoma) to deposit 100nm of gold film. After this, the sample was placed carefully on a glass slide using double sided carbon

tape, making it ready for measurement using FDTR.

5.4 Results and Discussions

5.4.1 Computational Analysis

Temperature dependent lattice thermal conductivity(k) of Zinc Selenide (ZnSe) and Zinc Telluride (ZnTe) derived from first-principles computations is shown in Figs. 5.2a and 5.2b respectively. At room temperature (300K), k of 23.2 W/m-K is computed for the naturally occurring ZnSe in close agreement with the previously reported experimental value [90].

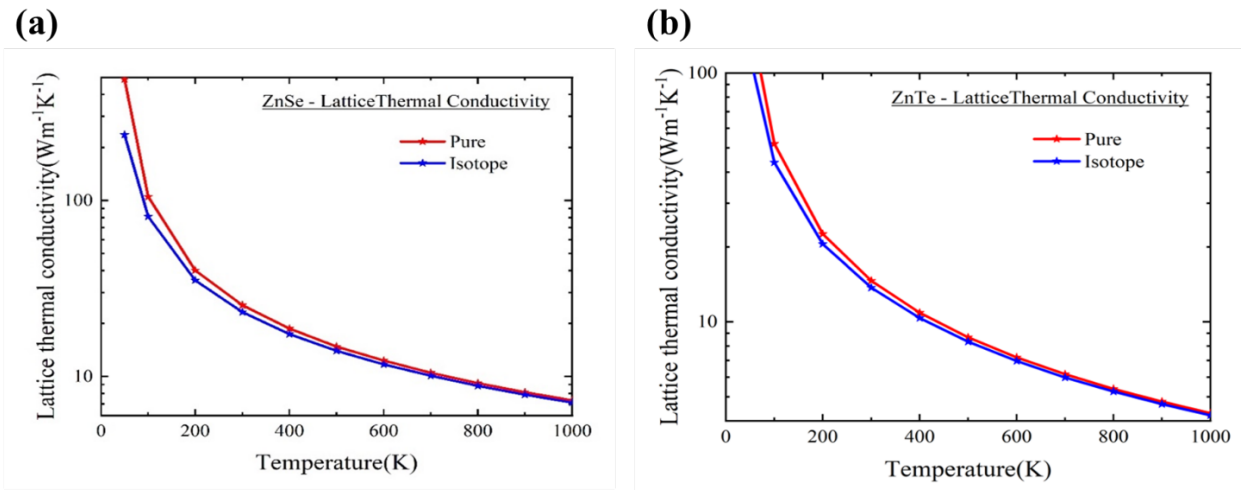

Figure 5.2: Lattice thermal conductivity of pure and naturally occurring a) ZnSe and b) ZnTe.

Length dependent k of ZnSe nanostructures was computed from first principles calculations by imposing Casimir/boundary scattering [106] and is shown in Fig. 5.4a. k value of ZnSe is observed to decrease significantly from 22.92 W/m-K to 1.79 W/m-K as the length scale is diminished from 10 m to 10 nm (Fig. 5.4a). Bulk k of ZnTe is computed to be 13.72 W/m-K for the naturally occurring case and is again in close agreement with the previously reported values [108]. k value of ZnTe is also observed to decrease significantly from 12.65 W/m-K to 1.24 W/m-K as the length scale is diminished from 10 m to 10 nm (Fig. 5.4b). We investigated the phonon dispersion,

phonon group velocity, phonon scattering rate and phonon mean free path in detail to explain these thermal conductivity results.

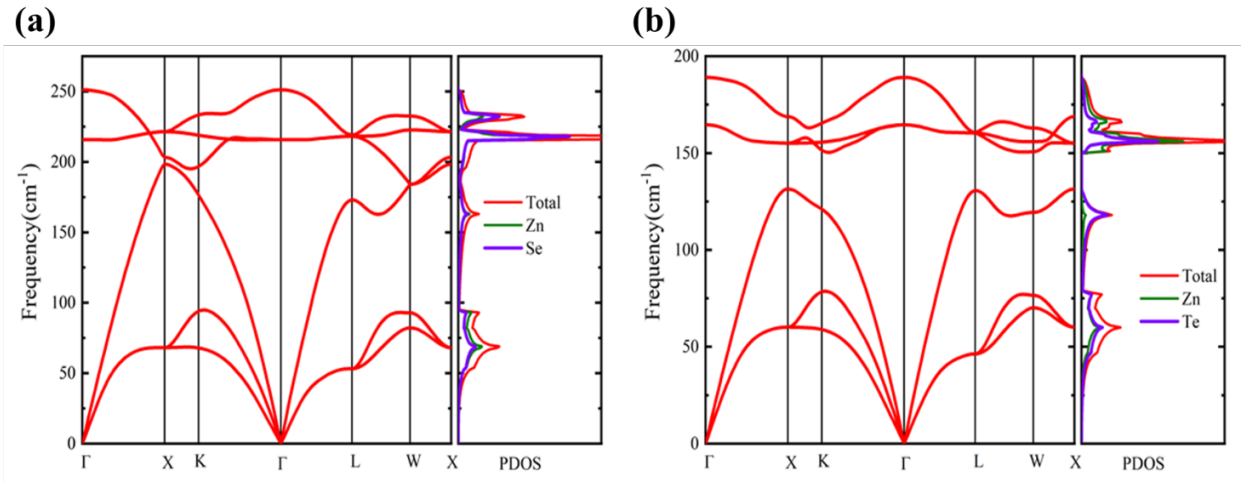

Figure 5.3: Phonon Density of States of a) ZnSe b) ZnTe

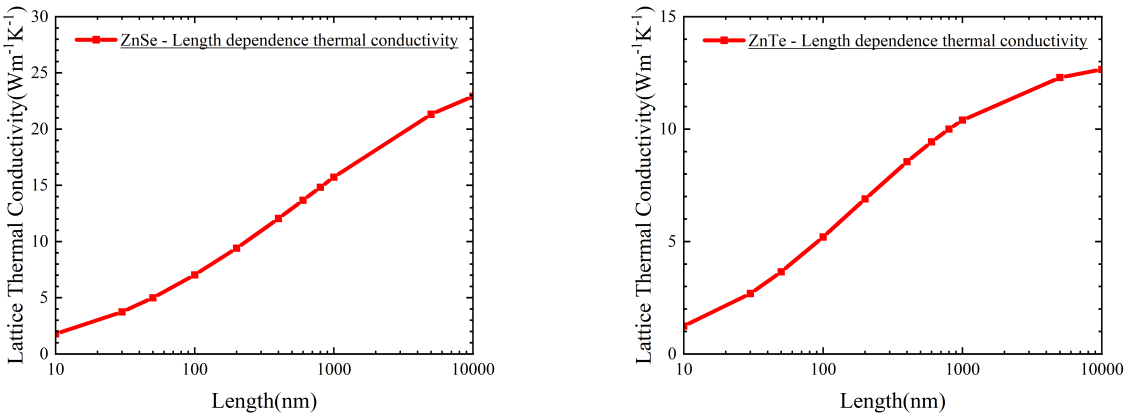

Figure 5.4: Length dependent thermal conductivity of isotopically disordered a) ZnSe b) ZnTe

We first compare the thermal conductivity accumulation with respect to phonon mean freepath (MFP) in Fig. 5.5a and Fig. 5.5b for ZnSe and ZnTe respectively. Fig. 5.5a and Fig. 5.5b represent the accumulated thermal conductivity (k accu) of ZnSe and ZnTe as a function of the mean free path length [109] Contributions of transverse acoustic (TA), longitudinal acoustic (LA) and optical

phonons to overall thermal conductivity are shown in Figs.5.6a and Fig. 5.6b for ZnSe and ZnTe respectively.

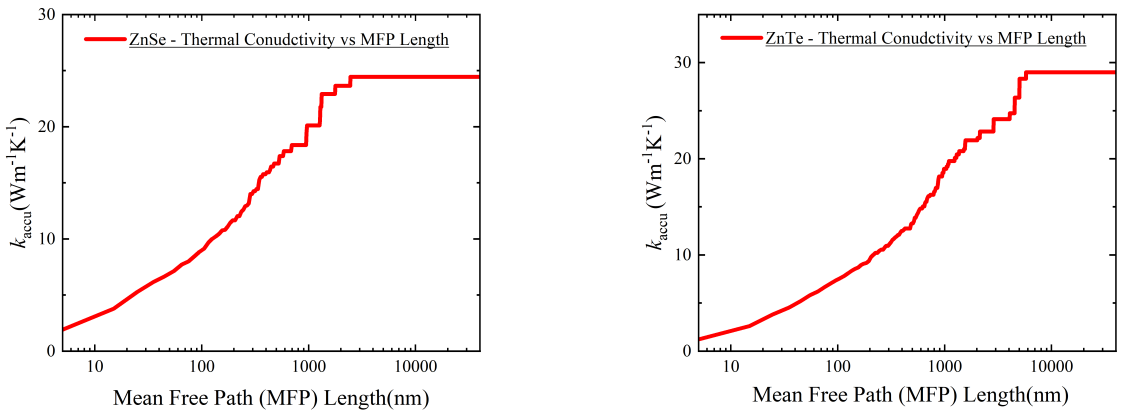

(a) (b)

Figure 5.5: Mean free path length dependent thermal conductivity of isotopically disordered a) ZnSe b) ZnTe

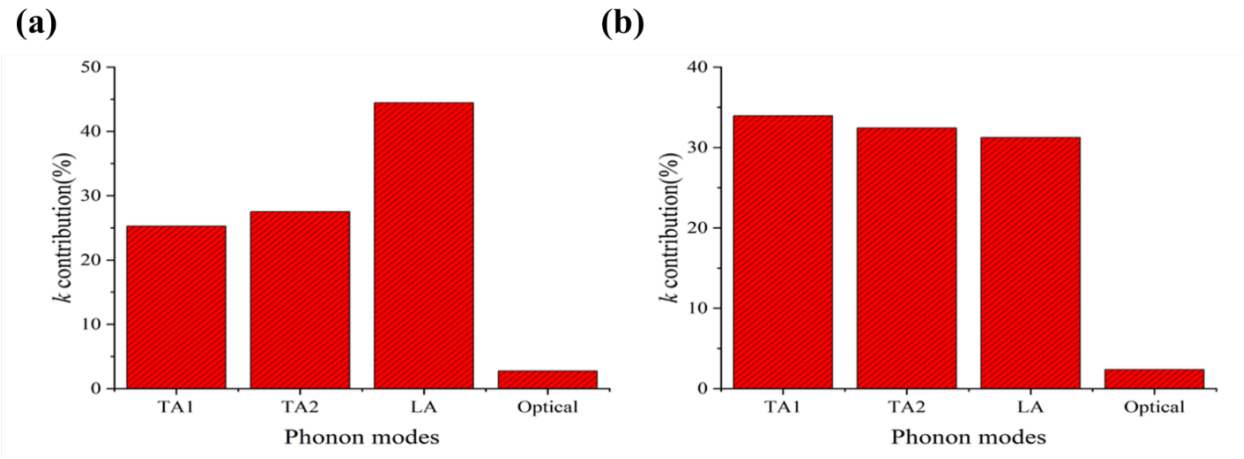

Figure 5.6: Thermal conductivity contribution from TA, LA and optical; phonon modes for a) ZnSe and b) ZnTe

Phonon line width (inverse of lifetime) are shown in Figs. 5.7a and Fig. 5.7b and phonon group velocities are shown in Figs. 5.8a and 5.8b for ZnSe and ZnTe respectively. In ZnSe, the contribution of LA phonons to overall thermal conductivity is higher than TA and optical phonons

(Fig. 5.6a). This can be understood by noticing that LA phonons have higher phonon group velocities (Fig. 5.8a), and their scattering rates (Fig. 5.7a) are lower than TA phonons (in the low frequency range).

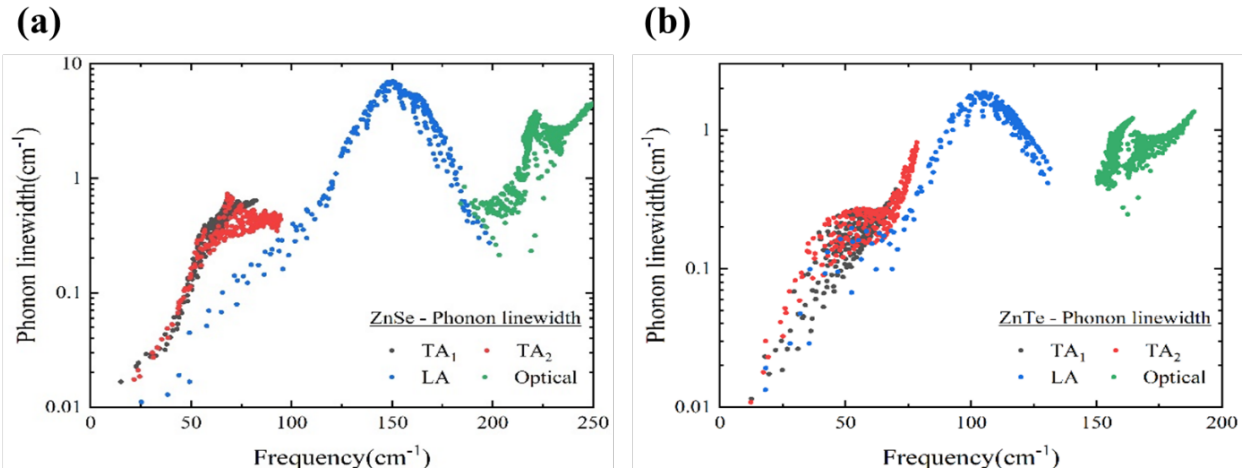

Figure 5.7: Phonon scattering rates of a) ZnSe b) ZnTe

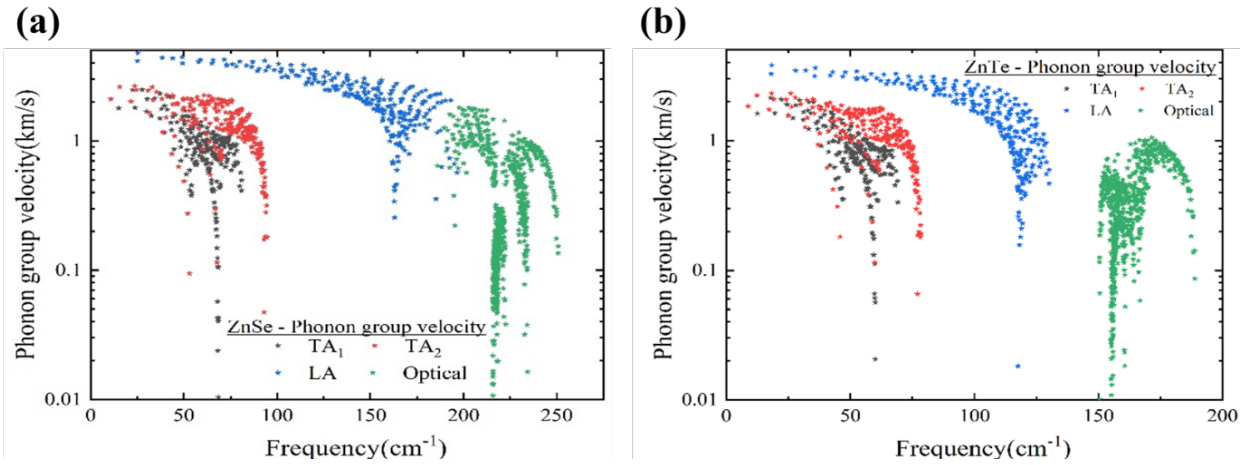

Figure 5.8: Phonon group velocities of a) ZnSe b) ZnTe

LA phonons contribute almost 44.5% to overall thermal conductivity in ZnSe. In case of ZnTe, the contribution of TA_1, TA_2 and LA phonons are $\sim$34%, 32% and 31% respectively at 300 K.

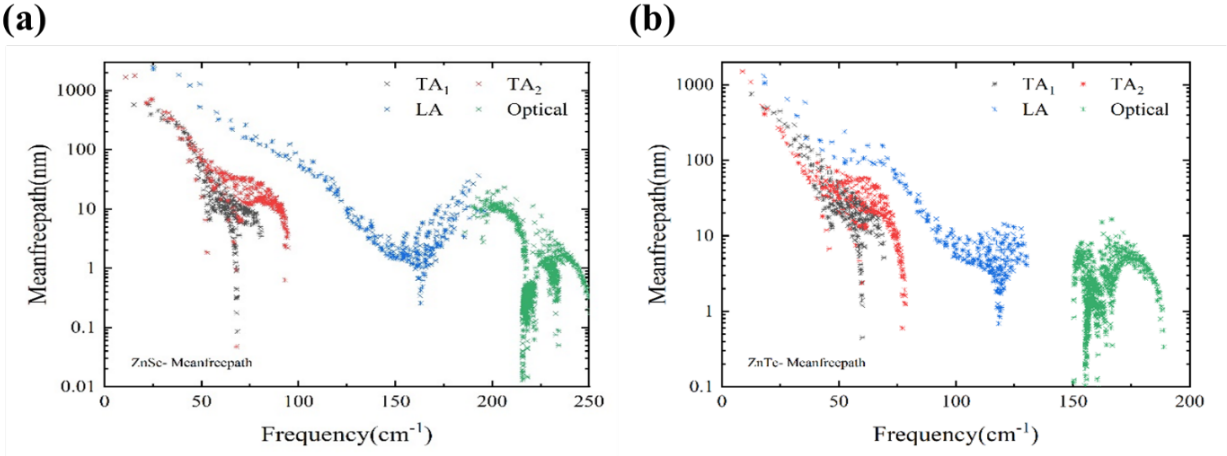

Figure 5.9: Phonon Mean free paths of a) ZnSe b) ZnTe

5.4.2 Thermal Conductivity Measurements - Experimental Analysis

The experimentally measured thermal conductivity values of Zinc Selenide (ZnSe) and Zinc Telluride (ZnTe) using FDTR were $\sim$17 W/m-K and 14 W/m-K respectively at room temperature. Comparing experimental thermal conductivity results from FDTR and theoretical results as shown in Figs. 5.4a and 5.4b, we can determine that the grain sizes of the ZnSe and ZnTe samples obtained from the MTI Corp. are around 2μm and more than 10μm respectively [110]. The measurement of thermal conductivities of polycrystalline ZnSe and ZnTe using FDTR is achieved by curve fitting method as explained in the experimental setup. The blue circles (in Fig.5.10) represent the phase-lag data that has been measured using the FDTR setup where in the frequency of lock-in amplifier was set at 1MHz and the laser power of the pump and theprobe lasers were set at 20mW and 5mW respectively for all samples measured in this work. The solid line represents the best fit curve, which is obtained by a 2D heat conduction mathematical model which utilizes known input parameters such as volumetric heat capacity of the gold film, gold film thermal conductivity, film thickness, volumetric heat capacity of the material under investigation, the thickness of the material under investigation and the laser spot size. The properties of gold film and its thickness are determined by depositing the gold film over a substrate with known properties, namely, fused

Silica (k ∼1 W/m-K) and Sapphire (k ∼35 W/m-K).

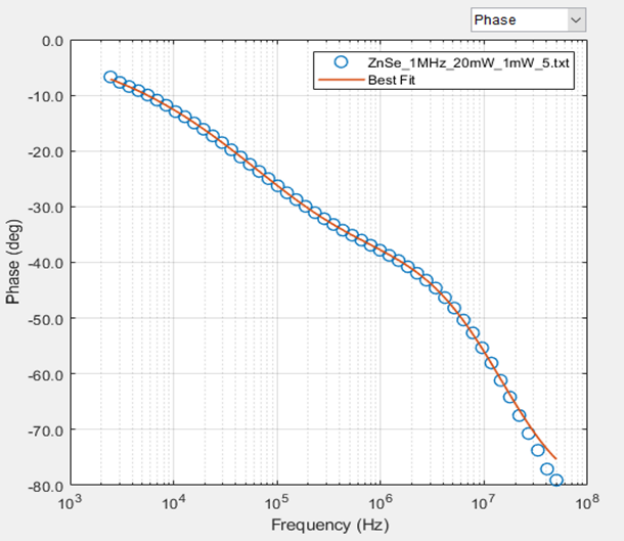

Figure 5.10: FDTR data for curve fitting analysis to calculate the thermal properties of ZnSe measured at a lock-in frequency of 1MHz along with pump and probe powers at 20 and 1mW respectively

This results in accurate determination of the properties of the gold thin film. The volumetric heat capacities of ZnSe and ZnTe are obtained by multiplying the density (g/cm^3) and specific heat (J/Kg K). These details are available on the datasheet of the ZnSe and ZnTe on MTI Corporation's website [86]. The only unknown property in our study is the thermal conductivity of ZnSe and ZnTe, which leads to a single parameter fit.

For the measured thermal conductivity to be accurate, the measured data and the predicted phase-lag from heat conduction model should agree very well. As shown in Fig.5.10, the best fit curve agrees very well with the measured phase-lag values (represented by blue circles). The figure is representative of the agreement between the measured phase data and the phase data generated using the mathematical model which utilizes the input parameters mentioned earlier in the section.

We next describe the sensitivity analysis which is important in ascertaining the accuracy of measured thermal conductivity values. Insensitive parameters can be fixed as input parameters in the model as they do not affect the curve fitting, and this reduces the number of free parameters to be fitted. Sensitive parameters are seen to have a significant difference in the upper and lower

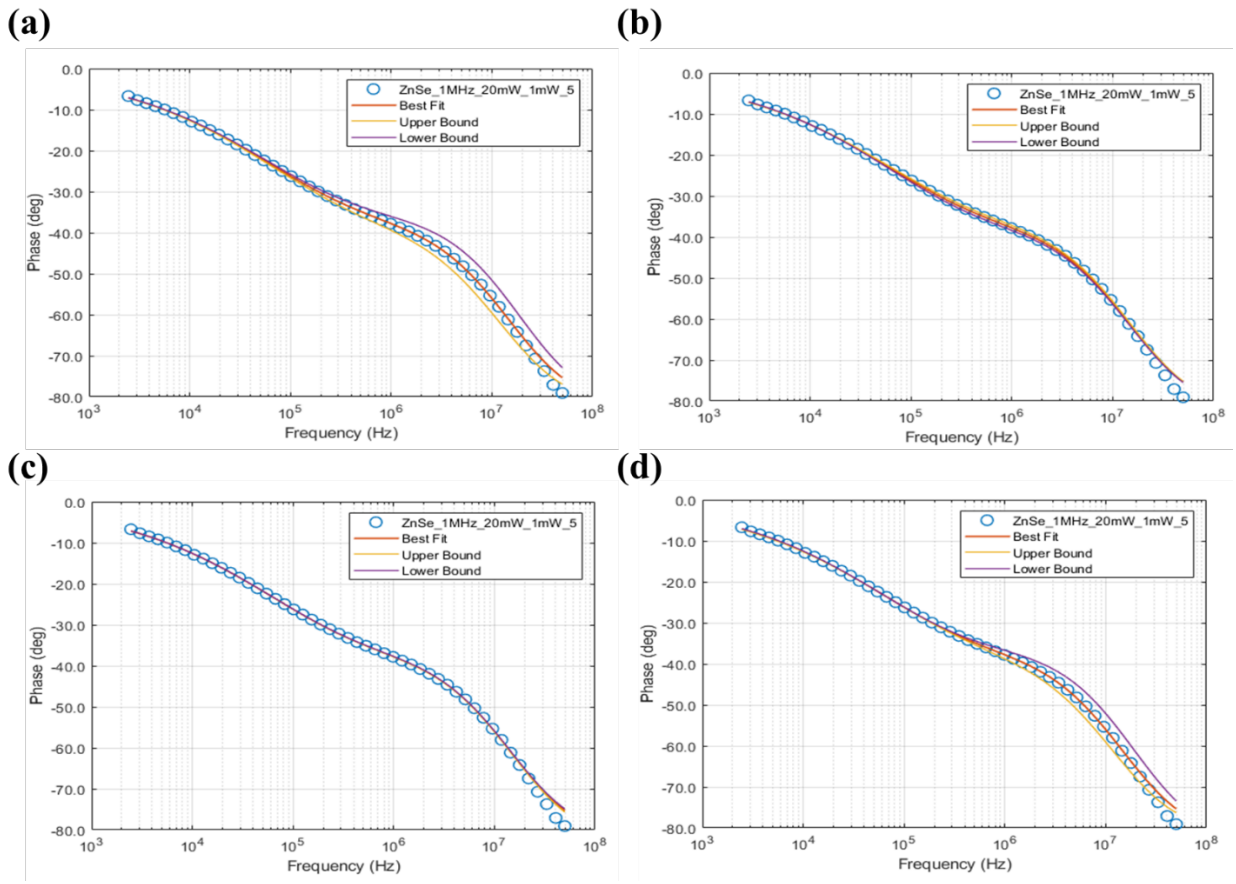

Figure 5.11: Sensitivity of phase-lag to a) gold volumetric heat capacity b) gold cross plane thermal conductivity c) gold in-plane thermal conductivity and d) thickness of gold film deposited on top of the ZnSe crystal

bound values of the phase lag measured in degrees (Figs. 5.11a, 5.11d), while insensitive parameters demonstrate small difference between these bounds (Figs. 5.11b, 5.11c). Figs. 5.11a, 5.11b and 5.11d show us that the measurement is sensitive to gold thin film's volumetric heat capacity, gold's cross-plane thermal conductivity and its thickness (essential input parameters). Figs. 5.12a and 5.12b, show that the measurement is sensitive to the cross and in-plane thermal conductivity of bulk polycrystalline ZnSe. Figs. 5.13a and 5.13b represent another way of understanding sensitivity in terms of the phase difference values.

As seen in Fig. 5.13, the sensitivity analysis shown in Figs. 5.11 and 5.12 can be represented as a function of the phase lag set to a certain upper and lower bound limit, which in this case

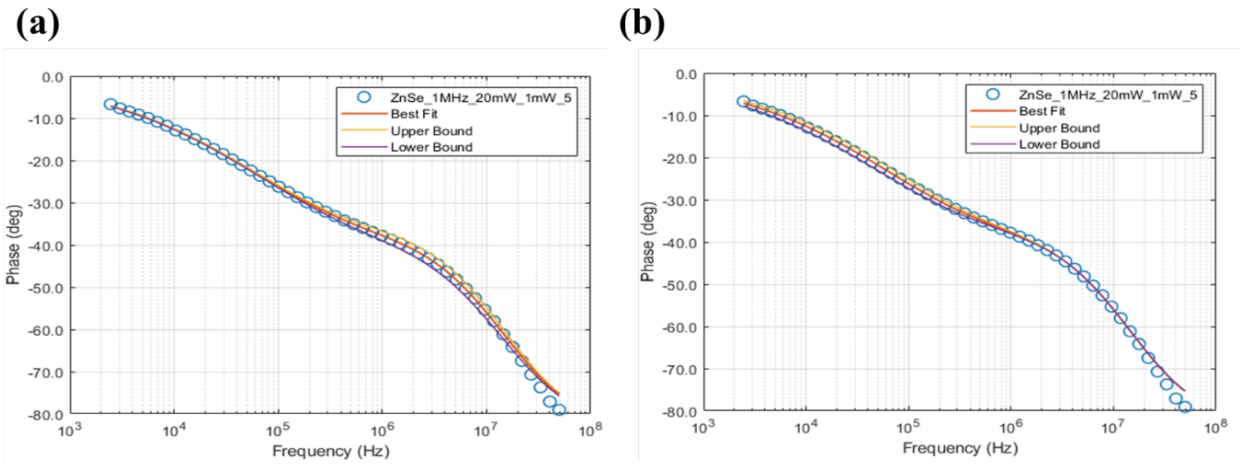

Figure 5.12: Sensitivity of a) Cross Plane b) In Plane thermal conductivity parameters of ZnSe Crystal

is set at 20%. This representation is a great way of determining the sensitivity of FDTR to the material parameters. Comparing the Figs. 5.11b and 5.11c with 5.13a, the orange and yellow curves represent the sensitivity of FDTR to the in-plane and cross plane thermal conductivity of gold thin film.

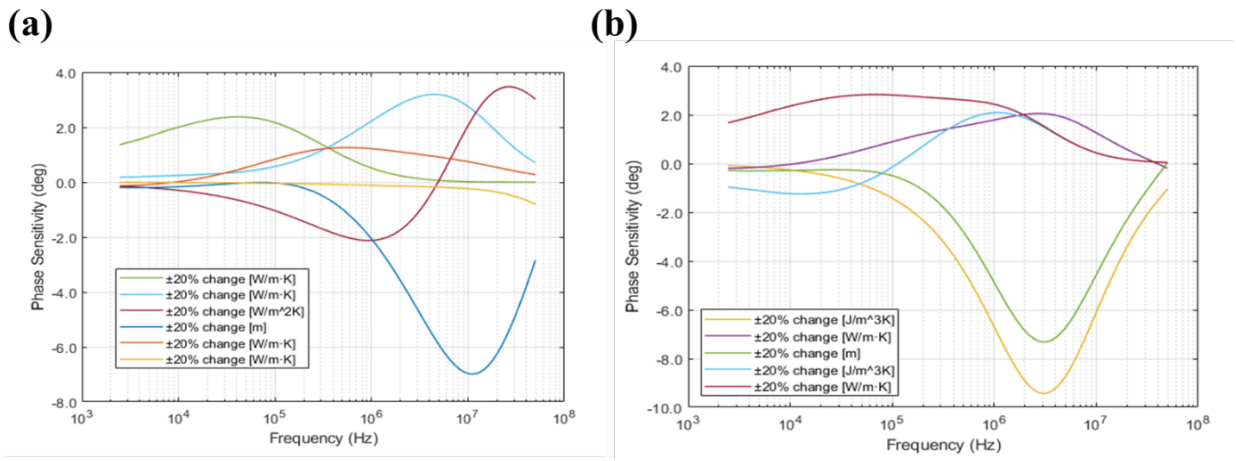

Figure 5.13: Sensitivity analysis of all the parameters of gold transducer and a) ZnSe and b) ZnTe as a function of phase change with limits of $\pm 20\%$ upper and lower bounds

The green and light blue curves in Figs. 5.13 corresponds to the FDTR's sensitivity to the in-plane and the cross plane thermal conductivity of ZnSe.

Analysis process similar to that of ZnSe was conducted for ZnTe as well in order to determine its thermal conductivity. Figs. 5.14 shows that with the help of accurately determined input parameters, we were able to achieve a good agreement between the FDTR's measurement of the

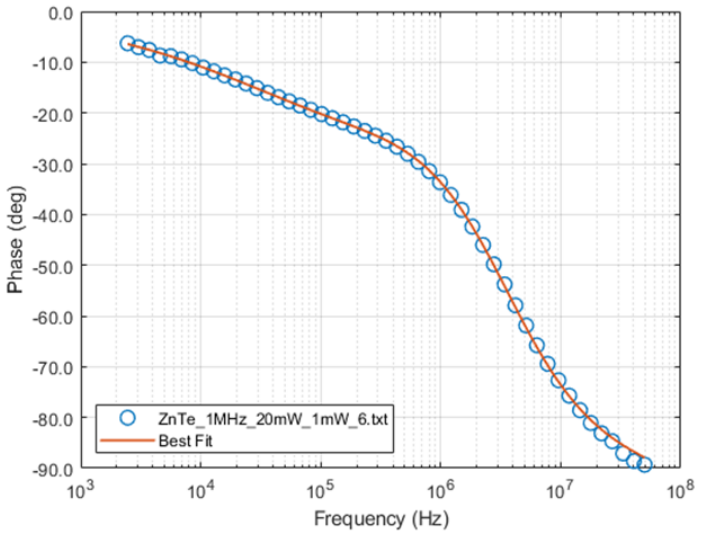

Figure 5.14: FDTR data for curve fitting analysis to calculate the thermal properties for ZnTe

phase lag and the phase lag calculated using the 2D diffusion model, keeping the thermal conductivity of ZnTe as a floating or a free parameter. This gives us a high confidence value of the thermal conductivity of ZnTe which was measured to be ∼14 W/m-K.

5.5 Conclusion

Using FDTR, the experimentally determined thermal conductivity values of ZnSe and ZnTe are found to be ∼17 W/m-K and 14 W/m-K respectively. These compare well to the computed results of around 23.2 W/m-K and 13.72 W/m-K for ZnSe and ZnTe respectively at 300K achieved using first-principles. The length dependent k value of ZnSe saw a significant reduction from 11.3 W/m-K to 1.75 W/m-K with the length scale going from 10 m to 10 nm whereas for ZnTe, the k value was observed to decrease significantly from 10 W/m-K to 1.2 W/m-K with similar length scale reduction as ZnSe. The difference in the experimental and the computational results can be attributed

to the dissimilarity in the polycrystallinity as obtained from the manufacturer and as modeled for computational analysis. This work is also a definite demonstration of the power of the tool that is FDTR, which can very precisely and accurately measure the thermal properties of materials. FDTR can also be utilized to measure the thermal properties of some unknown material systems with great confidence and supplemented by the computational work, one can easily gain a greater understanding towards the physics behind the heat transport phenomena taking place within the material system under study. Additionally, this combination of computational work and the experimental work using FDTR can greatly influence the ability of tuning the materials to achieve desired results for specific applications in the areas of thermal management and thermoelectric devices.

Chapter 6

Thickness Dependent Thermal Conductivity of Strontium Titanate (STO) Thin Films

6.1 Literature Review

Perovskite materials, of which strontium titanate (STO) and its thin films are an example, have attracted significant scientific interest, due to their desirable properties and the potential to tune thermal conductivity, by employing several techniques. Notably, strontium titanate thin films on silicon (Si) substrates serve as a fundamental platform for integrating various oxides onto Si substrates, making it crucial to understand the thermal properties of STO on Si.

The ability to control thermal conductivity is important for a wide range of applications. For instance, advancements in both oxide thermal barrier coatings and thermoelectric materials hinge on engineering a thermally resistive material that is optimized in conjunction with other parameters such as thermal expansion, microstructure, toughness, or carrier mobility. Similarly, materials with high thermal conductivity are desirable for thermal management applications. The remarkable ability of perovskites to accommodate a wide range of materials opens avenues to tune material properties through an appropriate choice of elements [111]. In recent years, epitaxial growth of complex oxides with the perovskite crystal structure has featured prominently in studies of the physics of correlated electrons [112] and in the search for electronic materials for information technology and sensing [113] [114]. Measurement of thermal conductivity of epitaxial thin films is another way to characterize the quality of epitaxial films, beside x-ray diffraction (XRD) [115], transmission electron microscopy (TEM) [116] [117], and in situ reflection high energy electron diffraction (RHEED) [118]. The perovskite family of oxides shows promise for thermal barrier [119] and thermoelectric applications [120, 121, 122, 123], because of its compositional tunability, which is accompanied by high-temperature stability. One such material from the perovskite

family is strontium titanate (Fig. 6.1) and its epitaxial thin films have attracted interest as possible insulating layers in dynamic random-access memories [124, 125, 126], ferroelectric thin film structures [127] and high-Tc superconductor devices [128, 129].

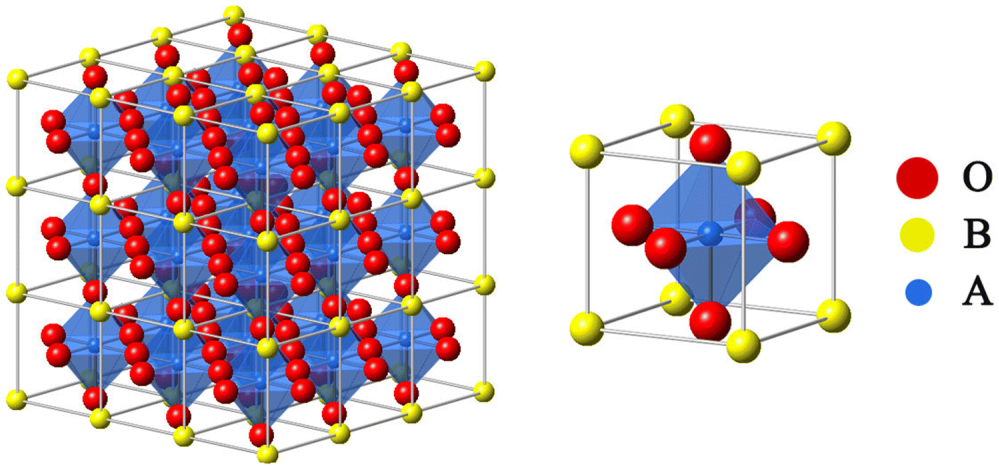

Figure 6.1: a) STO crystal structure and b) unit cell

Due to its potential applications, it is important to investigate thermal conductivity properties of STO and tunability of thermal conductivity using techniques such as varying domain size [130, 131, 132, 133, 134, 135, 136], defects, doping, deposition using different techniques under varying growth conditions and deposition of films on different substrates. Computational methods have also been applied to understand the thermal transport in STO.

With respect to thermal conductivity measurements for STO thin films, Oh *et al.* measured STO thin films produced using MBE and PLD (Pulsed Laser Deposition) techniques on single-crystalline STO and LSAT $(LaAlO_3)_{0.3}(Sr_2AlTaO_6)_{0.7}$ substrates [137]. The STO film thickness across all the samples was in the range of 300 to 400nm. The thermal conductivity of all the samples at 300 K ranged from $\sim$ 9 to 12 $Wm^{-1}K^{-1}$ for MBE samples while k values were in the range of $\sim$ 4 to 12 $Wm^{-1}K^{-1}$ for PLD samples [137]. Sarantopoulos *et al.* demonstrated that STO thin films grown on $DyScO_3$ substrate under tensile strain showed a significant reduction in thermal conductivity at room temperature to $\sim$2.5 $Wm^{-1}K^{-1}$, when compared to the STO on LSAT and STO substrates ($\sim$6 $Wm^{-1}K^{-1}$) [138]. Katsufuji *et al.* measured thermal conductivity of two

samples where one of them was a thin film of 70 nm $SrVO_3$ on STO and the other samples were thin film of 30 nm $SrVO_3$ and 30nm $SrTiO_3$ on LSAT substrates with thermal conductivities of 8 $Wm^{-1}K^{-1}$ and 2 $Wm^{-1}K^{-1}$ respectively [139]. Bugallo *et al.* measured $SrTiO_3$- $LaCoO_3$ superlattices on STO substrate, with varying periodicity of $SrTiO_3$ - $LaCoO_3$ and a total thickness of 80nm. The combinations of $SrTiO_3$ - $LaCoO_3$ were 40x2, 20x4, 10x8, 8x10, 5x16, 4x20 and 2x40 where the first number is the thickness of each layer and the other is the repetition of each layer. The thermal conductivity values for all the combinations were in the range of $\sim$ 4 to 1 $Wm^{-1}K^{-1}$ at 275 K [140].

Kumar *et al.* investigated the effect of Nb, and oxygen vacancies on thermal conductivity and thermoelectric properties of STO thin films. The lattice thermal conductivity at 300 K was measured to be 2.2 W/mK and the thermoelectric figure of merit was around 0.29 at 1000 K. The thin films were deposited on SiO_2/Si and LAO ($LaAlO_3$) substrates [141]. Yu *et al.* in their study mesured the thermal conductivity of oxygen deficient lanthanum-doped STO thin films $Sr_{1-x}La_xTiO_{3-\delta}$, deposited on STO/Si substrates, with the film thickness being $\sim$10 nm. The measured thermal conductivity of the thin film at 300 K was around 3 W/mK, which represents a large reduction in the value in comparison to bulk single crystal STO ($\sim$11 $Wm^{-1}K^{-1}$)[142]. Foley *et al.* looked at the thermal conductivity of nano grained STO thin films deposited on Sapphire substrates. Thin films with a thickness of 170 nm with varying grain sizes were deposited using a chemical deposition process. There was a reduction of 50%-60% across the grain sizes, as compared to the bulk values. A reduction in thermal conductivity with decreasing grain size was also observed in this work [143].

Brooks *et al.* demonstrated the ability to tune the thermal conductivity of homoepitaxial STO thin films using MBE by varying deposition parameters such as growth temperature, oxidation temperature and cation stoichiometry. The study showed a 80% reduction in thermal conductivity from 11.5 $Wm^{-1}K^{-1}$ for stoichiometric STO to 2 $Wm^{-1}K^{-1}$ by creating strontium rich homoepitaxial $Sr_{1+\delta}TiO_x$ films and also by introducing planar defects such as the $(SrO)_2$ Ruddlesden-Popper planar defects[111]. Breckenfeld *et al.* deposited $SrTiO_3$ thin films using PLD on $NdGaO_3$, where they illustrated that films with excess Sr displayed drastic reduction in thermal conductivity, as

compared to films with excess Ti [144]. Zhang *et al.* in their study of tunability of STO thermal conductivity, used annealing treatments as an effective method to induce reduction in the thermal conductivity values [145]. Wiedigen *et al.* induced defects (as a function of the deposition process), lattice strain (due to film-substrate lattice mismatch) and studied their effect on the film thermal conductivity in homoepitaxial STO films, produced by ion-beam sputtering [146].

Computational studies on the lattice thermal conductivity of $SrTiO_3$ were conducted by Fumega *et al.* using both *ab initio* Molecular Dynamic simulations and Density Functional Theory. This study focuses on the effect of structural distortions on the thermal conductivity of STO, by identifying key features of thermal transport in STO and the changes they undergo under a particular case of structural distortions. The thermal conductivity of bulk single crystal STO is measured to be 13.4 $Wm^{-1}K^{-1}$ [147]. Martelli *et al.* conducted studies on the thermal conductivity of doped and undoped STO, over a temperature range of 2 to 400 K and identified different heat flow regimes. In one of the regimes for undoped STO the thermal conductivity increased faster than T^3, at low temperatures, an effect that was attributed to hydrodynamic phonon transport. Such an effect was lost with the introduction of any dopant[148].

Data on thermal conductivity of STO thin films on Si substrate is lacking. STO on Si substrate serves as an epitaxial platform upon which other multifunctional oxides can be integrated for various device applications [149]. Understanding thermal transport of this material system is important to such applications [150]. In this study, we examine the thermal conductivity of four STO thin films of thicknesses of 12 nm, 50 nm, 80 nm, and 200 nm deposited on Si substrates.

6.2 Sample Preparation

The STO thin films were epitaxially grown on 2" diameter, undoped Si (100) wafers (Virginia Semiconductor) using oxide molecular beam epitaxy (MBE). Epitaxial growth was initiated through the crystallization of 2 unit-cells of amorphous STO deposited at room temperature, as discussed in detail elsewhere [151]. After crystallization of this seed-layer at $\sim$ 500 ^{o}C in ultra-high vacuum,

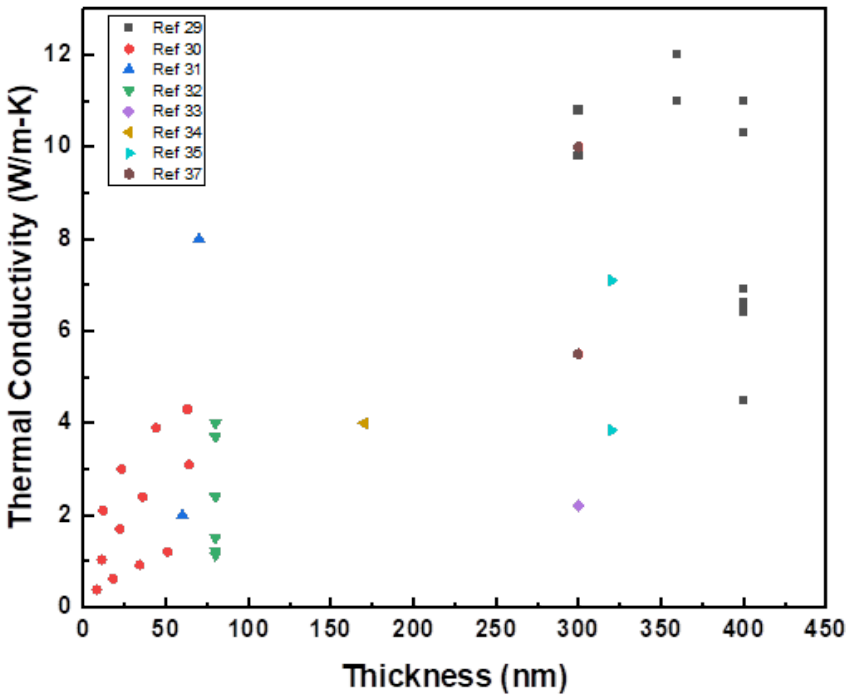

Figure 6.2: Plot showing the values of thermal conductivity of STO based thin films for various growth conditions and substrates

subsequent layers were grown through co-deposition of SrO and TiO_2 fluxes on Si wafers held at a temperature of 580 ^{o}C in a background pressure of 3 $\times$ 10^{-7} Torr of O_2. After growth, each wafer was diced (Disco DAD3220) into smaller pieces measuring 6 $\times$ 4 mm^2 for thermal conductivity measurements.

Additionally, the Au thin film converts the energy from the laser to create a periodic heat source at the sample's surface. The periodicity of the heat source corresponds to the frequency at which the pump laser beam is modulated. The Au film is deposited using a pellet (99% purity) as a target, for the deposition[46, 107, 36] purchased from Kurt. J Lesker Company. We use Lesker Nano36 Evaporator thermal evaporator, (part of Microfabrication Research & Education Center at University of Oklahoma) to deposit $\sim$100nm of gold film, which is a target thickness set in the thermal evaporator machine as a process parameter. The final gold film thickness achieved will be different, as it is based on the position of the sample placed on the sample holder. Before the start of the gold film deposition process, the STO samples were mounted on the sample stage in the

thermal evaporator, where a piece of sapphire reference sample was placed in between 200 and 50 nm STO samples, and another in between 80 and 12 nm STO samples respectively.

6.3 Structural Characterization of STO Thin Films

X-ray diffraction (XRD) (Fig. 6.3) confirms the epitaxial quality of the STO thin films on Si. The XRD measurements were taken on a Bruker D-8 system that is equipped with a standard Cu kα x-ray source ($\lambda = 1.54056$ Å). Figure 3 shows survey scans of the 4 films with the various diffraction peaks labelled. The out-of-plane lattice constants of the 12 nm, 50 nm, 80 nm, and 200 nm films were 3.918 Å, 3.924 Å, 3.898 Å, and 3.910 Å, respectively, which largely compares well with the bulk lattice constant of STO (3.905 Å).

6.4 Experimental Details

Thermal conductivity measurements were performed using the frequency domain thermo-reflectance method (FDTR). A sinusoidally modulated pump laser (wavelength $\lambda = 473$ nm) with a power of 51.41 mW was used to create a periodic heat source at the sample surface. The frequency range for the modulation of the pump laser is from 2000 Hz to 50 MHz. A probe laser ($\lambda = 532$ nm) was used to measure the change in phase of the temperature response of the surface with respect to the phase of the input heat signal. This is achieved by measuring the surface temperature through a measurement of the reflected probe beam's intensity which is dependent on the surface temperature of gold transducer layer through a thermoreflectance coefficient. The measured phase lag is fitted to an analytical 2D heat conduction model, by varying parameters such as material thermal conductivity.

The values of the parameters corresponding to best fit yield the material properties. The four STO samples of varying thicknesses (200nm, 80nm, 50nm, 12nm) were coated with $\sim$130 nm of gold film, which acts as a transducer layer, absorbing heat from the pump beam, and conducting

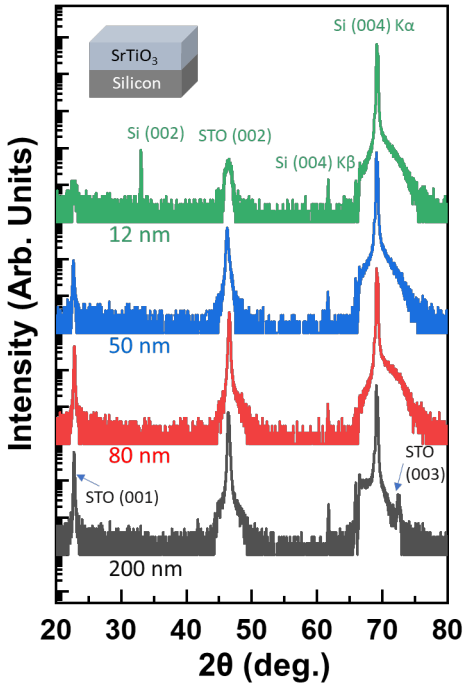

Figure 6.3: X-ray diffraction of the four SrTiO3 films showing epitaxial growth on silicon. Various diffraction peaks are labeled

the heat into the sample. With the gold coating, these materials become a 3-layer stacking problem, which can be visualized in Fig. 6.4.

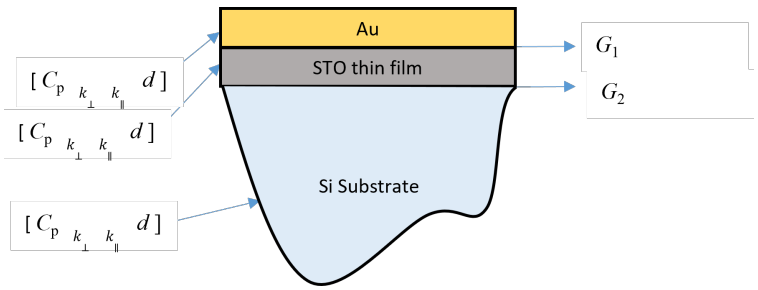

Figure 6.4: Multilayer stack model for Strontium Titanate (STO) thin film on Si Substrate

Each layer, starting from the top layer of gold to the Si substrate, is characterized by volumetric heat capacity (C_p), cross-plane thermal conductivity($k_\perp$) , in-plane thermal conductivity ($k_\parallel$), and thickness. Thermal boundary conductance (TBC) of Au/STO thin film interface (G_1) and STO thin film/Si substrate interface (G_2), are also shown in the figure. For a n layer system, the number

of properties associated with the system are $5n$-1 resulting in 14 parameters for a 3-layer material system. By eliminating the parameters with known values (such as silicon thermal conductivity), the number of unknown parameters to be obtained by the fitting process between measured and computed phase lag are reduced. Another important parameter for the fitting analysis is the laser spot size. The laser spot size determines the size of the heat source on the sample surface, which is an important parameter used in the calculation of the phase lag using the 2D heat conduction model. The estimate of these parameters is described next.

6.5 Thermal Conductivity Measurement

6.5.1 Evaluating Input Parameter Quantities

The thermal conductivity, thickness and CTR (coefficient of thermoreflectance) values for Au layer deposited on the STO samples are determined by performing transducer layer characterization using a reference sample, with known thermal properties such as fused silica or sapphire [152]. By fitting the thermal properties of the transducer layer on reference samples, we use these values as input parameters for the analysis of the STO samples. Such transference of properties of gold layer from reference sample to STO samples is possible because of the assumption in the analysis methodology that the values of the properties of the Au layer, for samples placed very close to each other will be the same. The properties of the sapphire reference sample, chosen for the transducer layer characterization analysis, are pre-determined in the analysis software. The C_p and cross-plane k values for the reference sample used in this process are 3.066 $MJm^{-3}K^{-1}$ and 36.43 $Wm^{-1}K^{-1}$ respectively. Since the reference sample is a c axis sapphire, we use anisotropy ($\frac{k_{\parallel}}{k_{\perp}}$) value to be 0.85.

Based on this, Table.6.1 compiles the results for the Au layer properties for reference sapphire samples, used in the analysis of the STO samples. The value of C_p (also pre-determined in the fitting analysis software) for gold is 2.484 $MJm^{-3}K^{-1}$[153].

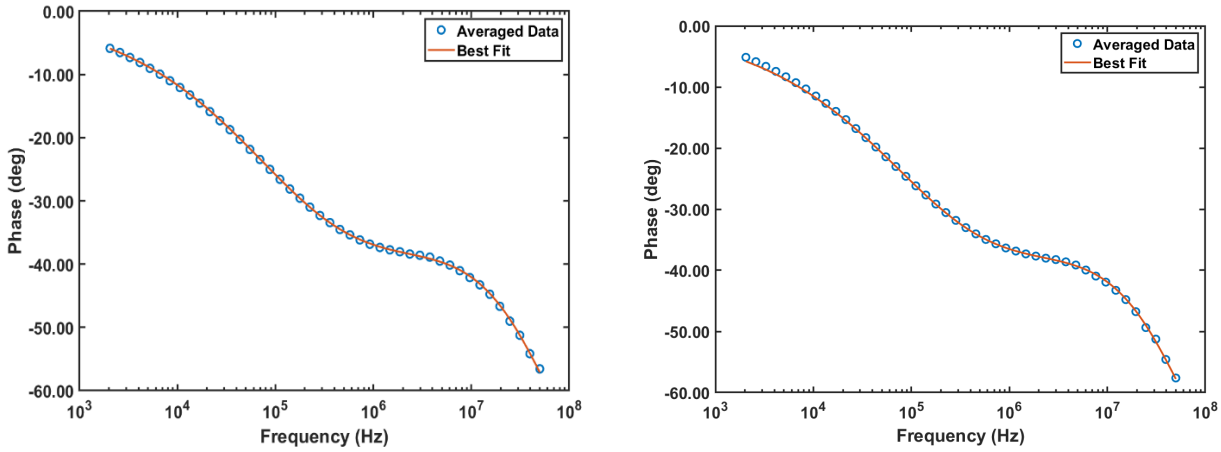

(a) (b)

Figure 6.5: Curve fit analysis for transducer (Au thin film) on Sapphire reference samples for a) 200 and 50 nm STO samples b) 80 and 12 nm STO samples, determining the thermal conductivity and thickness properties of Au thin film on the STO samples (used as input parameters for STO analysis)

Figs. 6.5a and 6.5b are the best curve fit figures for the transducer layer analysis of reference sapphire samples for 200 and 50 nm STO samples, and 80 and 12 nm STO samples respectively. Since the 200 and 500 nm samples share the same sapphire reference sample, the reference sample curve fit analysis is represented by the same figure for both the samples. This is also true for the 80 and 12 nm STO samples. We observe that the best curve fit line for the measured data fits near perfectly for both the measurements. This indicates the fitted values of the thermal conductivity and the thickness for the transducer layer, determined during this analysis is the correct solution. The Table. 6.1 is the properties of the Au thin film, which are used in the analysis of the STO samples.

The $SrTiO_3$ thickness is measured as a function of the deposition rate, which is computed from the rates of SrO and TiO_2 fluxes, which are measured and controlled during the STO thin film deposition process. Volumetric heat capacity values for Au and Si layers are taken from the literature.

Table 6.1: Au thin film transducer layer characterization using properties of the STO reference sample.

STO Thin Film Thickness *(nm)*	k **(thermal conductivity)** $(W m^{-1} K^{-1})$	**Au Film Thickness** t *(nm)*
200 nm	196 ± 25.48	137 ± 9.59
80 nm	196 ± 25.48	138 ± 9.66
50 nm	196 ± 25.48	137 ± 9.59
12 nm	196 ± 25.48	138 ± 9.66

$$C_p = a + bT + \frac{c}{T^2} + \frac{d}{\sqrt{T}}(1) \tag{6.1}$$

The volumetric heat capacity ($Jmol^{-1}K^{-1}$) for STO is calculated using the above formula mentioned in the literature [154] [155], where the values of a, b, c, and d, are 134.581 $Jmol^{-1}K^{-1}$, 0.0045567 $Jmol^{-1}K^{-2}$, 11.979e^5 $Jmol^{-1}K$, and -414 $Jmol^{-1}K^{-1/2}$ respectively. Using a molecular weight of 189.49 $gmol^{-1}$ and a density of 4.81 gcm^{-3} for strontium titanate, the volumetric heat capacity is obtained to be 2.77 $MJm^{-3}K^{-1}$. Experimentally, the volumetric heat capacity of STO was determined to be around 2.78 $MJm^{-3}K^{-1}$ [156].

6.6 Best Curve Fit Analysis

6.6.1 Quantifying Thermal Conductivity of Films

In Figs. 6.6, the slope of the phase lag plot and its best fit curve in the mid to high-frequency range changes from a trough to a slight crest as the sample thickness decreases (indicated in Fig. 6 using red highlighted box). This discernible difference in the phase lag plots indicates that all the samples with varying thickness exhibit discrete trends.

In Figs. 6.7a, 6.7b, 6.7c, 6.7d, shows the sensitivity of the parameters across the modulation

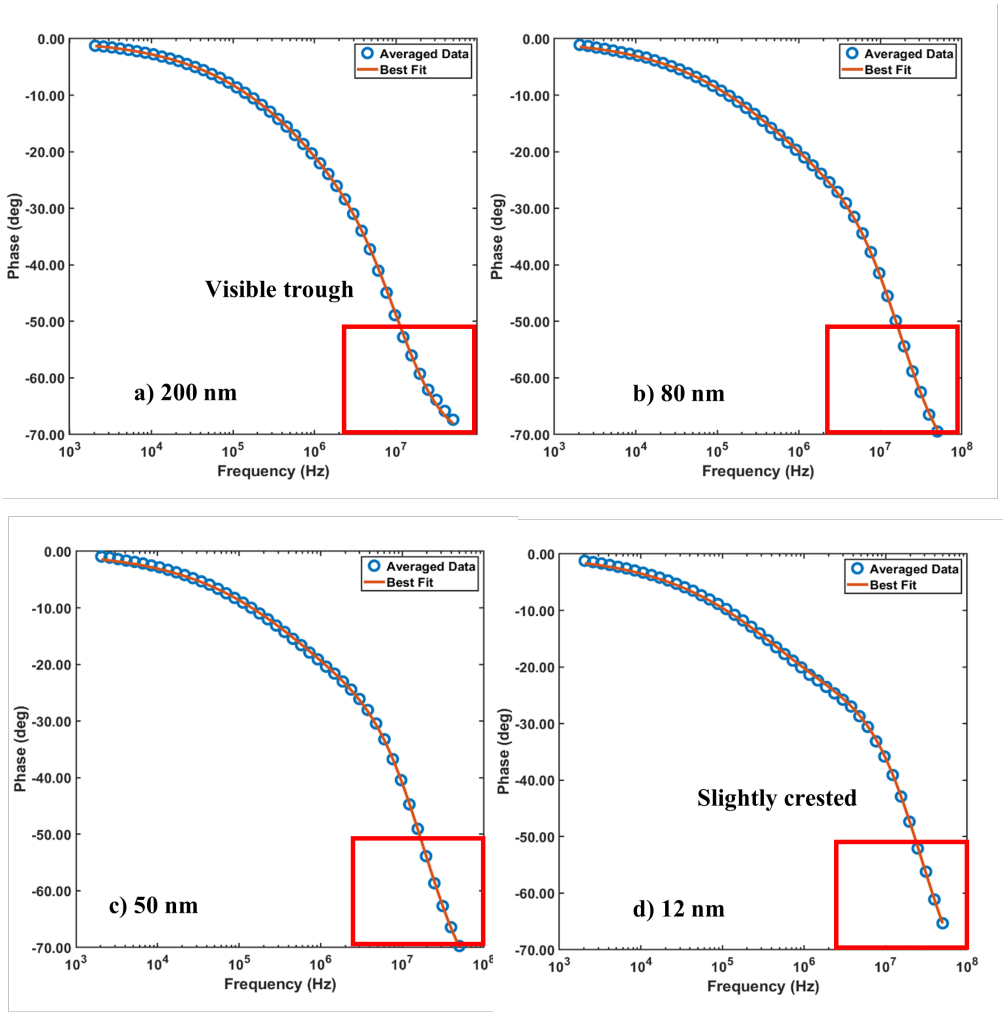

Figure 6.6: Curve fitting analysis for STO thin films of varying thickness a) 200 nm b) 80 nm c) 50 nm d) 12 nm, determining the thermal properties of the STO films under examination

frequency range. The measurement is found to be sensitive to cross-plane thermal conductivity (TC), with the extent of sensitivity remaining relatively constant in all the cases. This is an indication that the values of cross-plane conductivity obtained by the curve fitting analysis will be accurate. We also observe that the solution is relatively insensitive to the thermal boundary conductance (TBC) $G_1$and G_2 in all the cases. Therefore, we assign a high value to G_1 and G_2 equal to 1000 $MWm^{-2}K^{-1}$ and consider them to be fixed input parameters with a known value, for our analysis. This clears up the fact that there is little to no resistance to heat flow across these thermal boundaries and the effective resistance to the heat flow comes predominantly from the material's

thermal conductivity.

In this analysis we also consider the anisotropy ($\frac{k_\parallel}{k_\perp}$) as 1, implying that the materials are isotropic. Under this imposed isotropic condition, the analysis software outputs the thermal conductivity value (either the cross-plane or in-plane) based on the measurement's sensitivity to the specific parameter. In our case, the system is sensitive to the cross-plane thermal conductivity of the STO thin films and is insensitive to the in-plane thermal conductivity. Hence, by keeping the anisotropy to be 1 (essentially not decoupling the cross and the in-plane thermal conductivities), we reduce another fitting parameter, aiding us in the fitting analysis.

This leaves us with only 2 unknown parameters, namely, STO cross-plane thermal conductivity and laser spot size. The reason we fit the spot size along with the thermal conductivity for our analysis is because the main source of experimental uncertainty comes from the estimation of spot size [157] [7].

This spot size can be determined in two ways, by using a knife edge method with a x-y piezo stage and by using Gaussian beam optics with a stationary sample stage. The knife edge method is an expensive method of determining spot size, as it requires a specially prepared knife-edge sample, a piezo stage and additional photodetectors, attached to the stage [41].

One can reduce the expense of this spot size measurement, with a stationary stage, which would be less accurate. In this method, the pump laser spot is scanned over the probe layer spot, generating a Gaussian spot intensity profile, which is fitted to a calculated Gaussian spot intensity profile. This is done in both x and y directions. The curve fit analysis of these intensity plots provides us with a reasonable estimation of the spot size, at the cost of increased uncertainty.

Hence, for our analysis, a 2-parameter fit was essential to perform thermal conductivity measurements accurately. Thin films can generally show anisotropic nature due to their very small thickness, but when we analyze the sensitivity plots, we see that there is no sensitivity to the in-plane thermal conductivity property in any of the samples. This is because the substrate in use is Si ($C_p = 1.64$ MJm^{-3}K^{-1}, used in the fitting of STO measurements), which has a very high thermal conductivity value of $\sim$145 Wm^{-1}K^{-1} (also used in the fitting analysis). This leads to quick dissi-

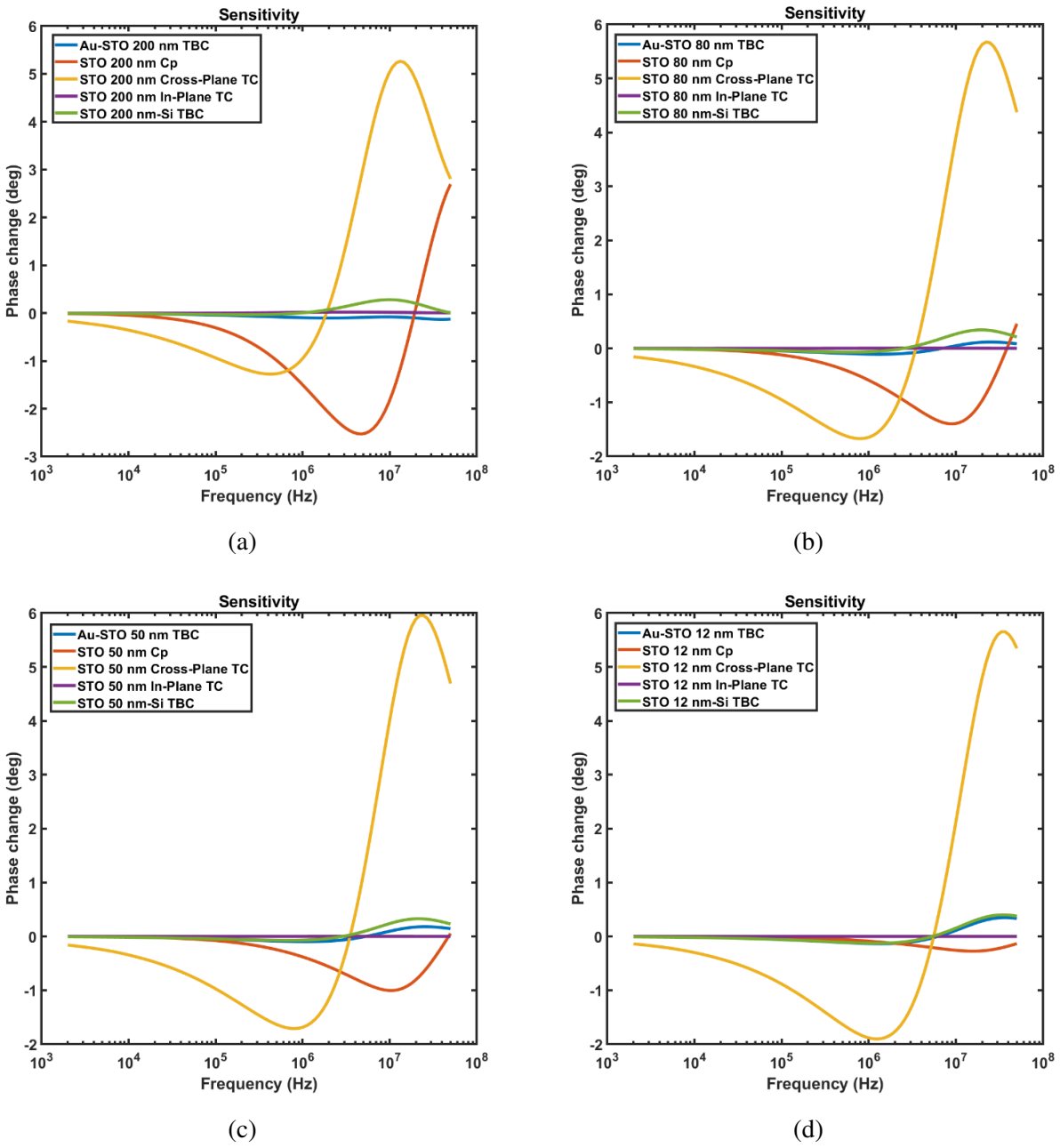

Figure 6.7: Sensitivity plots for different parameters for STO thin films of varying thickness a) 200nm b) 80nm c) 50nm d) 12nm, indicating the extent to which each parameter is sensitive to the measurement done at each thickness. Sensitivity of every parameter is measured across the modulation frequency range

pation of the heat into the Si substrate, diminishing the spreading of the heat in the radial direction, leading to insensitivity to the in-plane thermal conductivity. We then perform a 2-parameter fit for

the cross-plane thermal conductivity of STO and laser spot size, to find the best fit solution for the material systems with varying thickness. The values of STO thermal conductivity for different thicknesses are tabulated in 6.2.

The value of thermal conductivity for STO thin film decreases with the decreasing thickness of the thin film. The reduction in the thermal conductivity across various thicknesses ranges from $\sim 38\%$ to 93%, when compared to the value of bulk single crystal of STO, purchased from MTI Corporation [86]. The thermal conductivity of bulk single crystal was also measured in our FDTR system, with a value of 12.5 $Wm^{-1}K^{-1}$. The approach for its analysis was like the one used in the case of thin films. These k values have an uncertainty of 10%, 11%, 11% and 13% respectively, from the thickest to the thinnest film.

The 38% reduction in thermal conductivity value of 200 nm thin film relative to bulk sample is due to both finite-size effects associated with scattering of phonons at boundaries of the STO sample as well as due to presence of dislocations in the sample. Epitaxial films of STO on Si have dislocations due to the mismatch of not just the in-plane but also out-of-plane lattice constants between STO and Si. Steps on the Si surface associated with the miscut in the wafer are incommensurate in height relative to the lattice constant of STO.

Consequently, even very thin films, such as the 12 nm thick film studied here, have dislocations that give rise to anti-phase boundaries in the STO [158]. At present, the effect of such dislocations on thermal conductivity is not well established. We estimate the distance between dislocations to be ~ 25 nm in our films [159]. The even larger 93% decrease in the thermal conductivity value of the 12 nm thick film relative to the bulk sample, points to reduction in part from finite-size effects, as the density of dislocations due to steps on the Si surface in the 12 nm thick film and the 200 nm thick film are comparable.

Table 6.2: Thickness-dependent thermal conductivity of STO thin films on Si.

STO Thin Film Thickness (nm)	**Thermal Conductivity k ($\mathbf{W\,m^{-1}K^{-1}}$)**
200	7.4 ± 0.74
80	3.86 ± 0.43
50	2.35 ± 0.26
12	0.80 ± 0.10

6.6.2 Volumetric Heat Capacity Estimation

Figs. 6.7a, 6.7b, 6.7c and 6.7d show a steady reduction in measurement's sensitivity to the volumetric heat capacity (C_p) of STO, with decreasing thickness. To measure C_p, we need to apply a 3-parameter curve fit analysis, with parameters being fitted as C_p, k, and thickness. Table. 6.3 shows that the value of C_p is most certain for the 200 nm thick sample. Although the value of uncertainty increases with the decreasing thickness of the films, the C_p values seem to be relatively in the range of the literature values. The uncertainty values are associated to the parameter's sensitivity across the film thicknesses, as seen in Fig. 6.7. Therefore, to accurately measure the volumetric heat capacity and to be confident in the value derived from analysis using FDTR, the film needs to be thick enough for it to be sensitive to C_p. The measured C_p values for the thickest film is 3.07 $MJm^{-3}K^{-1}$ with an uncertainty of 6%. The reason why the 3-parameter fit worked in this case is that phase lag sensitivities of cross-plane thermal conductivity and C_p shows us that they traverse a completely different trend, across the range of modulation frequencies of pump laser (2000 Hz – 50 MHz), and the fact that there is a sensitivity difference between the two parameters at the lowest frequency.

Fig. 6.8 depicts the Monte-Carlo simulations for the curve fit analysis, that involves chosing random values of the fixed input parameters based on their Gaussian distribution and then confirming the response of the fitted parameters, which should also have a Gaussian response. This normal distribution of the fitted parameters to a small peak value is another way of validating our

Table 6.3: Volumetric heat capacity for STO at different thicknesses with uncertainties.

STO Thin Film Thickness *(nm)*	**Volumetric Heat Capacity** C_p $(10^6\ Jm^{-3}K^{-1})$	**Uncertainty** *(%)*
200	3.07	6
80	2.79	21
50	2.71	35
12	2.64	51

experimental results, proving them to be correct and true. The results of the fitted parameters is considered to be incorrect, in case we observe a distribution other than the Gaussian distributuion.

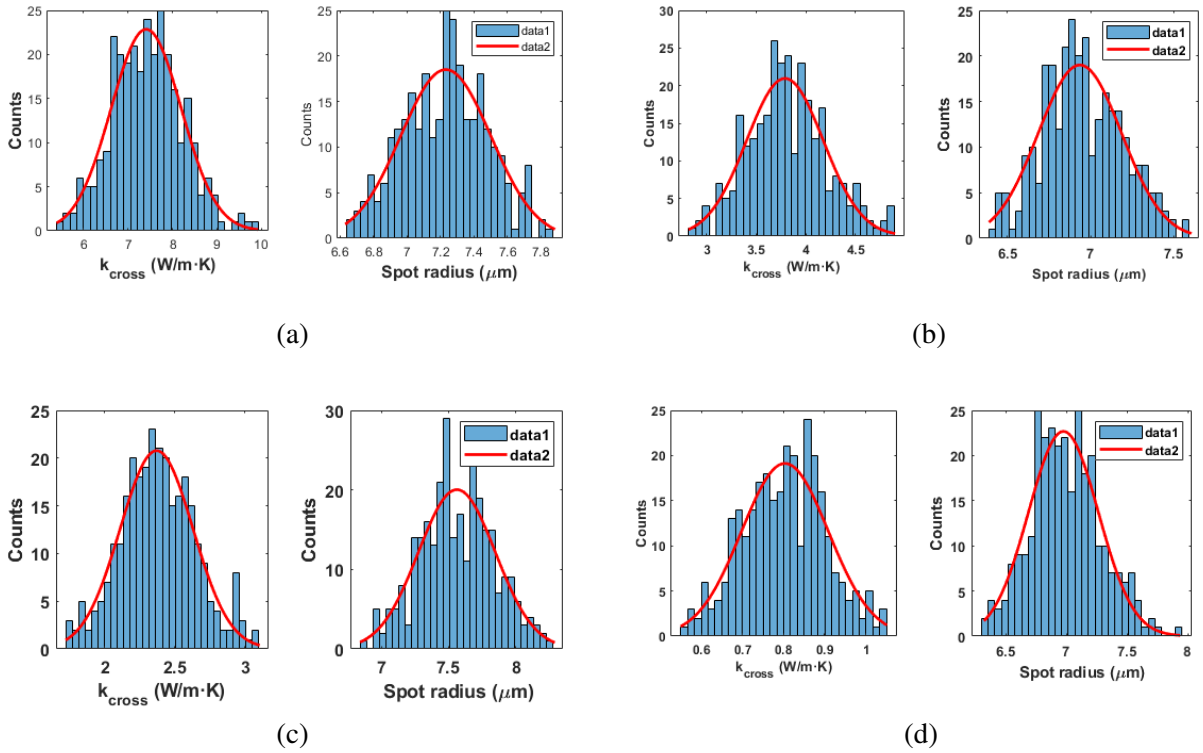

Figure 6.8: Monte Carlo simulation results for a) 200 nm b) 80 nm c) 50 nm d) 12 nm showing the distribution of the results obtained for the fitted parameters

6.7 Conclusions

In summary, we measured the thermal properties of STO thin films on Si substrate for four different thicknesses of STO films, 200nm, 80 nm, 50 nm and 12nm as well as a bulk STO sample. The thermal conductivity values were measured to be 7.4, 3.86, 2.35 and 0.8 W $m^{-1}K^{-1}$ for the 200 nm, 80 nm, 50 nm and 12 nm, respectively. The k value for the bulk STO sample was measured to be at 12.5 $Wm^{-1}K^{-1}$. A significant reduction of 93% in the thermal conductivity value was observed for 12 nm thin film, in comparison to the value of bulk single crystal STO. The percentage reduction in k values of different thickness thin films indicate the approximate mean free path of phonons. A 38% reduction in thermal conductivity for the 200 nm thick sample, relative to bulk value, indicates that phonons with mean free path larger than 200 nm, contribute $\sim$38% to overall thermal conductivity. The measurements were sensitive to the cross-plane thermal conductivity of the thin films and volumetric heat capacity (C_p) but were insensitive to other parameters such as the in-plane thermal conductivity and thermal boundary conductance. The measured values of C_p of the thin films were in reasonable agreement with the literature values. A co-relation between uncertainty of C_p values across the samples and the measurement's sensitivity to the parameter was found. Sample's decreasing thickness leads to decreased sensitivity to C_p, which is responsible for the increasing uncertainty, with it being the highest for the thinnest sample. The work provides understanding of thickness dependence of thermal conductivity of STO on Si substrate.

Chapter 7

Characterizing the Thermal Conductivity of Silicides of Rhenium using First Principles

7.1 Introduction to Transition Metals and their Structures

For the applications such as the optoelectronic [160, 161] and thermoelectric devices [162], materials such as transition metal silcides have garnered the attention of the scientific community [163]. Thermoelectric devices have also gained attention for their potential applications in the areas of power generation and refrigeration [164]. These materials have been shown to contain cage like structures, where the rattling of the atoms causes the phonon to scatter, lowering the thermal conductivity while the electronic conductivity remains unchanged or in some case is found to be enhanced. These kinds of materials are classified as phonon glass-electron crystal [165, 166]. In this family of transition metal disilicides, one material system that is being touted to have the potential to transform these devices is Rhenium Disilicide [163].

Rhenium disilicide's semiconducting nature having a narrow band gap [167] was fist discovered by Nesphor [168] which then gave rise to numerous other investigations [169, 170, 171] on its nature. Gu et al. [172] provided insights on the demonstration of material's exceptional thermoelectric properties by report a figure of merit (ZT) value of 0.7 at 1000K. This was achieved by synthesizing a single crystal of its compound, whose crystallographic direction was chosen specifically to observe its performance. Long [173] and Gottlieb [171] reported that the direct and indirect band gaps of 0.36 eV and 0.12 eV for the disilicide thin films through optical measurements and two band gaps of 0.16 eV and 0.30 eV through electrical resistivity measurements on a single crystal respectively. Interestingly, these results disproved that this material system is metallic in nature, which was theorized through computational analysis [174, 175].

The story of crysrtal structure characterization of Rhenium Disilicide is an interesting one.

Firstly it was attributed to have a body-centered tetragonal C11b structure, which is similar to $MoSi_2$ type structure with a I4/mmm space group. The lattice parameter were determined to be a = 0.3121 nm and c = 0.7681 nm [168]. Then later studies revealed that there were still some discrepancies in the understanding of material's crystal structure and its stoichiometry. A composition of $ReSi_{1.8}$ with constitutional vacancies on Si sites [169] was reported through this investigation. A subsequent study by Siegrist et al. [170] found that the structure is a body-centered orthorombic (space group Immm) with a composition similar to $ReSi_2$. Gottlieb et al. report that the compound's structure is triclinic (space group P1) and its stoichiometry is $ReSi_{1.75}$ [171]. They conclude that half of the Si sites in the unit cell is randomly occupied by the constitutional voids. However, electron diffraction patterns that were taken from a specific crystallographic directions exhibited extra spots that indicated a long-range ordered structure [176, 172] and those of Mishra et al. [177]. A new structure for the material was determined to be a monoclinic structure (space group Cm) with lattice parameters a=2.32nm, b=0.314nm, c=0.831nm and β=92.8º, and the atomic positions were assessed by the first principle calculations [163]. The crystal structures for ReGaSi, ReAlSi and ReSi have been shown in Figs. 7.1 [178] and 7.2 [179].

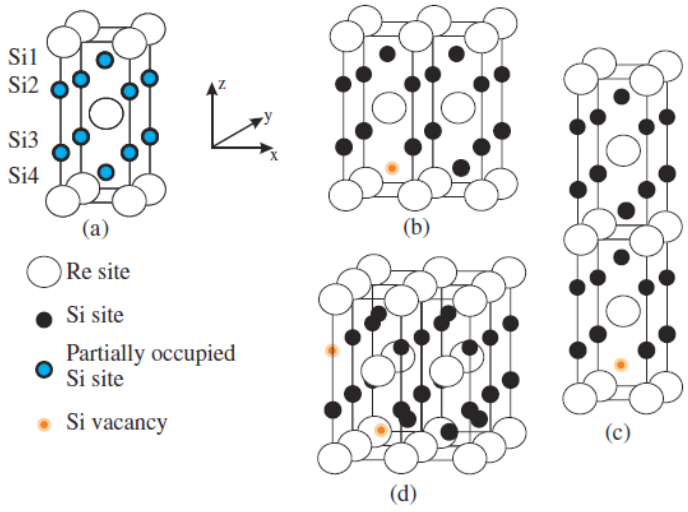

Figure 7.1: Crystal structure of ReSi

ReAlSi and ReGaSi are ternary compounds that have been developed from the $ReSi_{1.75}$ com-

pound family. The compostion of ReAlSi and ReGaSi is in the ratio of 1:1:1, satisfying the (18 – 4) valence electrons per formula unit (f.u.) rule, where need for vacancies is eliminated, and therefore both ReAlSi and ReGaSi are presumed to have a crystal structure, that is similar to that of $MoSi_2$. While the $MoSi_2$ is a body-centered structure, the ReAlSi and ReGaSi are found to be primitive structure. This slight difference in the two material systems arises due to the restructuring of the Al and Si atom just like they way it was observed between the Ga and Si atoms in the ReGaSi structure [180]. Investigation on the crystal structre for the ternary compounds tells us that the they have a tetragonal common space group of P 4/mmm. The lattice parameters for ReGaSi and ReAlSi are a=3.19 Å, b=3.19 Å c=8.054 Å and a=3.17 Å b=3.17 Å and c=8.04 Å respectively. All the angles of the for the compounds were found to be 90 degrees [179].

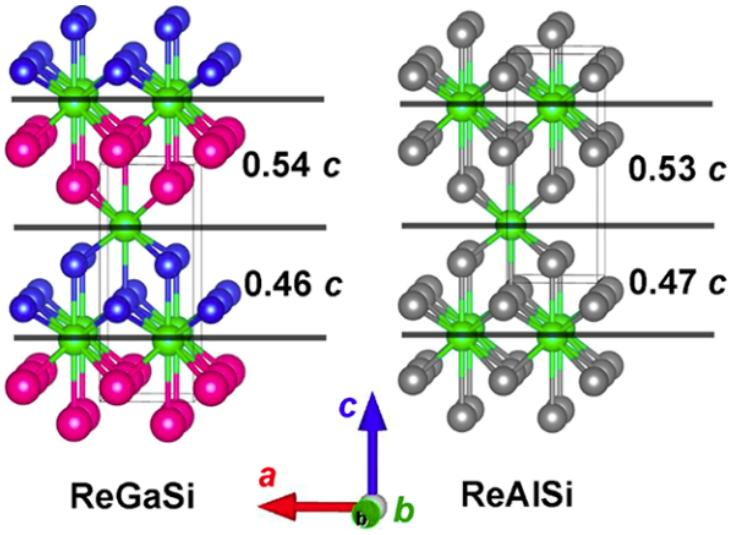

Figure 7.2: Crystal structures of ReGaSi and ReAlSi

These structures have been conceptualized and analyzed theoretically, and have also been been synthesized experimentally [181].

7.2 Computational Details

For the self-consistent calculations in ReAlSi and ReGaSi, we used a plane-wave based Quantum ESPRESSO [59] package, conducting the electronic calculations using local density approximation and norm-conserving pseudopotentials. For ReAlSi and ReGaSi, we used a plane-wave energy cut-off of 80 Ry, with a Monkhorst-Pack k-point mesh of 5 x 5 x 2 and 10 x 10 x 4 for the two calculations, and for ReSi, the plane-wave energy cut-off of 40 Ry, with a Monkhorst-Pack grid of 1 x 7 x 3 for integration over the Brillouin Zone. The crystal structure was relaxed until the toal force acting on each atom diminished below $1e^{-10}$ eV/Å.

The optimized lattice parameters for ReAlSi, ReGaSi and ReSi were a=3.15 Å c=7.96 Å, a=3.15 Å c=7.87 Å, and a=23.09 Å b=3.13 Å c=8.36 Å respectively. The harmonic (2^{nd}) order force constants in real space were computed on the supercell as the Monkhorst-Pack[58] grid for all the materials. For ReAlSi and ReGaSi, the anharmonic (3_{rd}) order force cosntant were computed on a 5 x 5 x 2 q-point grid, and inverse Fourier transform was applied to obtain force constants in real space using the D3Q[101, 102, 103] package in Quantum ESPRESSO. Thermal conductivity was calculated on a 20 x 20 x 8 q-point mesh, using the thermal2[101, 102, 103] code in Quantum ESPRESSO.

For ReAlSi and ReSi calculations in ShengBTE [182], the (2^{nd}) order force constants were computed by converting the harmonic force constants from QuantumESPRESSO to a Phonopy converter. The converter utilized a python script in Phonopy, where the input parameters were the second order force constants file from Quantum ESPRESSO and a supercell input file. The conversion was excuted by running the command as instructed in the Phonopy environment. The anharmonic (3_{rd}) order force constants were computed on 5 x 5 x 2 supercell for ReAlSi and 1 x 2 x 2 for the ReSi thermal conductivity measurement. For ReAlSi, we chose the displacement files to be generated for 10 nearest neighboring atoms. For ReSi, we checked the convergence of the thermal conductivity values calculated using the third order force constants derived from 10 and 12

nearest neighboring atoms and then finally used the 1 x 2 x 2 supercell with 10 nearest neighboring atoms for the calculation of the force constants. The set of q-grid points that were utilized for the thermal conductivity calculations was 3 x 21 x 9 at 1.0 scale broad value. For the finer grid sizes of 4 x 28 x 12 and 5 x 35 x 15, we used a scale broad value of 0.1 as we saw that the thermal conductivity values converged across the various scale broad values.

7.3 Computed Thermal Conductivity Values

Here we will first discuss about the thermal conductivity values of ReAlSi and ReGaSi under various conditions. We measure the length dependent thermal conductivity of both the materials by changing the characteristic length of the crystal structure, which determines the length of the physical boundary of the material system in all the three directions. We see that the values of k_x and k_y remains the same, but thermal conductivity in the z direction (k_z) is lower than k_x and k_y. This is due to the fact that the structure of both ReAlSi and ReGaSi is tetragonal i.e a=b and the c dimension is longer, contributing to the anisotropy in the thermal properties. We observe that the thermal conductivity values converge at a length scale of 1.5 microns. The values of k_x, k_y and k_z for ReAlSi range from 1.19, 1.19 and 0.07 $Wm_{-1}K_{-1}$ to 24.37, 24.37 and 13.95 respectively, for the characteristic lengths changing from 1 nm to 1.5 microns and beyond. Through our calculations we also observe that ReAlSi and ReGaSi exhibit similar thermal properties for the length scales ranging from 1 nm to 50 nm, after which we see a significant difference in thermal conductivity values between the two material systems.

We also looked the thermal conductivity behavior of ReAlSi and ReGaSi as a function of ambient temperature, and summarized them in Tables. 7.1 and 7.2 respectively. Thermal conductivity for these materials can be computed in Quantum ESPRESSO by solving the Boltzmann Transport Equation (BTE) by using the Single Mode Relaxation Time Approximation (SMA) or by exactly solving the equation through Conjugate Gradient algorithm with Pre-conditioning (CGP). It has been understood that the SMA solution for temperatures lower than 300 K is fairly inaccurate, but

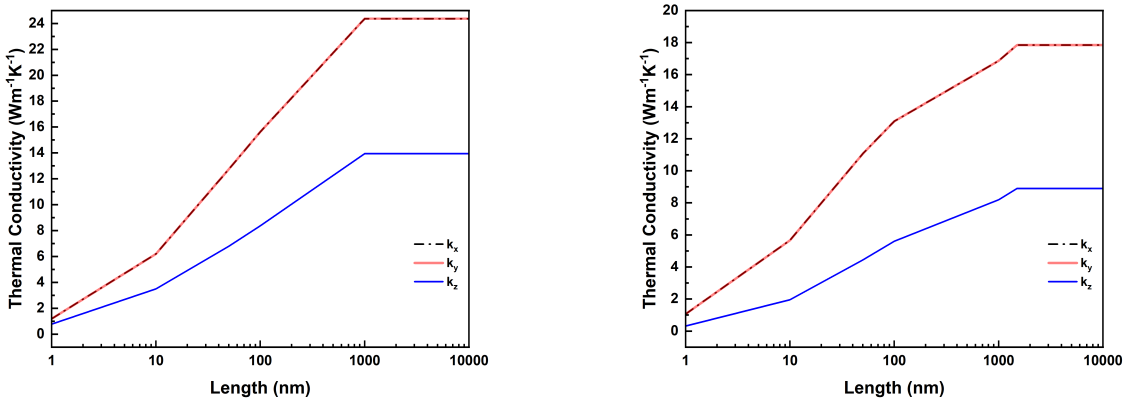

Figure 7.3: Demonstrating the length dependent thermal conductivity of a) ReAlSi and b) ReGaSi by imposing Casimir scattering

for temperatures beyond 300 K, the SMA and the CGP solutions agree within a certain percentage. Within the range of 50 to 1000 K, the difference in the SMA and CGP results is around 26% to 1% for ReAlSi, while for ReGASi, the thermal conductivity values vary from 15% to 3.4% for the k_x and k_y. For k_z this percentage change of thermal conductivity values between the two methods ranges from 45% to 30% for ReAlSi and 4% to 1% in ReGaSi. An important thing to note is that the calculation done using the Conjugate Gradient algorithm with Pre-conditioning (CGP) based solution took almost 3 weeks as compared to the Single Mode Relaxation Time Approximation (SMA) based solution which took 3 days. Therefore, considering computational inexpensiveness of the SMA solution alongside a small loss in accuracy to the exact solution for temperatures between 300 K and 1000 K (a range where the characterization of material for thermoelectric device applications) prompted us to utilize the SMA calculations for our analysis in this section.

For both ReAlSi and ReGaSi, the thermal conductivity values in the temperature range of 700 to 1000 K change only by 30%. This could indicate that the material is thermally stable at really high temperatures without demonstrating any significant change in its thermal properties, providing more reasons to why the materials are excellent candidates for thermoelectric device

Table 7.1: Thermal conductivity for ReAlSi computed using SMA and CGP methods

Temp (K)	**SMA: k (W/mK)**			**CGP: k (W/mK)**		
	k_x	k_y	k_z	k_x	k_y	k_z
50	528.94	528.94	347.50	670.21	670.21	518.33
100	118.36	118.36	66.66	124.93	124.93	92.78
200	39.80	39.80	22.26	40.55	40.55	29.96
300	24.37	24.37	13.95	24.69	24.69	18.49
400	17.74	17.74	10.30	17.95	17.95	13.55
500	14.01	14.01	8.20	14.15	14.15	10.74
600	11.59	11.59	6.81	11.70	11.70	8.90
700	9.90	9.90	5.83	9.99	9.99	7.61
800	8.63	8.63	5.09	8.71	8.71	6.65
900	7.66	7.66	4.52	7.72	7.72	5.90
1000	6.88	6.88	4.07	6.95	6.95	5.31

Table 7.2: Thermal conductivity of ReGaSi computed using SMA and CGP methods

Temp (K)	**SMA: k (W/mK)**			**CGP: k (W/mK)**		
	k_x	k_y	k_z	k_x	k_y	k_z
50	216.96	216.96	141.95	249.89	249.88	147.32
100	66.24	66.24	35.84	71.89	71.89	36.49
200	27.66	27.66	14.10	29.05	29.05	14.24
300	17.84	17.84	8.90	18.58	18.58	9.01
400	13.24	13.24	6.58	13.74	13.74	6.63
500	10.55	10.55	5.22	10.93	10.93	5.26
600	8.77	8.77	4.33	9.08	9.08	4.36
700	7.50	7.50	3.70	7.76	7.76	3.73
800	6.56	6.56	3.23	6.79	6.79	3.25
900	5.83	5.83	2.87	6.03	6.03	2.89
1000	5.24	5.24	2.58	5.42	5.42	2.60

applications. The drop of thermal conductivity from 50 K to 300 K for both the materials is steep and significant, which is approximately 2700% and 1300% respectively.

7.4 Phonon q-grid Convergence in Quantum Espresso and Sheng-BTE for ReAlSi

7.4.1 Phonon q-grid Convergence QE

Our intention with this study is to understand the consequences of choosing a coarse or fine q-point grid for phonon calculations on the computation time and reason it through the lens of the accuracy of the results. For this we commence with our analysis on ReAlSi's crystal structure.

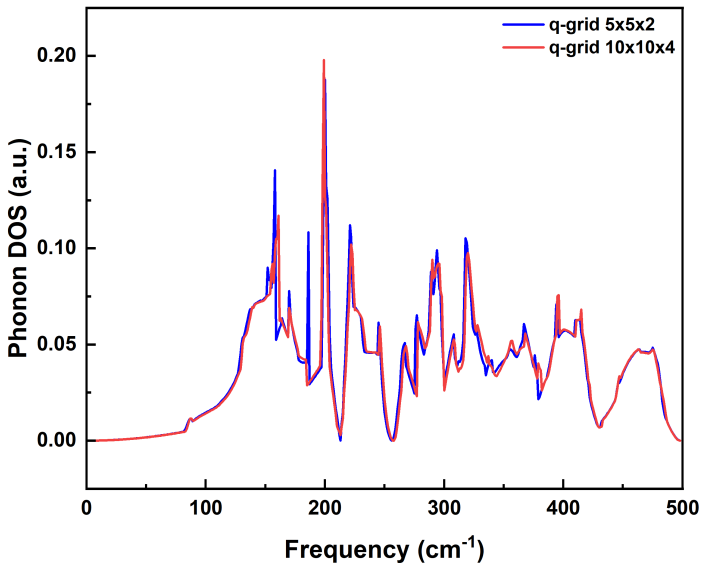

Figure 7.4: Comparison of phonon density of states across 2 q-grid points for ReAlSi

We first plot the phonon density of states (PDOS) of the two q-point grids under investigation. From the Fig. 7.4, we can observe that the PDOS from both the meshes sizes have an excellent agreement, which is indicative of the convergence of the phonon spectrum with respect to the

Brillouin-Zone (BZ) sampling. In both the cases, we observe minor differences in the amplitudes of some of the density of states (DOS), with some peak smoothening observed for the larger mesh, confirming that a coarse q-point grid of 5x5x2 is sufficient for vibrational and thermodynamic analysis. The absence of any DOS at the negative or imaginary frequencies is indicative of the dynamic stability of the material system under study.

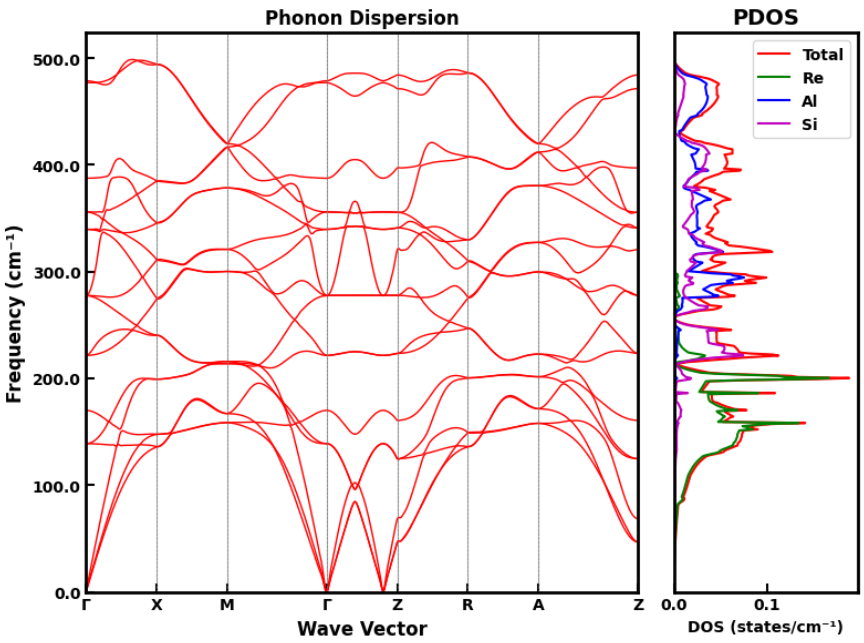

Figure 7.5: Phonon dispersion and phonon density of states for ReAlSi

Looking at the elemental contribution of Re, Al and Si individually to the phonon density of states for ReAlSi compound from Fig. 7.5 , the heavy Re atom dominates the low frequency region, while the lighter Al and Si atoms are responsible for the vibrational modes in the higher frequency range. We observe crossing over of phonon modes in many bands across the frequency range in the phonon dispersion diagram, across the high symmetry path for a tetragonal structure. As expected we observe three acoustic phonon modes TA1, TA2 and LA originate at 0 cm^{-1} at the Γ point in the BZ, with an expected linear behavior, with the one of the modes extending up to approximately 220 cm^{-1}. We see the Re atom also contributes to 2 low frequency optical modes originating at 150 cm^{-1} and 180 cm^{-1}, which is where we see the first of the sharp peaks observed

in the PDOS diagram discussed before. The Al and Si atoms contribute to mid and high frequency optical vibrational modes, which is indicative of their lighter mass. A wider range of bands in the optical region is due to the complexity of ternary material's multi atom system and its mixed bonding environment.

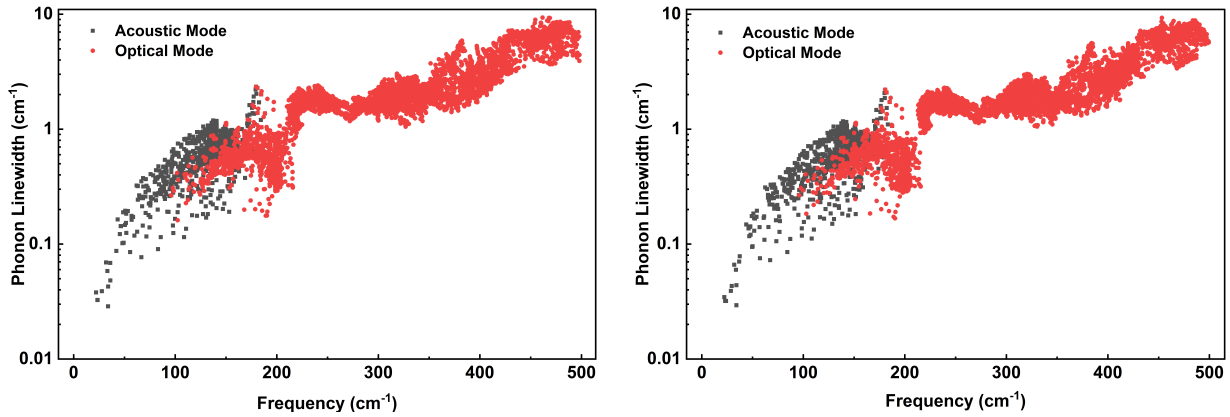

Figure 7.6: Comparison of phonon linewidths for ReAlSi across 2 q-grid points a) 5 x 5 x 2 and b) 10 x 10 x 4 in QE

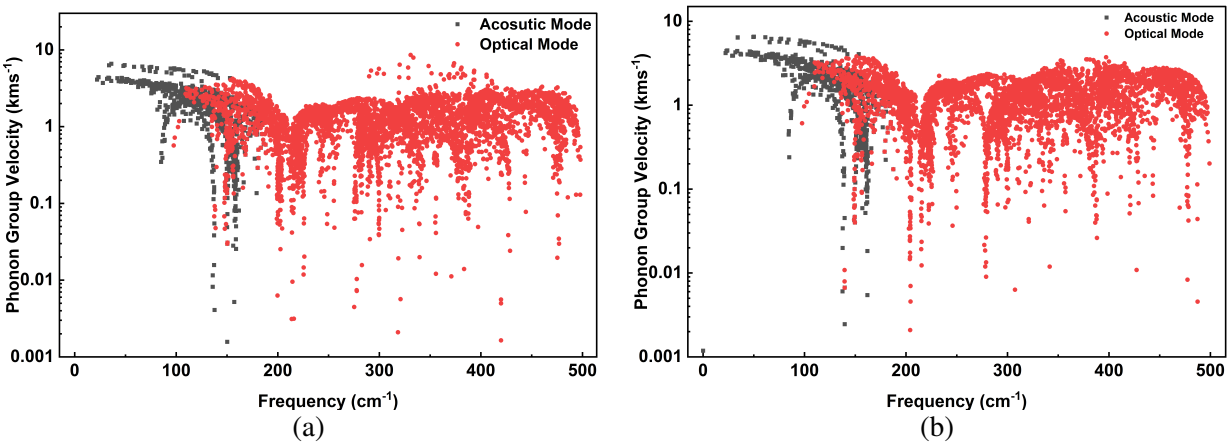

Figure 7.7: Comparison of phonon group velocity for ReAlSi across 2 q-grid points a) 5 x 5 x 2 and b) 10 x 10 x 4 in QE

Apart from the excellent agreement in the phonon density of states for the two different mesh sizes, from Figs. 7.6 and 7.7, we see an excellent agreement in the phonon linewidth and phonon

group velocity plots for ReAlSi. It is also approximately where the contribution from the Re atom ends, where comparatively, lower linewidths and higher group velocities are observed. The phonon in this region of 0 cm^{-1} to 220 cm^{-1} have lower linewidhts and higher velocities as compared to phonons in frequency range greater than 220 cm^{-1}, which tells us that these phonons contribute towards the higher thermal conductivity of the material, as they travel longer and faster.

It is worthy to note that majority of the phonons are in this high frequency range, indicating that thermal conductivity of the material is dominated by the shorter mean free path and slower optical phonons. A transition from acoustic to optical modes is clearly observed in the 150 cm^{-1} to 200 cm^{-1} range explained through the increasing linewidth and decreasing group velocity of the phonons in this range, which is also confirmed by the phonon dispersion diagram.

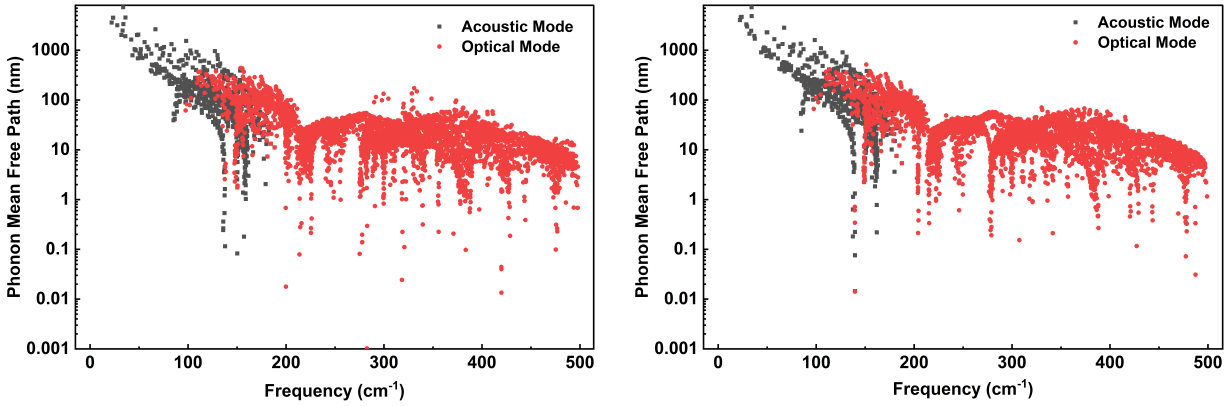

Figure 7.8: Comparison of phonon group velocity for ReAlSi across 2 q-grid points a) 5 x 5 x 2 and b) 10 x 10 x 4 in QE

Interestingly, we also observe that in the higher frequency range, the linewidths steadily increase, i.e. the phonon travel a shorter distance, but their group velocity remain relatively unchanged. We then compute the mean free paths for the same set of phonons, and observe that the mean free paths (MFPs') from Fig. 7.8 exhibits a similar trend that is observed in the group velocity plot. We now simulate the ReAlSi material system using another solver named ShengBTE.

7.4.2 Phonon q-grid Convergence from ShengBTE

We utilized ShengBTE to replicate our results from Quantum ESPRESSO. We observe an excellent agreement in the vibrational frequencies of the modes, the acoustic-optical separation along with linewidth and velocity magnitudes. This is an indication that the conversion of 2nd order force constants from Quantum ESPRESSO to ShengBTE did not introduce any anomalies or discrepancies, which is essential for integration of two methods. Although the 3rd order force constants were independently generated for both methods, the agreement between the results shows consistency in the force constant calculation method across different solvers, as shown by Figs. 7.9, 7.10 and 7.11. Even in ShengBTE for both the q-point grids, the data looks exactly the same as the one obtained in Quantum ESPRESSO, which is essential in validating our results of the physical parameters, such as the thermal conductivity of the material.

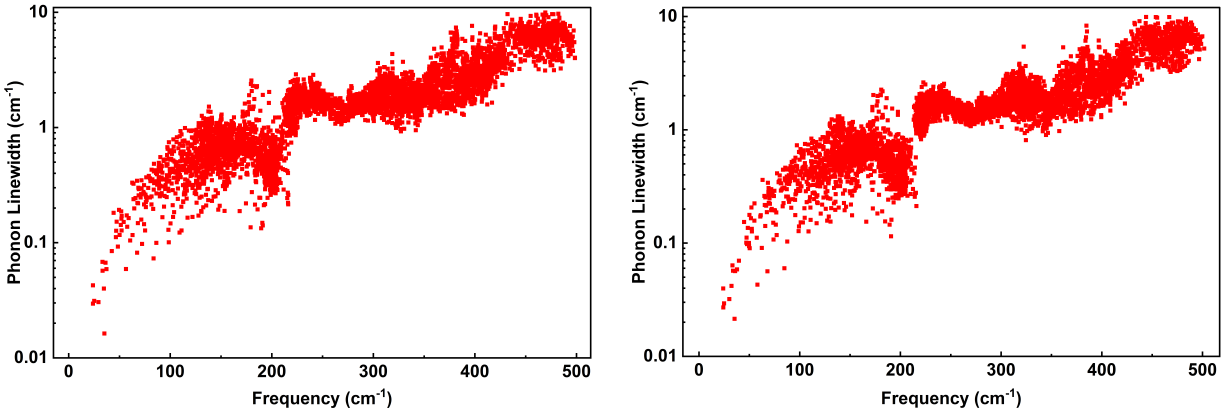

Figure 7.9: Comparison of phonon linewidths for ReAlSi across 2 q-grid points a) 5 x 5 x 2 and b) 10 x 10 x 4 in ShengBTE

This analysis also helped us in solidifying our understanding of the procedure to conduct computational analysis using ShengBTE, which will come handy in our quest to analyze the ReSi system.

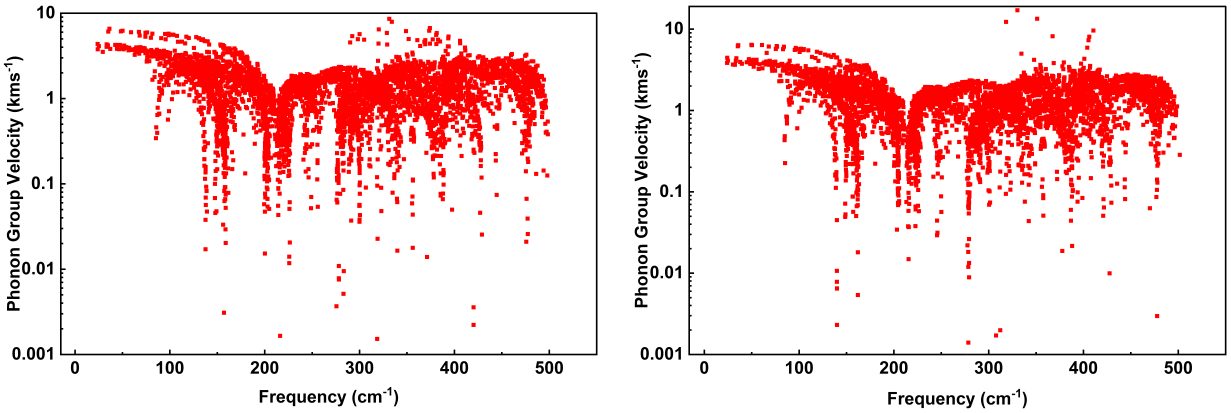

Figure 7.10: Comparison of phonon group velocity for ReAlSi across 2 q-grid points a) 5 x 5 x 2 and b) 10 x 10 x 4 in ShengBTE

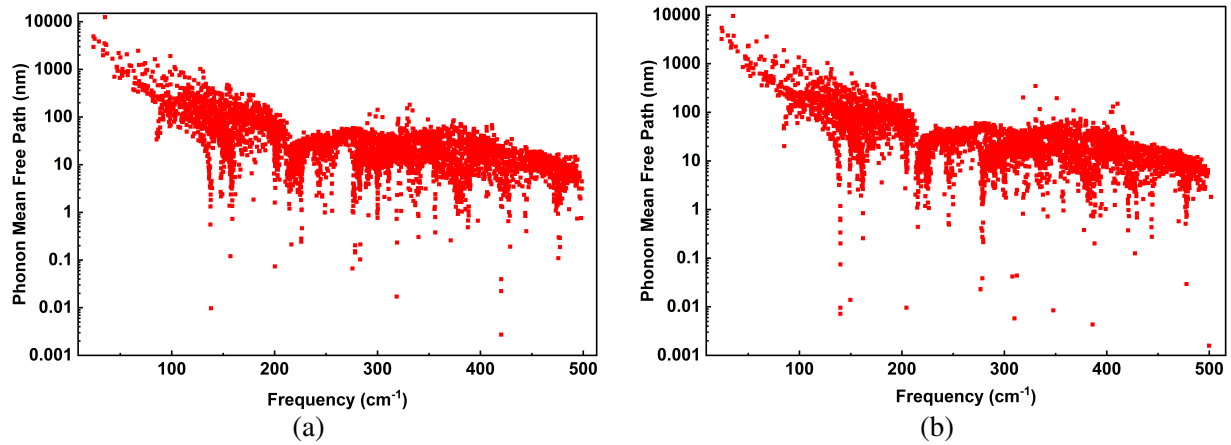

Figure 7.11: Comparison of phonon mean free path for ReAlSi across 2 q-grid points a) 5 x 5 x 2 and b) 10 x 10 x 4 in ShengBTE

7.5 Thermal Conductivity Measurement of ReGaSi using Quantum ESPRESSO

For ReGaSi, we apply a similar kind of analysis that we did for ReAlSi. Just with the mere substitution of Al with Ga, the expectation is to observe a change in the phonon dispersion and phonon density of states spectrum, which is clearly observed between the Figs. 7.12 and 7.5 for

ReGaSi. In the case of ReAlSi, due to the atomic masses of Si and Al being closer to each other (28.08 and 26.98 respectively), there is an observable similarity in their elemental density of states spectra, with distinguishable differences in the magnitudes of the density of states, notably the magnitude being higher for Al than Si. But in the case of ReGaSi, the Re and Ga atoms are heavier than Si, due to which see some density of states for Re and Ga in the low frequency range of 0 cm^{-1} and around 230 cm^{-1}.

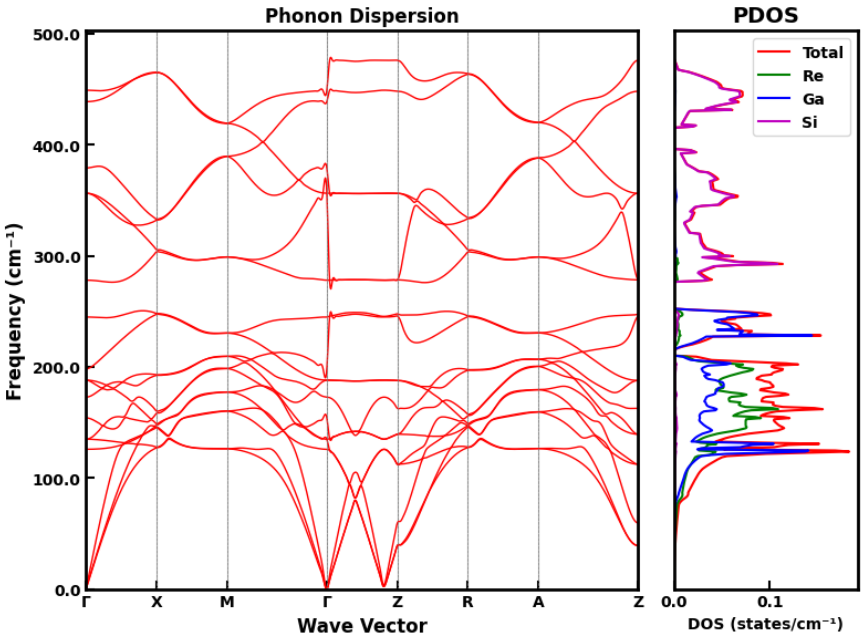

Figure 7.12: Phonon dispersion and phonon density of states for ReGaSi

Firstly, a distinct phonon band gap is observed in the ReGaSi phonon dispersion, marked by a frequency region in which no phonon branches occur between the two distinct optical modes. This gap is also clearly reflected in the phonon density of states, which exhibits a corresponding interval of zero vibrational states. The presence of this phonon band gap originates from the large mass contrast among Re, Ga, and Si atoms, which leads to a strong separation between low-frequency optical modes dominated by the heavy Re atoms and the higher-frequency optical modes associated primarily with the lighter Ga and Si atoms.

Another effect of this mass sensitivity of the phonon dispersion is that it gives rise to the

acoustic-optical mode transition that occurs much quicker in ReGaSi at around 120 cm^{-1}, extending up to around 180 cm^{-1}. This signifies that the bands representing the acoustic modes in ReGaSi have shallower slopes compared to the steeper slopes for the band in ReAlSi. Within this same frequency range we saw only two optical bands in the ReAlSi phonon dispersion diagram, where here we see 7 low frequency optical bands. This can be reasoned by examining the phonon dispersion with the phonon density of states for ReGaSi, where due to the significant mass mismatch between the constituent elements, we see multiple low frequency optical modes. The high frequency range is completely dominated by Si only. The optical bands in the high frequency range are flatter and smoother for ReGasi than that of ReAlSi. All these factor suggests a lower lattice thermal conductivity of ReGaSi and compared to ReAlSi, which is what we observe from our computed values from Tables. 7.1 and 7.2.

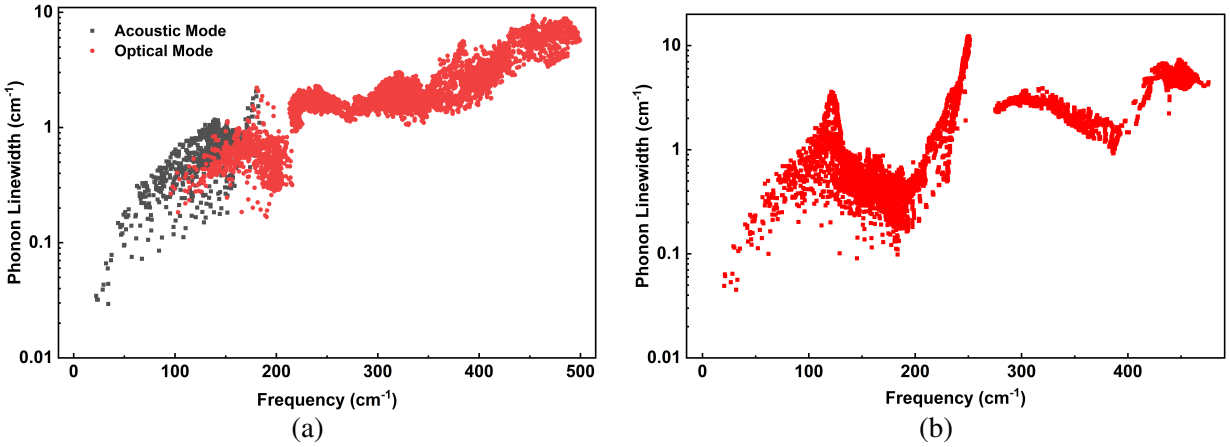

Figure 7.13: Phonon linewidth comparison for a) ReAlSi and b) ReGaSi

In Fig. 7.14, we can clearly see how the multiple optical modes that develop above the acoustic modes in the ReGaSi manifest themselves in the group velocity plots. This is done by observing the number of vertical lines that form in these plots for both the materials. The lowering of the group velocities is due to the heavier mass of Ga atom. The frequency range where no density of states are observed is also visible in the linewidths and the group velocity plots. The increase in the groupings of the phonons in the low frequency region (below the 230 cm^{-1}) in ReGaSi as

compared to ReAlSi, corresponds well to the total phonon density of states observed for both the materials.

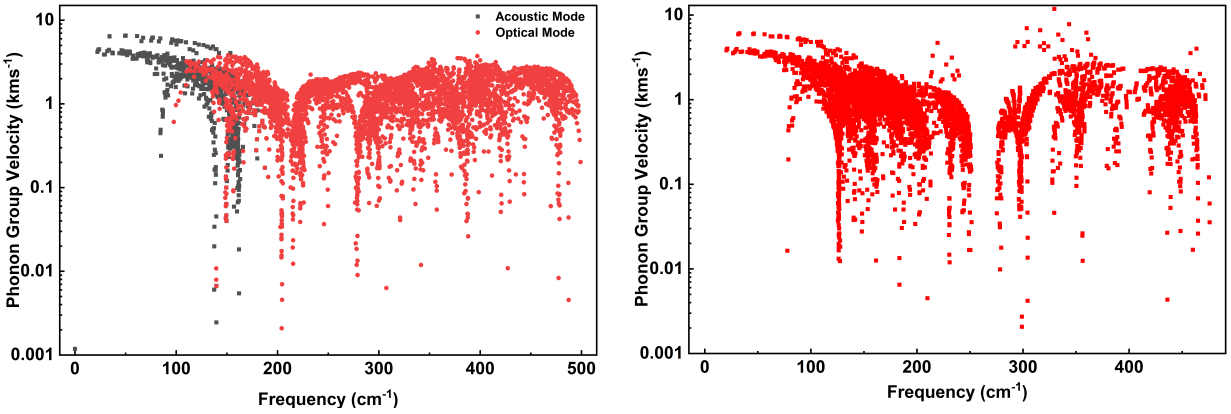

(a) (b)

Figure 7.14: Phonon group velocity comparison for a) ReAlSi and b) ReGaSi

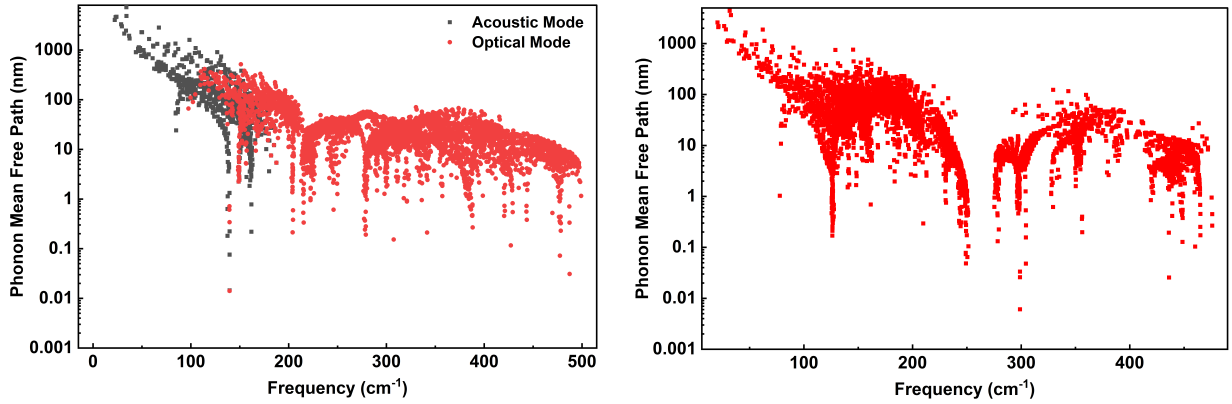

(a) (b) fig 7.15b

Figure 7.15: Phonon mean free path comparison for a) ReAlSi and b) ReGaSi

7.6 Thermal Conductivity Calculation of ReSi using ShengBTE

$ReSi_{1.75}$ is the Rhenium Silicide structure that we are to analyze in this section of the chapter. This is the base transition metal silicide from which, through substitutions, computational and experimental methods, ternary ReAlSi and ReGaSi were developed. The thermal conductivity of

single crystal Re_4Si_7 has been measured experimentally using Time-Domain Thermoreflectance Method (TDTR) and is reported to be 4.5 $Wm^{-1}K^{-1}$ in the in-plane direction and a value of 3.9 $Wm^{-1}K^{-1}$ in the through plane direction[183]. Through our computational analysis, we were able to demonstrate the thermal conductivity values of k_x, k_y, and k_z to be around 3.36 $Wm^{-1}K^{-1}$, 4.48 $Wm^{-1}K^{-1}$ and 4.23 $Wm^{-1}K^{-1}$ respectively, which is in good agreement with the published literature values. This validation sheds light on the thermal transport mechanisms in Re_4Si_7.

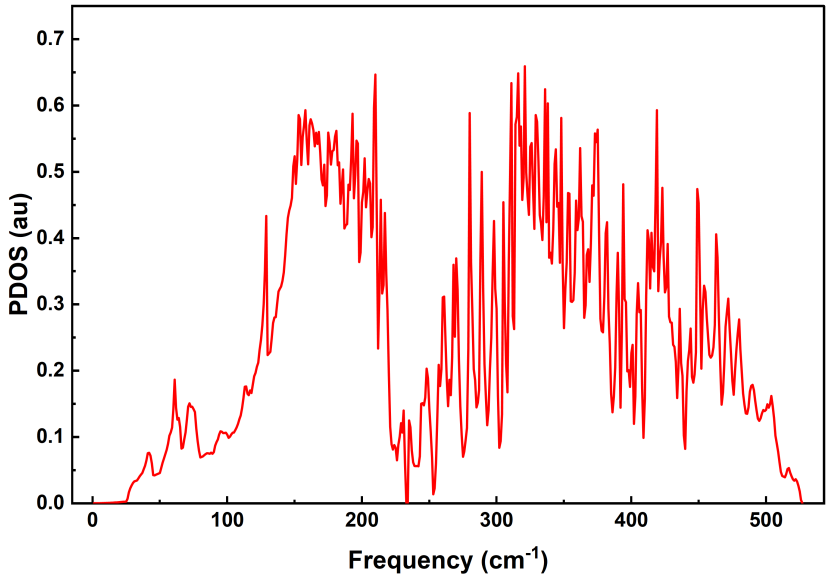

Figure 7.16: Phonon density of states for ReSi

Analyzing the phonon density of states diagram (Fig. 7.16), we clearly see that the magnitudes of the density of states for this material system across the vibrational frequency range is significantly higher compared to those of ReAlSi and ReGaSi. Due to presence of a large number of vibrational modes at each frequency range, it can contribute to significant phonon-phonon scattering to be induced in the material system, leading us to believe that the thermal conductivity of the material would be significantly lower than ReAlSi and ReGaSi, which now we know is true.

Around 240 and 250 cm^{-1} frequencies is where the lowest magnitude of the phonon density of stats occur, which leads to a slight separation between the lower and the higher frequency modes, which is not as significant as observed in ReGaSi. Peak broadening is observed in the region where

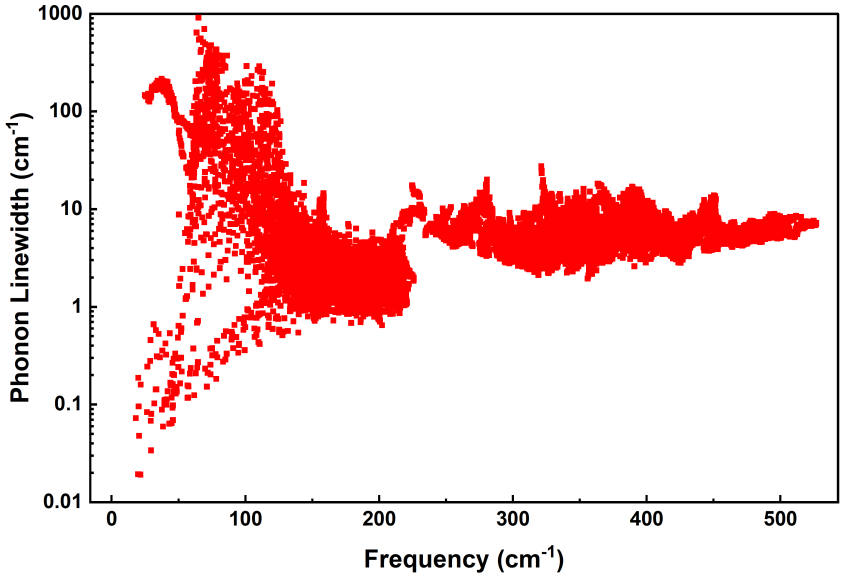

Figure 7.17: Phonon linewidths for ReSi

the effects or Rhenium are dominant, whereas in the region where silicon is dominant, sharper density of states peaks are observed. This indicates the presence of larger variety of vibrational modes for Re atoms, but for the Si dominated region, the number of phonons vibrating at that particular frequency is significantly increased. Interestingly, the group of phonons in the frequency range range of 0 to 130 cm^{-1} have an abnormally large range of linewidths, ranging from 0.02 cm^{-1} to 1000 cm^{-1}. The majority of the phonons in this group of vibrational frequency have a linewidth in the range of 2 to 100 cm^{-1}. Apart from this abnormal region, the phonon linewidths experience a slight increase, but largely remain unchanged with most of the phonon being in the 1 to 10 cm^{-1} region.

Another interesting observation is that a majority of the phonons in the group below the vibration frequency of 230 cm^{-1} have a significantly larger mean free paths, while the velocities of the same phonon group is consistently the same throughout the vibrational frequency range. The net effect of this is that the majority of the phonons experience a consistent mean free path in the range of 0.1 nm to almost 10 nm as seen in Fig. 7.19. Such low mean free path values for the various phonon groups contribute to the significantly low thermal conductivity of Re_4Si_7, compared to its

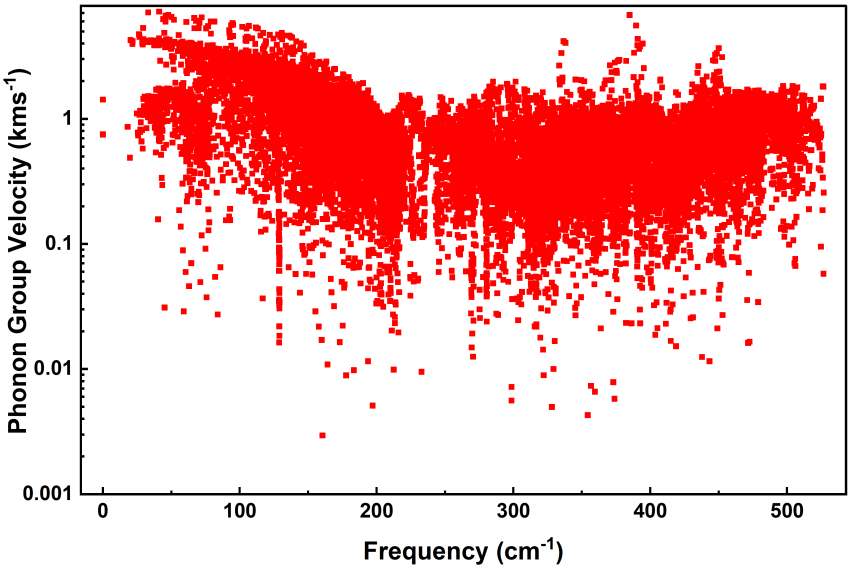

Figure 7.18: Phonon group velocity of ReSi

ternary compound counterparts.

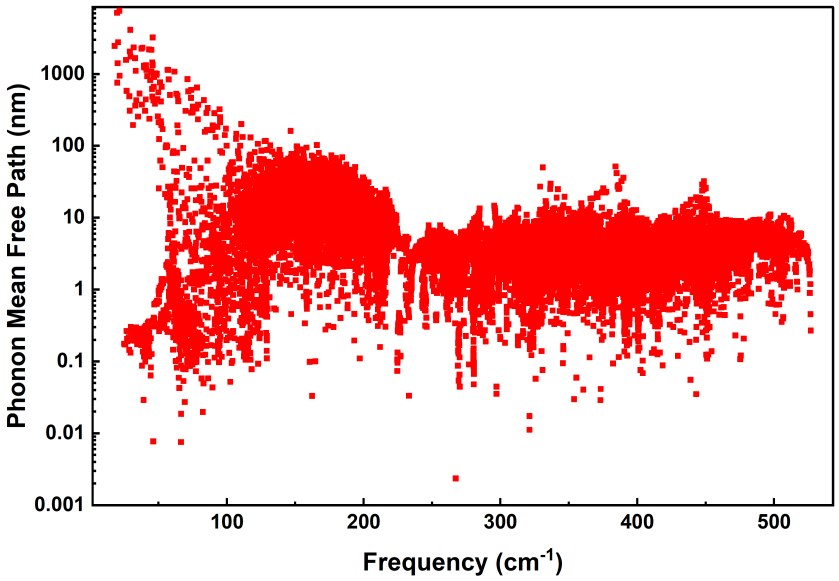

Figure 7.19: Phonon mean free path for ReSi

7.7 Examining the Effects of 2% Biaxial Strain on ReAlSi and ReGaSi

Bi-axial compressive strain effects were induced in the system by changing the lattice parameter of the materials by 2%. The system was then relaxed by fixing the a and b dimensions, while keeping the c dimension of the crystal structure free by using the 'Epitaxial ab' flag in the vc-relax and scf input files for Quantum ESPRESSO.

Looking at the phonon dispersion plots, we observe a slight shift in the phonon frequency range of the vibrational modes. This slight increase in the frequencies results in a small percentage increase in the thermal conductivity values of both ReAlSi and ReGaSi. A certain amount of curve smoothening was also observed between the un-strained and the strained materials.

An increase of 13% and 8% in the thermal conductivity values was observed in the ReAlSi and ReGaSi materials systems respectively. While the overall reduction in the phonon linewidths is slightly more evident for ReAlSi, for ReGaSi, we do not see any such effect significantly.

The same can be said about the phonon group velocity, where a slight increase in the phonon group velocity is observable in ReAlSi, but for ReGaSi, that difference is not quite discernible. The mean free path calculations also suggests that the increase in mean free path seems to be larger in magnitude for ReAlSi as compared to ReGaSi. Hence, there is a slightly higher increase in thermal conductivity for ReAlSi and compared to ReGaSi, but this increase in thermal conductivity is not significant. This is a significant result as one can deduce the fact that the thermal conductivity of the material remains relatively unaffected to the applied stress. Along with their relative stability at high temperatures as discussed in the earlier sections of the chapter, one can definitely state that these materials are definitely a strong candidate for the development of thermoelectric devices.

We also plot the percentage contribution of the phonon modes to the material's thermal conductivity (Fig. 7.24. The total contribution to thermal conductivity from acoustic modes are significantly smaller compared to that of the total optical modes. A large contribution to the thermal

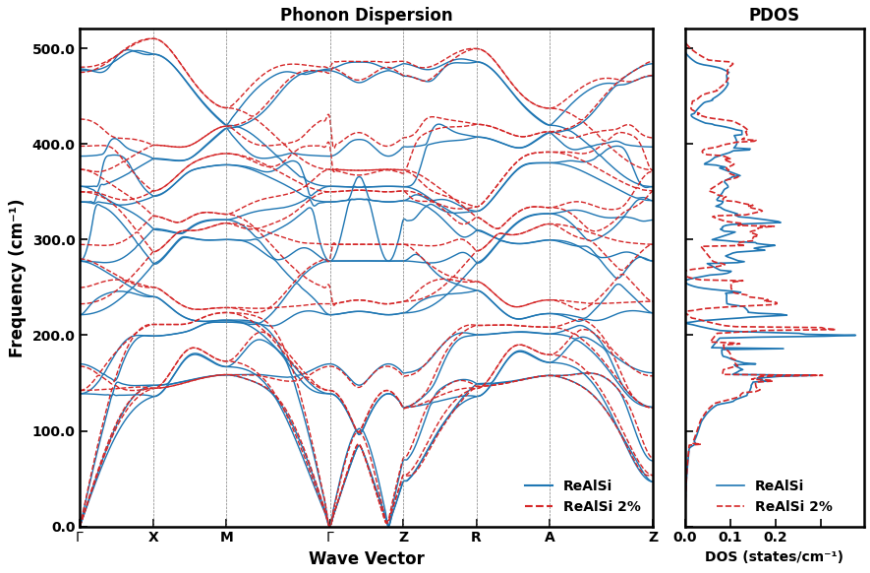

(a)

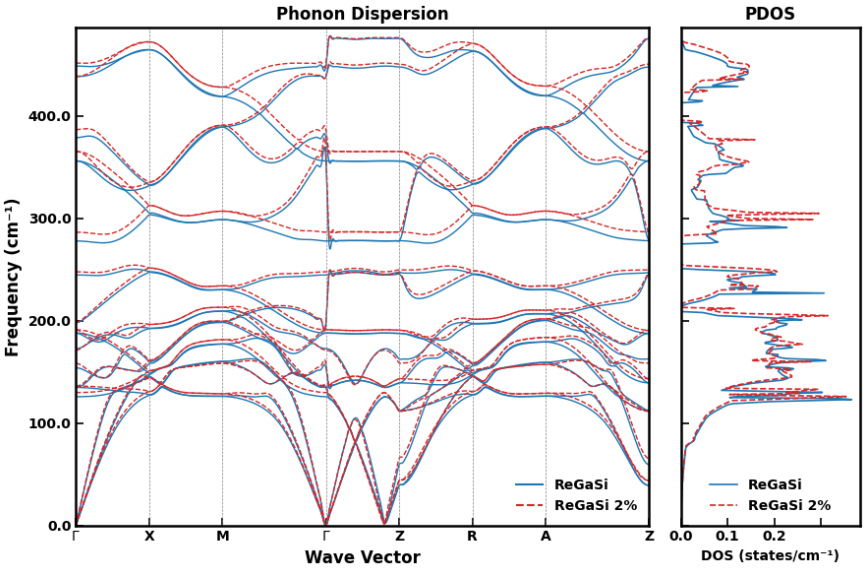

(b)

Figure 7.20: Phonon dispersion and phonon desnity of states comparison for both no strain and 2% strain for ReAlSi and ReGaSi

conductivity of the material is made up by the mixed phonon modes.

Due to the application of the bi-axial compressive strain, the contributions from the LA and LO modes remain relatively unchanged. The contributions from the from the TA and TO modes seems to decrease and at the same time, the contributions from the mixed phonons increases by almost

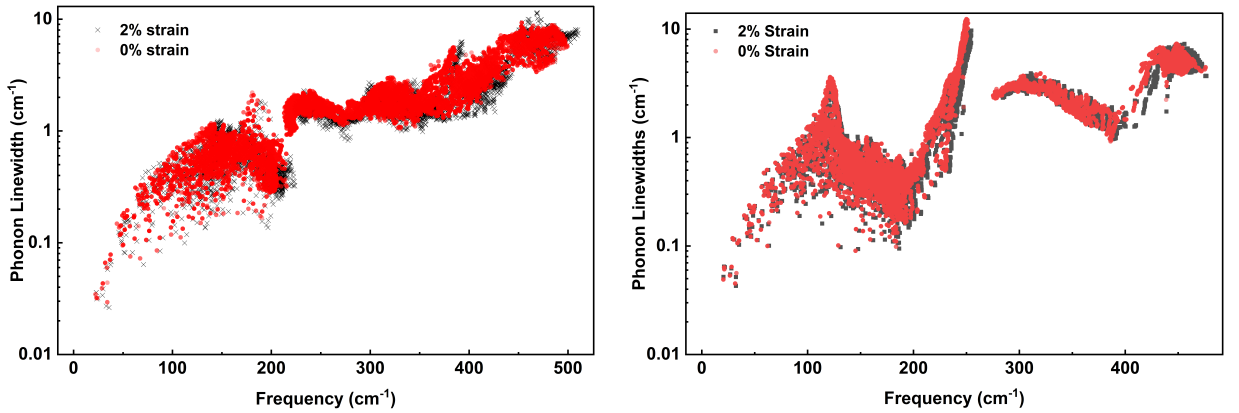

Figure 7.21: Phonon linewidth comparison for 2% strained a) ReAlSi and b) ReGaSi

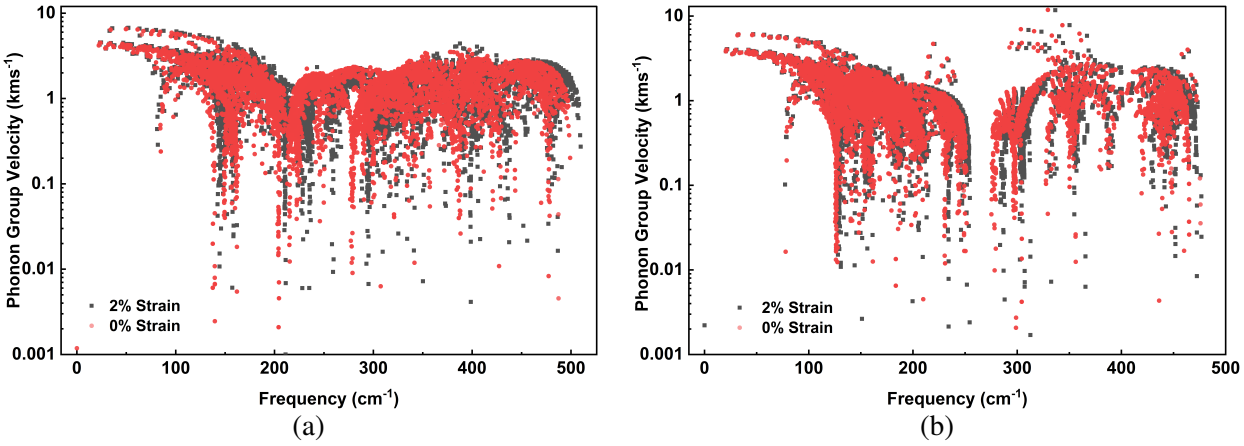

Figure 7.22: Phonon group velocity comparison for 2% strained a) ReAlSi and b) ReGaSi

the same amount. This could be the reason why we did not observe a huge change in the thermal conductivity values of the strained materials.

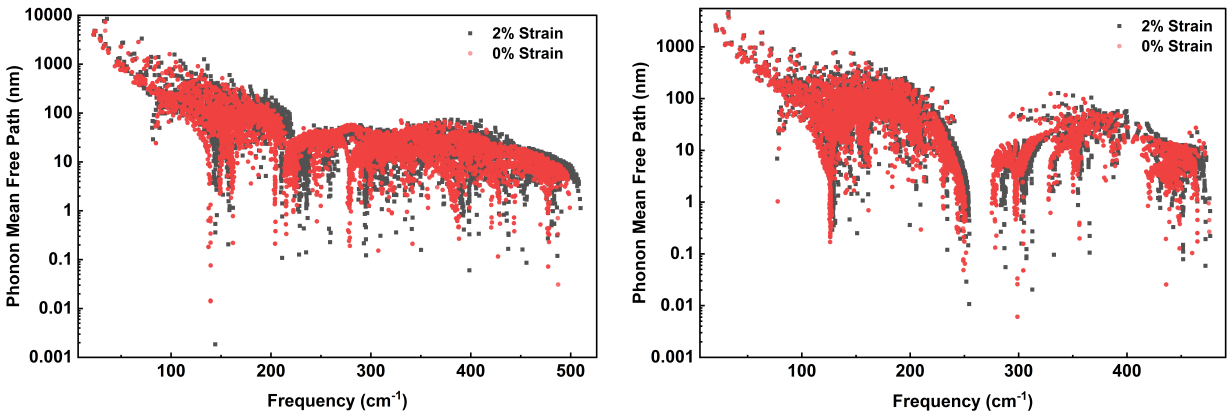

Figure 7.23: Phonon mean free path comparison for 2% strained ReAlSi and ReGaSi

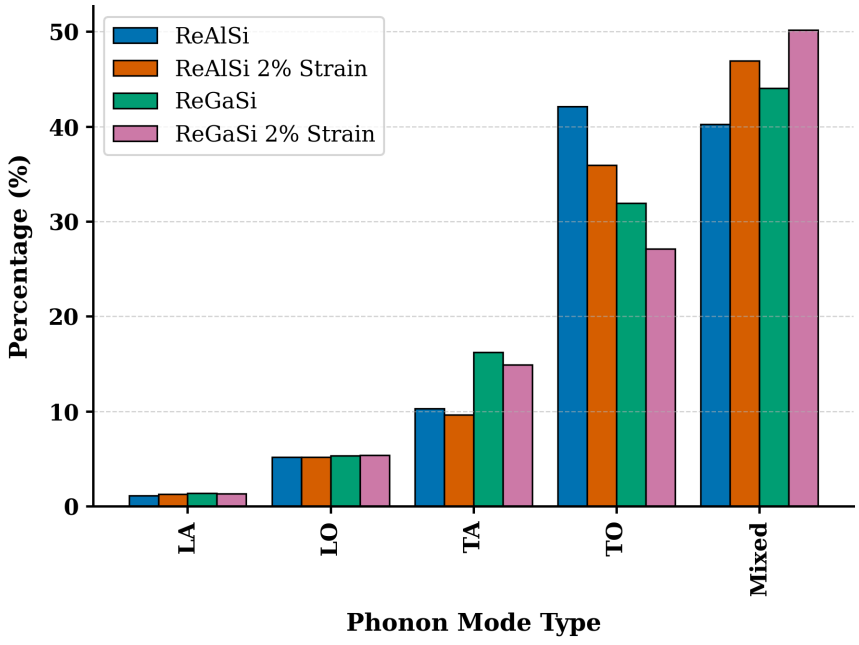

Figure 7.24: Percentage contribution of phonon modes for both unstrained and biaxially 2% strained ReAlSi and ReGaSi

Chapter 8

Understanding the Effects of Annealing on the Thermal Properties of Strontium Chromate (SCO) thin films on Si substrate

8.1 Introduction

Chapter 6 of this dissertation was dedicated to the characterization of Strontium Titanate, while in this chapter we take a look at another material system from the family of oxide perovskites known as Strontium Chromate or (SCO). These materials are extremely tuneable due to interesting interactions between their physical properties that can produce unexplored phenomena, which make them an outstanding candidate for a variety of applications [184, 185, 186, 187]. Due to the subtle inaccuracies in ab initio based DFT calculations that arise because of the nature of electron interactions in complex oxides, accurate prediction of their material properties becomes difficult [188]. Even experimental characterization of these materials remains a problem that needs attention from the scientific community. This problem is even worse, due to the struggles in synthesizing these materials as the material properties are susceptible to minor variations in synthesis conditions, causing it to transition between insulating and metallic states [189]. Because of these reasons, it has been a challenge to accurately characterize the properties of SCO and understand its underlying mechanism through which it exhibits certain material properties. Materials like SCO have been relatively unexplored. Therefore, through the work done in this section, we attempt to provide more understanding of the thermal properties of Strontium Chromate thin films using experimental methods and speculate at the possible reasons that lend these specific properties to the material system.

8.2 Sample Preparation, Transducer Characterization and Modeling

Since the aim of the study was to analyze the effects of annealing environments, we prepared 4 samples, each one of them representing a unique annealing condition. One of the thin films was first annealed on a hot plate set at a temperature of 250°C. The hot plate was allowed to reach up to the set temperature, after which the sample was placed in the middle of the hot plate for a set duration of 2 hours. This sample in this chapter will be referred to as Hot Plate Annealed SCO or HPASCO. We then annealed two other samples, where both the samples were annealed in the tube furnace. In one of the cases, the annealing was done by keeping the tube open from both the sides, to simulate the conditions for annealing in air, which will be referred to as Tube Furnace Annealed SCO (TFASCO). For the other sample, we provided a small and a steady flux of pure Oxygen gas, which traveled through the tube and then was trapped in a 5-gallon water jug. This sample will be called Pure Oxygen Annealed SCO (POASCO). The final sample was an un-annealed pristine sample, which was simply referred to as SCO. The temperature and the duration of the annealing process via. the tube furnace method was kept the same as the one for the hot plate annealing.

Once the samples were annealed, they were then deposited with a thin layer of gold using a gold pellet (99% purity) as a target, for the deposition, purchased from Kurt. J Lesker Company. We used the Lesker Nano36 Evaporator thermal evaporator, (part of Microfabrication Research & Education Center at the University of Oklahoma) to deposit 100 nm of gold film, which is a target thickness set in the thermal evaporator machine as a process parameter. The final gold film thickness achieved will be different from the target set in the deposition machine, as it is based on the position of the sample placed on the sample holder. Before the start of the gold film deposition process, the SCO samples were mounted on the sample stage in the thermal evaporator alongside a reference Si sample, which was required for the characterization of the properties of the gold film (also called the transducer layer).

The structure of the thin film is such that the system has 4 constituent layers comprising of gold transducer, SCO thin film, STO buffer layer and the Si substrate. Drawing from our analysis done in Chapter 6, where we analyzed STO thin films, our task was to resolve the 5n-1 parameters that model the system in FDTR curve fit analysis. Here, n is the number of layers in our sample, which correlates to the model having 19 individual parameters. Out of these 19 parameters, we need to find the volumetric heat capacity and the thermal conductivity of the SCO thin films and thermal boundary conductance at the Au/SCO interface. The rest of the 16 parameters were either evaluated using independent characterization methods or may not affect the curve fit analysis, if the parameter is insensitive to the measurement.

Table 8.1: Properties of the transducer layer characterized using the Si reference sample.

Material	k_{Au} *($Wm^{-1}K^{-1}$)*	**Au Thickness** t *(nm)*	**TBC** *(10^7 $Wm^{-2}K^{-1}$)*
HPASCO	241.03 (21.74)	170.24 (2.46)	4.45 (0.12)
POASCO	280.29 (18.01)	202.76 (2.28)	4.52 (0.22)
SCO	186.07 (34.12)	136.03 (2.37)	4.50 (0.08)
TFASCO	167.20 (25.77)	130.44 (3.21)	4.54 (0.12)

Table 8.1 represents the numerical values of the transducer layer parameters which are important for the evaluation of the thermal properties of un-annealed and annealed SCO thin films. FDTR is a very localized measurement technique and may not capture the total picture as the properties of the materials may vary from location to location. To account for location dependent variations in our transducer layer and the SCO thin film characterization, we measure up to 17 points on each sample, spanning from the middle of the sample to the edges of the samples. The result thus obtained is an average of 17 different measurement on the sample surface. The values in the brackets represents the standard deviation of all the 17 measurements taken.

8.3 Experimental Analysis

8.3.1 Identifying Fixed and Free Parameters for Best Curve Fit Analysis

We now focus on performing the curve fit analysis for our SCO samples, for which we need to nail down our input/fixed parameters, thus reducing the number of unknown parameters that need to be evaluated using the best curve fit method. In the previous section we discussed how characterizing the transducer layer helped evaluate two of the 19 parameters.

For the other 17 parameters, we shift our focus to the sensitivity plots in Figs. 8.2 and 8.1 for the measurements in done in this section. This is done by plotting the absolute change in the phase lag (in degrees) for each of the remaining 17 parameters (although for the sake of having clear illustrations, we are not showing the sensitivity to all the 17 parameters). From the figures, we clearly see that the measurement is sensitive to most of the 17 parameters. The measurement is insensitive to the Thermal Boundary Conductance (TBC) between the SCO and STO film interface and also to the TBC of the STO/Si interface. This is commonly observed in thin films that are deposited on a high thermal conductivity substrate like Si. It is due to this that the heat quickly diffuses through these interfaces, giving no time for the heat to dissipate in the radial direction, which explains the lack of sensitivity to the TBCs' of both the interfaces. This phenomena was also observed in the STO/Si thin film system, discussed in Chapter 6.

Therefore, we consider both the TBCs' as our input parameter with a value equal to that of 1000 $MWm^{-2}K^{-1}$ for our analysis. 15 more parameters remain for the assessment. Using the STO thin film results from chapter 6, we were able to determine the volumetric heat capacity and thermal conductivity values of the 20 nm buffer STO thin film. The thickness was measured experimentally by our collaborators, hence we consider it to be true, although a quick check can be done by looking at the curve fit with the varying STO film thickness, and the curve fit to the measured phase lag gets worse and worse and we go further away from our correct guess. This helps us determine that the thickness of the STO thin film in our SCO system is around 20 nm. With this, we now know

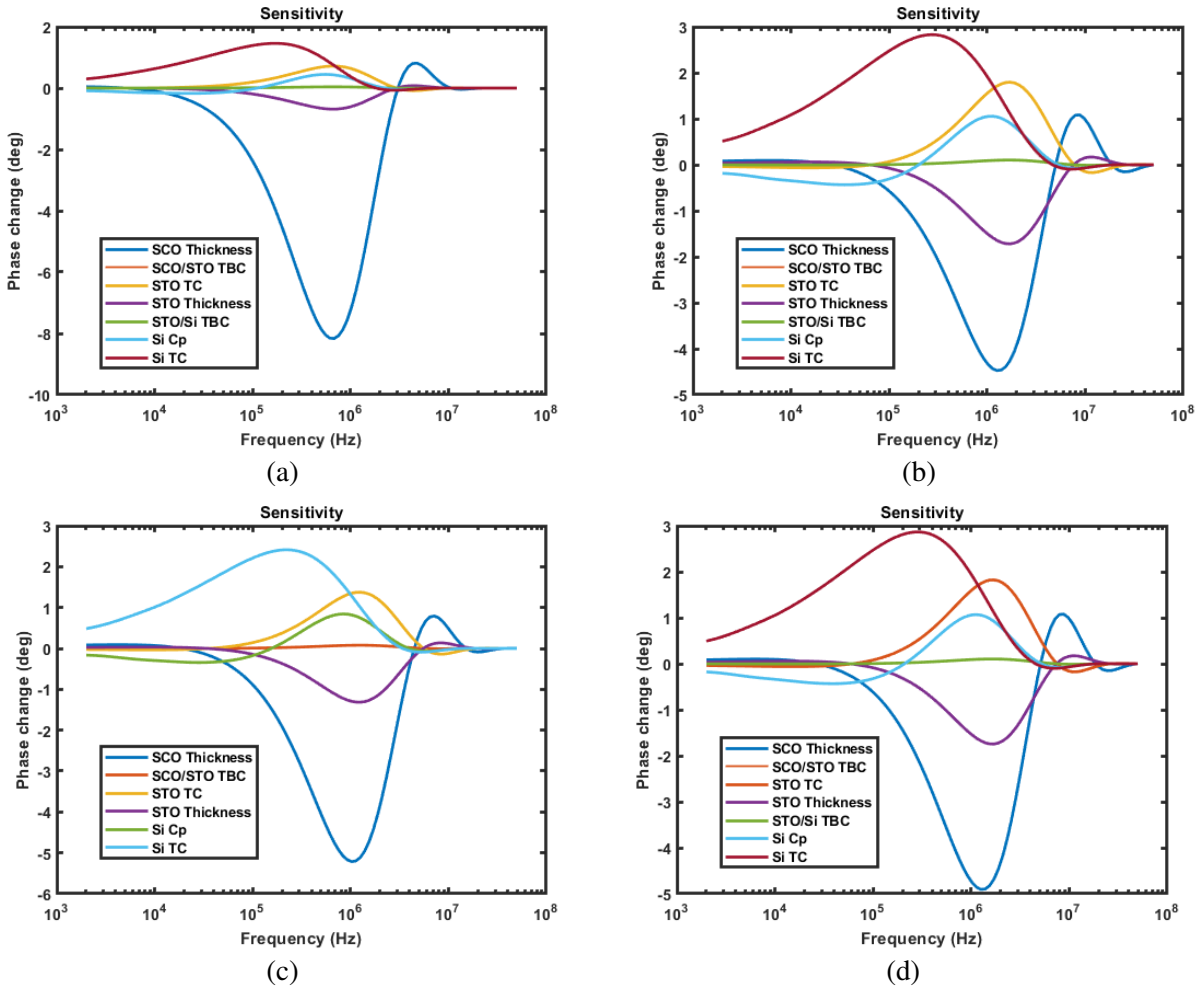

Figure 8.1: Sensitivity of the fixed parameters to the measurement in a) SCO b) HPASCO c) POASCO d) TFASCO

the exact values of the 3 more parameters, reducing our number of unknown parameters to 12.

For the substrate parameters, we use the predefined values for the Si that are available in the model, based on extensive research of the thermal properties in various literature, both experimentally and computationally. Although for FDTR, one thing was observed that as the spot size for high thermal conductivity materials decreases, their thermal conductivity predicted by FDTR should be lower than the preset value. However, for the sake of convenience, we shall go ahead with the predetermined values of volumetric heat capacity and the thermal conductivity of Si.

For thickness, since the Si substrate is quite thick (around 1 mm), it becomes a semi-infinite

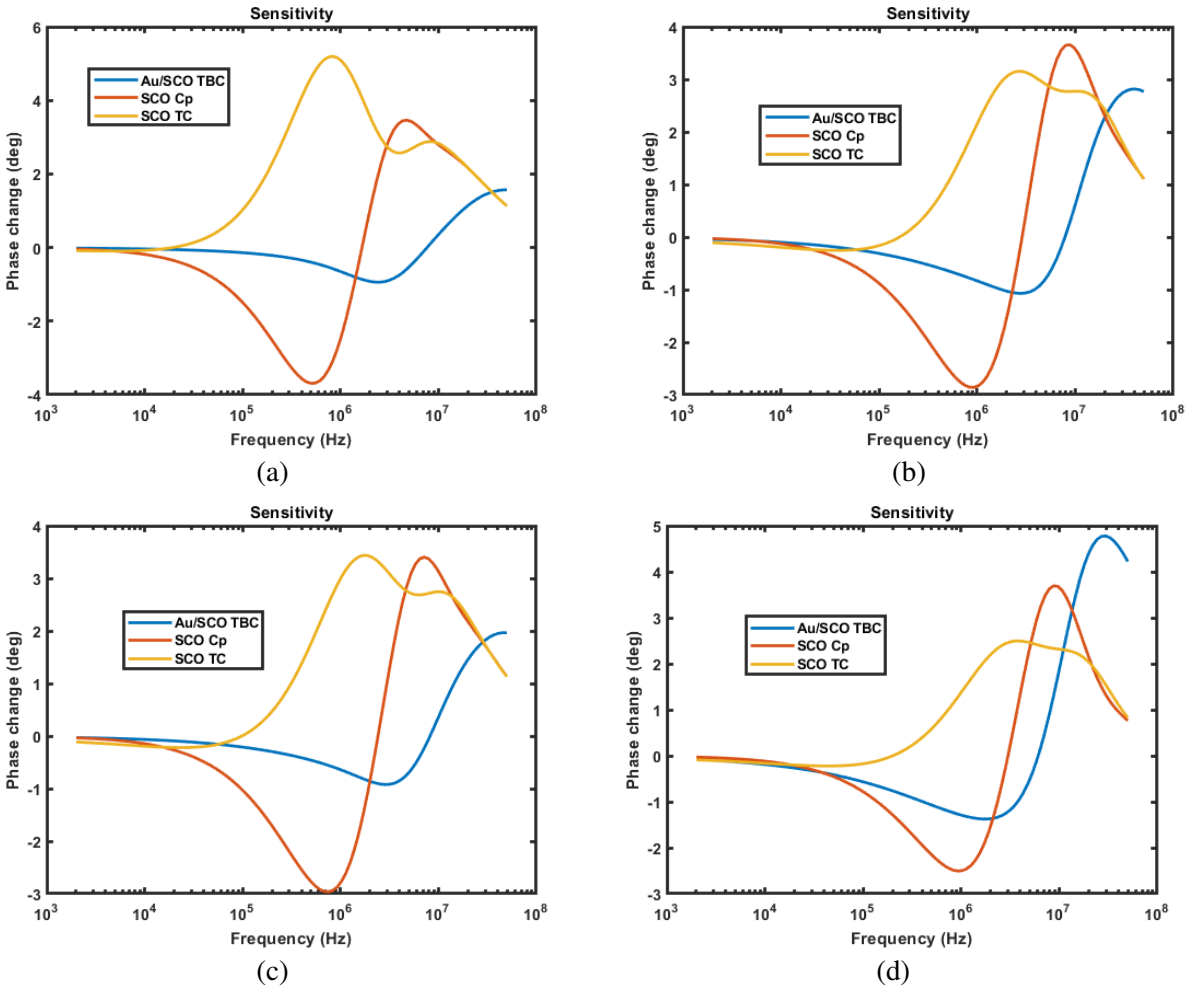

Figure 8.2: Sensitivity of the fitted parameters to the measurement in a) SCO b) HPASCO c) POASCO d) TFASCO

adiabatic boundary as the heat thermalizes quickly into the substrate. This feature of the measurement allows to consider any large value for thickness of the substrate and in our case we consider it to be 1 mm. We also consider the materials to be isotropic and use a anisotropy value of 1 for all the layers, as a known in put parameter. With this we are left with 5 parameters, out of which the volumetric heat capacity of the gold transducer layer is taken from the preset values available to us in the software. The SCO thin film is grown through a meticulous MBE process, which also involves the characterization of the thickness of the SCO thin film, which was also know to us via, the characterization done by our collaborators. This left us with the unknown parameters or free

parameters, that will be evaluated using the curve fit analysis. In our case, these parameters were TBC at Au/SCO interface, volumetric heat capacity of SCO thin film and the thermal conductivity of the SCO thin films. Generally, it is difficult to curve fit both volumetric heat capacity and the thermal conductivity of the material, if their sensitivity plots trace the same path through the modulation frequency range. However, in our case, from Fig. 8.2 we can clearly ascertain that the sensitivities of the volumetric heat capacity and the thermal conductivity of the SCO thin film have distinctly different traces, due to which fitting them together is possible in this particular scenario.

8.3.2 Best Cuve Fit Analysis using Phase Lag Plots

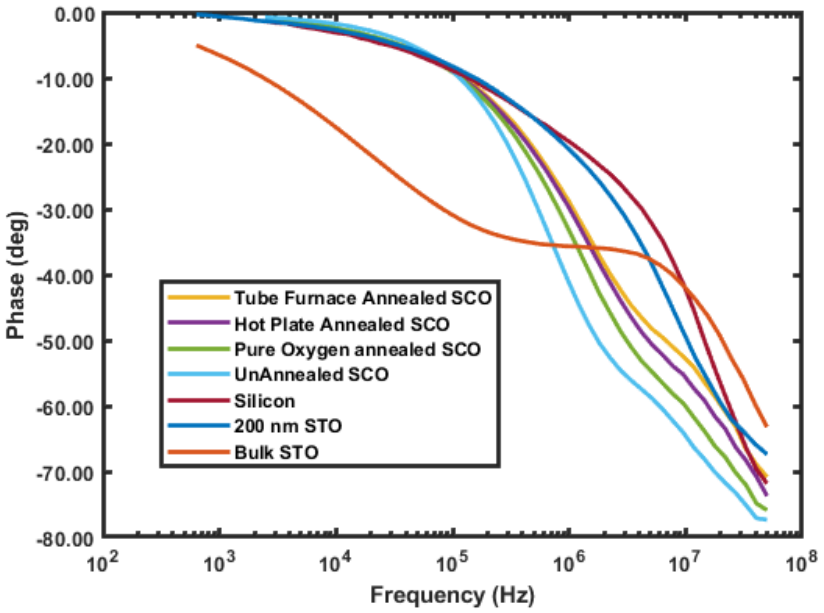

Figure 8.3: Comparison of the phase lag plots from different samples

Fig. 8.3 represents the phase lag plots for all the samples used in our analysis, along with some measurements of thin film STO and bulk STO for comparison as STO and SCO systems are very similar in nature due to their perovskite structure. Comparison of the bulk and thin film STO phase lag plots highlights the effect substrates have on the thin film thermal characteristics, as noted from our analysis in Chapter 6. This may be due to the commensurate growth of thin films that closely

match the lattice parameter of the substrates they are deposited on. A similar response should be expected for SCO thin films if compared to the SCO bulk single crystal.

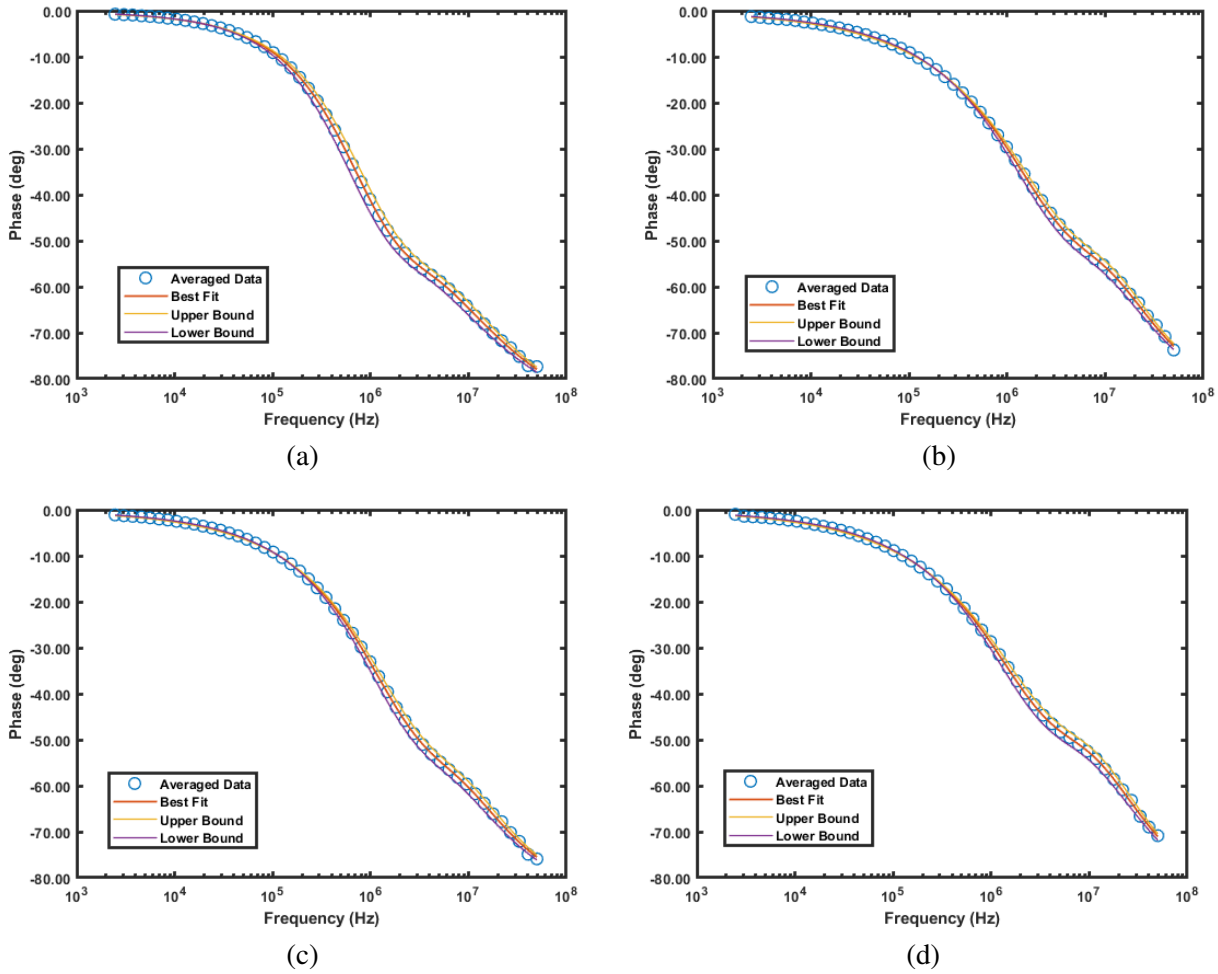

Figure 8.4: Best curve fit plots for a) SCO b) HPASCO c) POASCO d) TFASCO

Upon closer observation of the Fig. 8.3, we determine that the thermal properties of the unannealed SCO, POASCO and TFASCO samples have a similar trend up until the modulation frequency of approximately 200,000 Hz, after which the phase lag plots for the samples start to differentiate from each other. This distinct differentiation in the high modulation frequency range is indicative of the fact that the thermal conductivity of these films will be unique and different to each other. The phase lag plots for both the HPASCO and the TFASCO overlap each other until 7-8 MHz range, after which there is a slight difference.

The implication of this is seen from the thermal conductivity values in table 8.2 for HPASCO and TFASCO, which indicate that annealing in both the cases yielded a similar result, proven through closeness of their phase lag plot trends. Annealing on a hot plane in an open environment caused the heat to be concentrated at the center. Due to the convective heat losses at the edges of the sample, the effect of annealing was significantly reduced, which was confirmed by observing a low thermal conductivity value 6.5 $Wm^{-1}K^{-1}$, compared to the 20.43 $Wm^{-1}K^{-1}$ for the central parts of the sample. Hence to verify the effects of annealing in air uniformly across the sample, similar kind of annealing was done in tube furnaces (TFASCO) which showed an average thermal conductivity value of 18.74 $Wm^{-1}K^{-1}$ across various locations on the sample. The difference maybe due to the subtle difference in the annealing procedures in the two methods described. Uncertainty of the fitted parameters can be be evaluated from the Fig. 8.5, where the uncertainty values are plotted with respect to the changing guesses for the SCO thin film thermal conductivity. The uncertainty in thermal conductivity measurements for SCO, HPASCO, POASCO and TFASCO is around 10% in all the cases. The uncertainty values for other fitted parameter remain unaffected by the changing SCO thin film thermal conductivity values.

The phase lag plot for the POASCO compared to HPASCO and TFASCO plots differs in a broader range of modulation frequency, pointing to the fact that the thermal conductivity values for POASCO would be different. This is what we exactly observe through our tabulated values for POASCO, that its thermal conductivity is lower than that of hot plate and tube furnace annealed SCO. An interesting fact to note is that annealing in an oxygen rich environment lead to lower thermal conductivity as compared to annealing in air.

This result seems strange as one would expect that annealing in an Oxygen rich environment would lead to addition of electron rich Oxygen atoms to the SCO thin film's surface, which should in theory increase the thermal conductivity of the sample due to the presence of higher number of free electrons.

However, it seems like the Oxygen atoms on the SCO surface act more like a scattering site, than an electron donor site. Annealing increases the thermal conductivity of un-annealed sam-

Table 8.2: Volumetric heat capacity and thermal conductivity of SCO-based films.

Material	C_p $(J\,m^{-3}K^{-1})$	k_{SCO} $(W\,m^{-1}K^{-1})$
HPASCO	1.46 (0.01)	20.43 (0.25)
POASCO	1.51 (0.03)	14.51 (1.05)
SCO	1.28 (0.02)	4.07 (0.11)
TFASCO	1.41 (0.02)	18.74 (0.50)

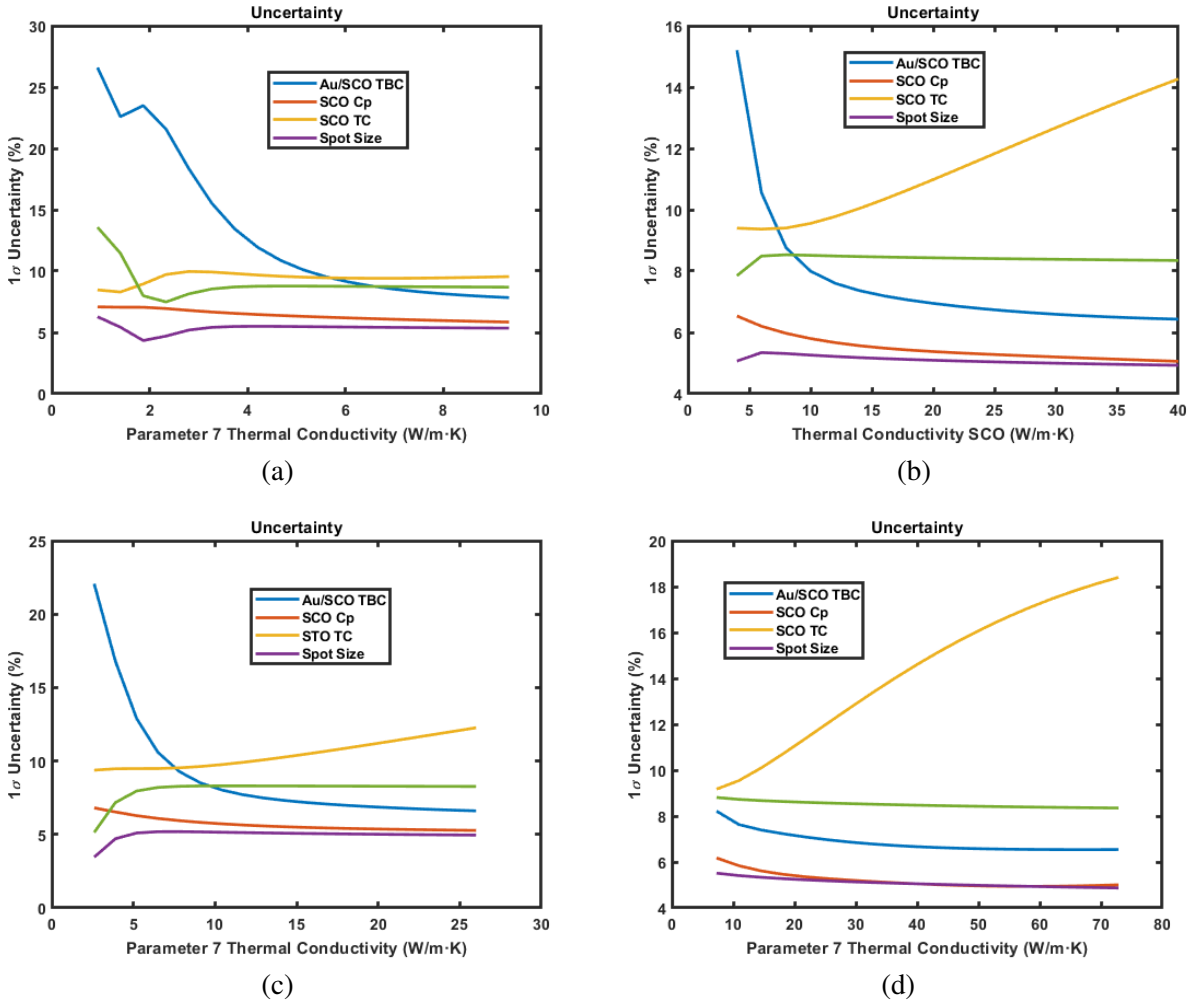

Figure 8.5: Uncertainty analysis of the fitted parameters, with respect to the variation in the thermal conductivity values of a) SCO b) HPASCO c) POASCO d) TFASCO

ple by 402%, 360% and 257% respectively for hot plate, tube furnace and pure Oxygen in tube furnace annealing environments, which is interesting to note. Electrical resistivity and carrier concentration measurement can shed some light by supplementing the arguments on why such a phenomena is observed in the measurement of thermal parameters, and to understand the correlation between electronic and thermal properties. This work to a certain extent supports the evidence of SCO thin films on LAO and LSAT substrates demonstrating metallic properties, when subjected to annealing[190].

8.4 Conclusions

Through this work, we were able to experimentally measure the thermal conductivity and volumetric heat capacity of SCO thin films prepared under various annealing environments. We measured the volumetric heat capacity for the un-annealed sample to be around 1.28 $Jm^{-3}K^{-1}$ and between 1.41 and 1.51 $Jm^{-3}K^{-1}$ for various annealed samples. Assuming a measurement error of 10% contributed by the FDTR system, the volumetric heat capacities of all the annealed samples seem to be in an agreement with each other, irrespective of the method of annealing.

We also measured the thermal conductivity values of the SCO thin films on Si substrate, which indicated that annealing substantially influenced the thermal conductivity values and the annealing environment determined how large the increment was. The mechanism of this increment needs to be understood well through analysis of micro structural changes using TEM, and through electrical measurements of resistivity and carrier concentrations. This will provide a holistic answer to the observed phenomena of SCO thin film exhibiting metallic behavior upon annealing.

Chapter 9

Conclusions

The work done in this dissertation demonstrates how the utilization of experimental thermoreflectance techniques—such as Frequency Domain Thermoreflectance (FDTR) and first-principles computational tools such as Quantum Espresso and ShengBTE can be used to examine and characterize the thermal properties of a different material systems. This approach can be applied to semiconductors, oxides, and intermetallic compounds, to name a few, to aid our understanding of heat transport phenomena across multiple length scales and material classes.

Our studies began with well-known gallium compounds: GaP, GaAs, and GaSb as a means to establish confidence in FDTR as a precision thermal measurement tool. As these materials' thermal properties have been extensively characterized, they provide a reliable baseline to solidify the procedure to extract thermal properties for this measurement tool. The FDTR-derived thermal conductivity of these compounds was shown to be consistent with literature values through measurements, sensitivity analyses, and optimized curve fitting. While also serving as a proof of concept for experimental methods, it was able to elucidate potential sources of error, and conditions that were required for accurate measurement readings, and allowed for an understanding of how the final extracted thermal properties could be affected by parameters like modulation frequency and transducer properties. This showed that FDTR, on a foundational basis, could be utilized as a method to characterize unexplored and uncharacterized materials systems while also aiding in the framework that could be used to interpret the remainder of the work.

We next applied the FDTR methodology to two compounds of interest in optoelectronics and thermoelectrics, Zinc Selenide (ZnSe) and Zinc Telluride (ZnTe). Our experimentally measured thermal conductivities (17 $Wm^{-1}K^{-1}$ for ZnSe and 14 $Wm^{-1}K^{-1}$ for ZnTe) were consistent with first-principles predictions (23.2 $Wm^{-1}K^{-1}$ and 13.72 $Wm^{-1}K^{-1}$at 300 K). Differences could be attributed to overall variations in polycrystallinity between experimental samples and computational

models. We also examined the length-dependent thermal conductivity of both of the above materials. We were able to observe a decrease in the thermal conductivity in both ZnSe and ZnTe when the length scale was reduced from micrometers to nanometers, further showing the effect of phonon–boundary scattering being present at modern device dimensions. The combination of FDTR and our first-principle results shows that experimental testing and our atomistic modeling can demonstrate how heat transfer is controlled at a basic physical level. This also shows that both of these tools can be used to apply theoretical ideas into practical applications.

We then did an examination of STO thin films at varying thicknesses to show FDTR's sensitivity to nanoscale thermal transport. Compared to the 12 $Wm^{-1}K^{-1}$ thermal conductivity value for the bulk single crystal STO, the thin film conductivity values for 200 nm, 80 nm, 50 nm, and 12 nm films were measured to be 7.4, 3.86, 2.35, and 0.8 $Wm^{-1}K^{-1}$ respectively, which could be a consequence of boundary scattering and substrate effects. A significant reduction of 93% from the bulk value was noticed for the 12 nm thin film. In a sensitivity analysis, FDTR measurements were shown to be sensitive to cross-plane thermal conductivity and volumetric heat capacity properties, which made their evaluation possible. This illustrated the underlying mechanisms of thermal transport in thin perovskite films. We can use this information to guide future experimental design as well as improve our understanding of phonon scattering in oxide thin-film systems especially those with silicon substrates.

Computational methods were applied to systematically predict the thermal transport phenomena in ReAlSi and ReGaSi, which are complex intermetallic compounds that have never previously had their thermal properties characterized. First-principles results of ReSi were compared to experimental measurements obtained with TDTR. These comparisons showed that the results from these methods were in close agreement with each other. We also examined the effect of biaxial compressive stress on the thermal conductivity in ReAlSi and ReGaSi. We examined how stress-induced modifications to phonon dispersions, lifetimes, and group velocities affected the thermal conductivity of the material. We noticed that the thermal conductivity of the material remained relatively unchanged due to the application of stress.

The final experimental chapter examined the effects of annealing of Strontium Chromate thin films under different environments — a process with limited literature due to the difficulty of computational modeling because of the strong electron correlations exhibited by the materials of this family. Measurements performed by FDTR showed that after annealing there were observable changes in thermal conductivity and heat capacity, that were consistent with observed electronic measurements that shows a transition towards metallic behavior. Further study is necessary to determine the microscopic origin of these changes but this work establishes a foundational background with regard to SCO thin films and the ability of FDTR to characterize thermally complex oxide systems grown on silicon, adding to the barely available literature.

Bibliography

[1] Moore G. Cramming more components onto integrated circuits. *Proc. IEEE*, 86:82–85, 1998. 1

[2] Minnich A, Johnson J, Schmidt A, Esfarjani K, Dresselhaus M, Nelson K, and Chen G. Thermal conductivity spectroscopy technique to measure phonon mean free paths. *Phys. Rev. Lett*, 107:95901, 2011. 1

[3] Due J and Robinson A. Reliability of thermal interface materials: A review. *Applied Thermal Engineering*, 50:455–463, 2013. 1

[4] Muthaiah R and Garg J. Strain tuned high thermal conductivity in boron phosphide at nanometer length scales - a first-principles study. *Phys. Chem. Chem. Phys*, 22:20914–20921, 2020. 1

[5] Muthaiah R and Garg J. Ultrahigh thermal conductivity in hexagonal bc6n-an efficient material for nanoscale thermal management-a first principles study. *Computational Materials Science*, page 110773, 0200. 1

[6] Cahill D. Analysis of heat flow in layered structures for time-domain thermoreflectance. *Review of Scientific Instruments*, 75:5119–5122, 2004. 1, 22

[7] Schmidt A, Cheaito R, and Chiesa M. A frequency-domain thermoreflectance method for the characterization of thermal properties. *Rev Sci Instrum*, 80:94901, 2009. 1, 2, 11, 80

[8] Cahill D G, Ford W K, Goodson K E, Mahan G D, Majumdar A, Maris H J, Merlin r, and Phillpot S R. Nanoscale thermal transport. *Journal of Applied Physics*, 93:793–818, 2003. 1

[9] Meneghesso G, Verzellesi G, Danesin F, Rampazzo F, Zanon F, Tazzoli A, Meneghini M, and Zanoni E. Reliability of gan high-electron-mobility transistors: State of the art and perspectives. *IEEE Transactions on Device and Materials Reliability*, 8:332–343, 2008. 1

[10] Shi L, Dames C, Lukes J, Reddy P, Duda J, Cahill D, Lee J, Marconnet A, Goodson K, Bahk J.-H, Shakouri A, Prasher R, Felts J, King W, Han B, and Bischof J. Evaluating broader impacts of nanoscale thermal transport research. *Nanoscale and Microscale Thermophysical Engineering*, 19:127–165, 2015. 1

[11] Cahill D, Goodson K, and Majumdar A. Thermometry and thermal transport in micro/nanoscale solid-state devices and structures. *Journal of Heat Transfer*, 124:223–241, 2001. 1

[12] Kwon O, Shi L, and Majumdar A. Scanning thermal wave microscopy (stwm). *Journal of Heat Transfer*, 125:156–163, 2003. 1

[13] Cahill D. Thermal conductivity measurement from 30 to 750 k: The 3ω method. *Review of Scientific Instruments*, 61:802–808, 1990. 1

[14] Paddock C and Eesley G. Transient thermoreflectance from thin metal films. *Journal of Applied Physics*, 60:285–290, 1986. 1, 2

[15] Capinski W and Maris H. Improved apparatus for picosecond pump and probe optical measurements. *Review of Scientific Instruments*, 67:2720–2726, 1996. 1

[16] Liu J. Simultaneous measurement of thermal conductivity and heat capacity of bulk and thin film materials using frequency-dependent transient thermoreflectance method. *Review of Scientific Instruments*, 84:34902, 2013. 2, 4

[17] Wei C, Zheng X, Cahill D, and Zhao J.-C. Invited article: Micron resolution spatially resolved measurement of heat capacity using dual-frequency time-domain thermoreflectance. *Review of Scientific Instruments*, 84:71301, 2013. 2

[18] Wilson O, Hu X, Cahill D, and Braun P. Colloidal metal particles as probes of nanoscale thermal transport in fluids. *Phys. Rev. B*, 66:224301, 2002. 2

[19] Schmidt A, Chen X, and Chen G. Pulse accumulation, radial heat conduction, and anisotropic thermal conductivity in pump-probe transient thermoreflectance. *Review of Scientific Instruments*, 79:114902, 2008. 2, 3

[20] Costescu R, Wall M, and Cahill D. Thermal conductance of epitaxial interfaces. *Phys. Rev. B*, 67:54302, 2003. 2

[21] Schmidt A, Cheaito R, and Chiesa M. Characterization of thin metal films via frequency-domain thermoreflectance. *Journal of Applied Physics*, 107:24908, 2010. 2, 4, 24

[22] Luckyanova M, Garg J, Esfarjani K, Jandl A, Bulsara M, Schmidt A, Minnich A, Chen S, Dresselhaus M, Ren Z, Fitzgerald E, and Chen G. Coherent phonon heat conduction in superlattices. *Science*, 338:936–939, 2012. 2

[23] Lyeo H.-K and Cahill D. Thermal conductance of interfaces between highly dissimilar materials. *Phys. Rev. B*, 73:144301, 2006. 2

[24] Hopkins P, Baraket M, Barnat E, Beechem T, Kearney S, Duda J, Robinson J, and Walton S. Manipulating thermal conductance at metal-graphene contacts via chemical functionalization. *Nano Lett*, 12:590–595, 2012. 2

[25] Yang J, Ziade E, Maragliano C, Crowder R, Wang X, Stefancich M, Chiesa M, Swan A, and Schmidt A. Thermal conductance imaging of graphene contacts. *Journal of Applied Physics*, 116:23515, 2014. 2, 4

[26] Hopkins P, Phinney L, Serrano J, and Beechem T. Effects of surface roughness and oxide layer on the thermal boundary conductance at aluminum/silicon interfaces. *Phys. Rev. B*, 82:85307, 2010. 2

[27] Rosencwaig A and Gersho A. Theory of the photoacoustic effect with solids. *Journal of Acoustical Society of America*, 58:S52, 1975. 2

[28] Rosencwaig A. Thermal wave imaging. *Science*, 218:223–228, 1982. 2

[29] Ospal J, Rosencwaig A, and Willenborg D. Thermal-wave detection and thin-film thickness measurements with laser beam deflection. *Applied Optics*, 22:3169–3176, 1983. 2

[30] Rosencwaig A, Ospal J, Smith W, and Willenborg D. Detection of thermal waves through optical reflectance. *Applied Physics Letters*, 46:1013–1015, 1985. 2

[31] Eesley G. Observation of nonequilibrium electron heating in copper. *Phys. Rev. Lett*, 51:2140–2143, 1983. 2

[32] Eesley G. Generation of nonequilibrium electron and lattice temperatures in copper by picosecond laser pulses. *Phys. Rev. B*, 33:2144–2151, 1986. 2

[33] Qiu T Q and Tien C L. Short-pulse laser heating on metals. *International Journal of Heat and Mass Transfer*, 35:719–726, 1992. 2

[34] Schmidt A. Pump-probe thermoreflectance. *Annual Review of Heat Transfer*, page 16, 2013. 2

[35] Burzo M, Komarov P, and Raad P. Minimizing the uncertainties associated with the measurement of thermal properties by the transient thermo-reflectance method. *IEEE Transactions on Components and Packaging Technologies*, 28:39–44, 2005. 3

[36] Yang J, Maragliano C, and Schmidt A. Thermal property microscopy with frequency domain thermoreflectance. *Review of Scientific Instruments*, 84:104904, 2013. 3, 8, 11, 23, 58, 73

[37] Collins K, Maznev A, Cuffe J, Nelson K, Chen, and G. Examining thermal transport through a frequency-domain representation of time-domain thermoreflectance data. *Review of Scientific Instruments*, 85:124903, 2014. 4

[38] Hopkins P, Serrano J, and Phinney L. Comparison of thermal conductivity and thermal boundary conductance sensitivities in continuous-wave and ultrashort-pulsed thermoreflectance analyses. *Int J Thermophys*, 31:2380–2393, 2010. 4

[39] Malen J, Baheti K, Tong T, Zhao Y, Hudgings J, and Majumdar A. Optical measurement of thermal conductivity using fiber aligned frequency domain thermoreflectance. *Journal of Heat Transfer*, 133, 2011. 4, 11

[40] Zhu J, Tang D, Wang W, Liu J, Holub K, and Yang R. Ultrafast thermoreflectance techniques for measuring thermal conductivity and interface thermal conductance of thin films. *Journal of Applied Physics*, 108:94315, 2010. 4

[41] Yang J. Thermal property measurement with frequency domain thermoreflectance. 2016. 8, 24, 80

[42] Santos F and E Hecht. Optics. 2002. 12

[43] Carslaw H and Jaeger J. *Conduction of Heat in Solids*, 1959. 14

[44] Seber, George A, and Wild C. Nonlinear regression. *Series in Probability and Statistics)*, page 16, 04 2023. 19

[45] Jennrich R. Asymptotic properties of non-linear least squares estimators. *The Annals of Mathematical Statistics*, 40:633–643, 1969. 21

[46] Jiang P, Qian X, and Yang R. A new elliptical-beam method based on time-domain thermoreflectance (tdtr) to measure the in-plane anisotropic thermal conductivity and its comparison with the beam-offset method. *Review of Scientific Instruments*, 89:94902, 2018. 23, 58, 73

[47] Jiang P, Qian X, and Yang R. Tutorial: Time-domain thermoreflectance (tdtr) for thermal property characterization of bulk and thin film materials. *Journal of Applied Physics*, 124:161103, 2018. 23

[48] Srivastava G P. The physics of phonons. *CRC Press*, 1990. 27, 41

[49] Peierls R. Quantum theory of solids. *Oxford University Press*, 1955. 37

[50] Dirac P A. The quantum theory of the emission and absorption of radiation. *Proceedings of the Royal Society of London. Series A Containing Papers of a Mathematical and Physical Character*, 114:243–265, 1927. 37

[51] Fermi E. Nuclear physics: a course given by enrico fermi at the university of chicago. *University of Chicago press*, 1950. 37

[52] Omini M and Sparavigna A. Beyond the isotropic-model approximation in the theory of thermal conductivity. *Physical Review B*, 53:9064, 1996. 41

[53] Broido D A, Ward A, and Mingo N. Lattice thermal conductivity of silicon from empirical interatomic potentials. *Physical Review B—Condensed Matter and Materials Physics*, 72:014308, 2005. 41

[54] Fermi Eiman J M and Levy P W. Electrons and phonons. 1961. 41

[55] Asen-Palmer M, Bartkowski K, Gmelin E, Cardona M, Zhernov A P, Inyushkin A V, Taldenkov A, Ozhogin V I, Itoh K M, and Haller E E. Thermal conductivity of germanium crystals with different isotopic compositions. *Physical review B*, 56:9431, 1997. 41

[56] Cao J X, Yan X H, Xiao Y, and Ding J W. Thermal conductivity of zigzag single-walled carbon nanotubes: Role of the umklapp process. *Physical Review B*, 69:073407, 2004. 41

[57] Khitun A and Wang K L. Modification of the three-phonon umklapp process in a quantum wire. *Applied Physics Letters*, 79:851–853, 2001. 41

[58] Monkhorst H and Pack J. Special points for brillouin-zone integrations. *Physical Review B*, 13:5188–5192, 1976. 45, 58, 89

[59] Giannozzi P. Quantum espresso: a modular and open-source software project for quantum simulations of materials. *Journal of Physics: Condensed Matter*, 21:395502, 2009. 45, 57, 89

[60] Dal Corso A, Baroni S, Resta R, and de Gironcoli S. Ab initio calculation of phonon dispersions in ii-vi semiconductors. *Physical Review B*, 47:3588, 1993. 45

[61] Lessio M and Carter E. What is the role of pyridinium in pyridine-catalyzed co2 reduction on p-gap photocathodes? *J. Am. Chem. Soc*, 137:13248–13251, 2015. 46

[62] Li Y, Liu J, Xiao N, Yu L, Zhang J, Ning P, Zhang Z, and Niu P. Electrical transport properties of gallium phosphide under high pressure. *Physica Status Solidi B-Basic Solid State Physics*, 257:1900470, 2020. 46

[63] Haq B, Ahmed R, Mohamad M, Shaari A, Rhee J, Alfaify S, Kanoun M, and Goumri-Said S. Engineering of highly mismatched alloy with semiconductor and semi-metallic substituent's for photovoltaic applications. *Current Applied Physics*, 17:162–168, 2017. 46

[64] Belabbes A and Bechstedt F. Forbidden band-edge excitons of wurtzite-gap: A theoretical view. *physica status solidi (b)*, 256:1800238, 2019. 46

[65] Ahmed R, Fazal-E-Aleem, Hashemifar S, Akbarzadeh, and H. First-principles study of the structural and electronic properties of iii-phosphides. *Physica B Condensed Matter*, 403:1876–1881, 2008. 46

[66] Zhang Z, Chai C, Song Y, Kong L, Yang, and Y. A dft study on physical properties of iii-v compounds (aln, gan, alp, and gap) in the p3121 phase. *Mater. Res. Express*, 8:25908, 2021. 46

[67] Assali S, Zardo I, Plissard S, Kriegner D, Verheijen M, Bauer G, Meijerink A, Belabbes A, Bechstedt F, Haverkort J, and Bakkers E. Direct band gap wurtzite gallium phosphide nanowires. *Nano Lett*, 13:1559–1563, 2013. 46

[68] Panish M and Casey H. Temperature dependence of the energy gap in gaas and gap. *Journal of Applied Physics*, 40:163–167, 1969. 46

[69] Arbouche O, Belgoumène B, Soudini B, Azzaz Y, Bendaoud H, Amara, and K. First-principles study on structural properties and phase stability of iii-phosphide (bp, gap, alp and inp). *Computational Materials Science*, 47:685–692, 2010. 46

[70] Shan W, Walukiewicz W, Yu K, Wu J, Ager J, Haller E, Xin H, and Tu C. Nature of the fundamental band gap in ganxp1-x alloys. *Appl. Phys. Lett*, 76:3251–3253, 2000. 46

[71] Yeh C.-Y, Wei S.-H, and Zunger A. Relationships between the band gaps of the zinc-blende and wurtzite modifications of semiconductors. *Phys. Rev. B*, 50:2715–2718, 1994. 46

[72] Humphreys R, Rössler U, and Cardona M. Indirect exciton fine structure in gap and the effect of uniaxial stress. *Phys. Rev. B*, 18:5590–5605, 1978. 46

[73] Lorenz M, Pettit G, and Taylor R. Band gap of gallium phosphide from 0 to 900k and light emission from diodes at high temperatures. *Phys. Rev*, 171:876–881, 1968. 46

[74] Aparna A, Brahmajirao V, and Karthikeyan T. Review on synthesis and characterization of gallium phosphide. *Procedia Materials Science*, 6:1650–1657, 2014. 46

[75] Shi F, Chang K.-L, Epple J, Xu C.-F, Cheng K, and Hsieh K. Characterization of gaas-based n-n and p-n interface junctions prepared by direct wafer bonding. *Journal of Applied Physics*, 92:7544–7549, 2002. 46

[76] Czaban J, Thompson D, and Lapierre R. Gaas core-shell nanowires for photovoltaic applications. *Nano Lett*, 9:148–154, 2009. 46

[77] Zhou Y, Zhu Z, Crouse D, and Lo Y. Electrical properties of wafer-bonded gaas/si heterojunctions. *Appl. Phys. Lett*, 73:2337–2339, 1998. 46

[78] Yang X, Jurkovic M, Heroux J, and Wang W. Molecular beam epitaxial growth of ingaasn:sb/gaas quantum wells for long-wavelength semiconductor lasers. *Appl. Phys. Lett*, 75:178–180, 1999. 46

[79] Schnitzer I, Yablonovitch E, Caneau C, Gmitter T, and Scherer A. 30% external quantum efficiency from surface textured, thin film light emitting diodes. *Appl. Phys. Lett*, 63:2174–2176, 1993. 46

[80] Motosugi G and Kagawa T. Temperature dependence of the threshold current of algaassb/gasb dh lasers. *Jpn. J. Appl. Phys*, 19:2303, 1980. 46

[81] Morosini M, Herrera-Perez J, Loural M, Von Zuben A, Da Silveira A, and Patel N. Low-threshold gainassb/gaalassb double-heterostructure lasers grown by lpe. *IEEE Journal of Quantum Electronics*, 29:2103–2108, 1993. 46

[82] Hildebrand O, Kuebart W, Benz K, and Pilkuhn M. Ga1-xalxsb avalanche photodiodes: Resonant impact ionization with very high ratio of ionization coefficients. *IEEE Journal of Quantum Electronics*, 17:284–288, 1981. 46

[83] Segawa K, Miki H, Otsubo M, Shirahata K, and Fujibayashi K. Coherent gunn oscillations in gaxin1-xsb. *Electronics Letters*, 12:124–125, 1976. 46

[84] Hilsum C and Rees H. Three-level oscillator: A new form of transferred-electron device. *Electronics Letters*, 6:277–278, 1970. 46

[85] Esaki L. Inas-gasb superlattices-synthesized semiconductors and semimetals. *Journal of Crystal Growth*, 52:227–240, 1981. 46

[86] MTI Corp Inc. *mtixtl.com*. 47, 64, 82

[87] Ding J, Liu C, Xi L, Xi J, and Yang J. Thermoelectric transport properties in chalcogenides znx (x = s, se): From the role of electron-phonon couplings. *Journal of Materiomics*, 7:310–319, 2021. 56

[88] Zhang H and Fang Y. Temperature dependent photoluminescence of surfactant assisted electrochemically synthesized znse nanostructures. *Journal of Alloys and Compounds*, 781:201–208, 2019. 56

[89] Khan T, Mehmood M, Mahmood A, Shah A, Raza Q, Iqbal A, and Aziz U. Synthesis of thermally evaporated znse thin film at room temperature. *Thin Solid Films*, 519:5971–5977, 2011. 56

[90] Lugueva N, Luguev S, and Dunaev A. Thermal conductivity of polycrystalline zinc selenide. *Phys. Solid State*, 45:449–452, 2003. 56, 59

[91] Chandramohan R, Sanjeevaraja C, and Mahalingam T. Preparation of zinc selenide thin films by electrodeposition technique for solar cell applications -chandramohan -1997 - physica status solidi (a) -wiley online library. *Physica Status Solidi*, 163:R11–R12, 2001. 56

[92] Morkoç H, Strite S, Gao G, Lin M, Sverdlov B, and Burns M. Large-band-gap sic, iii-v nitride, and ii-vi znse-based semiconductor device technologies. *Journal of Applied Physics*, 76:1363–1398, 1994. 56

[93] Li P and He T. Recent advances in zinc chalcogenide-based nanocatalysts for photocatalytic reduction of co2. *J. Mater. Chem. A*, 9:23364–23381, 2021. 56

[94] Langer D and Vesely C. Electronic core levels of zinc chalcogenides. *Phys. Rev. B*, 2:4885–4892, 1970. 56

[95] Gangadharan R, Jayalakshmi V, Kalaiselvi J, Mohan S, Murugan R, and Palanivel B. Electronic and structural properties of zinc chalcogenides znx (x=s, se, te. *Journal of Alloys and Compounds*, 359:22–26, 2003. 56

[96] Sun Y. Fabrication of flexible and freestanding zinc chalcogenide single layers. *Nature communications*, 3:1–7, 2012. 56

[97] Davami K. Thermal conductivity of znte nanowires. *Journal of Applied Physics*, 114:134314, 2013. 56

[98] Broido D A, Lindsay L, and Reinecke T. Ab initio study of the unusual thermal transport properties of boron arsenide and related materials. *Physcial Review B*, 88:214303, 2013. 56

[99] Broido D A, Malorny M, Birner G, Mingo N, and Stewart D A. Intrinsic lattice thermal conductivity of semiconductors from first principles. *Applied Physics Letters*, 91:231922, 2007. 56

[100] Garg J, Bonini N, Kozinsky B, and Marzari N. Role of disorder and anharmonicity in the thermal conductivity of silicon-germanium alloys: A first-principles study. *Physical Review Letters*, 106:45901, 2011. 56

[101] Paulatto L. First-principles calculations of phonon frequencies, lifetimes, and spectral functions from weak to strong anharmonicity: The example of palladium hydrides. *Physical Review B*, 91:54304, 2015. 57, 58, 89

[102] Paulatto L, Mauri F, and Lazzeri M. Anharmonic properties from a generalized third-order ab initio approach: Theory and applications to graphite and graphene. *Physical Review B*, 87:214303, 2013. 57, 58, 89

[103] Fugallo G. Ab initio variational approach for evaluating lattice thermal conductivity. *Physical Review B*, 88:45430, 2013. 57, 58, 89

[104] Ceperley D and Alder B. Ground state of the electron gas by a stochastic method. *Physical Review Letters*, 45:566–569, 1980. 57

[105] Garg J, Bonini N, and Marzari N. First-principles determination of phonon lifetimes, mean free paths, and thermal conductivities in crystalline materials: Pure silicon and germanium. *Length-Scale Dependent Phonon Interactions*, pages 115–136, 2014. 58

[106] Casimir H. Note on the conduction of heat in crystals. *Physica*, 5:495–500, 1938. 58, 59

[107] Jiang P, Qian X, and Yang R. Tutorial: Time-domain thermoreflectance (tdtr) for thermal property characterization of bulk and thin film materials. *Journal of Applied Physics*, 124:161103, 2018. 58, 73

[108] Haynes W. Crc handbook of chemistry and physics. 2011. 59

[109] Hao Q, Xiao Y, and Chen Q. Determining phonon mean free path spectrum by ballistic phonon resistance within a nanoslot-patterned thin film. *Materials Today Physics*, 10:100126, 2019. 60

[110] Hao Q and Garg J. A review on phonon transport within polycrystalline materials. *ES Materials and Manufacturing*, 14:36–50, 2021. 63

[111] Brooks C M, Wilson R B, Schäfer A, Mundy J A, Holtz M E, Muller D A, Schubert J, Cahill D G, and Schlom D G. Tuning thermal conductivity in homoepitaxial srtio3 films via defects. *Applied Physics Letters*, 107:051902, 2015. 69, 71

[112] Imada M, Fujimori A, and Tokura Y. Metal-insulator transitions. *Reviews of Modern Physics*, 70:1039, 1998. 69

[113] Coey J, von Viret M, and Von Molnar S. Mixed-valence manganites. *Advances in Physics*, 48:167–293, 1999. 69

[114] Dawber M, Rabe K, and Scott J. Physics of thin-film ferroelectric oxides. *Review of Modern Physics*, 77:1083–1130, 2005. 69

[115] Onishi T, Lippmaa M, Yamamoto T, Meguro S, and Koinuma H. Improved stoichiometry and misfit control in perovskite thin film formation at a critical fluence by pulsed laser deposition. *Applied Physics Letters*, 87:241919, 2005. 69

[116] Nakagawa N, Hwang H, and Muller D. Why some interfaces cannot be sharp. *Nature Mater*, 5:204–209, 2006. 69

[117] Varela M, Findlay S, Lupini A, Christen H, Borisevich A, Dellby N, Krivanek O, Nellist P, Oxley M, Allen L, and Pennycook S. Spectroscopic imaging of single atoms within a bulk solid. *Phys. Rev. Lett*, 92:95502, 2004. 69

[118] Lippmaa M, Nakagawa N, Kawasaki M, Ohashi S, and Koinuma H. Growth mode mapping of srtio3 epitaxy. *Applied Physics Letters*, 76:2439–2441, 2000. 69

[119] Vassen R, Cao X, Tietz F, Basu D, and Stöver D. Zirconates as new materials for thermal barrier coatings. *Journal of the American Ceramic Society*, 83:2023–2028, 2000. 69

[120] Fergus J. Oxide materials for high temperature thermoelectric energy conversion. *Journal of the European Ceramic Society*, 32:525–540, 2012. 69

[121] Weidenkaff A, Robert R, Aguirre M, Bocher L, Lippert T, and Canulescu S. Development of thermoelectric oxides for renewable energy conversion technologies. *ScienceDirect*, 33:342–347, 2008. 69

[122] Sun J, Singh D, and Mater. Thermoelectric properties of n-type srtio3. *APL Materials*, 4:104803, 2016. 69

[123] Shi X.-L, Wu H, Liu Q, Zhou W, Lu S, Shao Z, Dargusch M, and Chen Z.-G. Srtio3-based thermoelectrics: Progress and challenges. *Nano Energy*, 78:105195, 2020. 69

[124] Lesaicherre P-Y, Yamaguchi H, Miyasaka Y, Watanabe H, Ono H, and Yoshida M. Srtio3 thin films by mocvd for 1 gbit dram application. *Integrated Ferroelectrics*, 8:201–225, 1995. 70

[125] Kiyotoshi M and Eguchi K. Ultrathin srtio3 films prepared by chemical vapor deposition on nb doped srtio3 substrates. *Applied Physics Letters*, 67:2468–2470, 1995. 70

[126] Wilk G, Wallace M, and Anthony J. High-κ gate dielectrics: Current status and materials properties considerations. *Journal of Applied Physics*, 89:5243–5275, 2001. 70

[127] Shin D S, Park S T, Choi H S, Choi I H, and Lee J Y. Characteristics of pt/srtio3/pb(zr0.52, ti0.48)o3/srtio3/si ferroelectric gate oxide structure. *Thin Solid Films*, 354:251–255, 1999. 70

[128] Qiao J, Yang, and C. High-tc superconductors on buffered silicon: Materials properties and device applications. *Materials Science and Engineering: R: Reports*, 14:157–201, 1995. 70

[129] Leskelä M, Mölsä H, and Niinistö L. Chemical vapour deposition of high-tc superconducting thin films. *Supercond. Sci. Technol*, 6:627, 1993. 70

[130] Seijas-Bellido J, Escorihuela-Sayalero C, Royo M, Ljungberg M, Wojdeł J, Íñiguez J, and Rurali R. A phononic switch based on ferroelectric domain walls. *Phys. Rev. B*, 96:140101, 2017. 70

[131] Royo M, Escorihuela-Sayalero C, Íñiguez J, and Rurali R. Ferroelectric domain wall phonon polarizer. *Phys. Rev. Mater*, 1:51402, 2017. 70

[132] Ihlefeld J, Foley B, Scrymgeour D, Michael J, McKenzie B, Medlin D, Wallace Margeaux, Trolier-McKinstry S, and Hopkins P. Room-temperature voltage tunable phonon thermal conductivity via reconfigurable interfaces in ferroelectric thin films nano letters. *Nano Letters*, 15:1791–1795, 2015. 70

[133] Hopkins P, Adamo C, Ye L, Huey B, Lee S, Schlom D, and Ihlefeld J. Effects of coherent ferroelastic domain walls on the thermal conductivity and kapitza conductance in bismuth ferrite. *Applied Physics Letters*, 102:121903, 2013. 70

[134] Ning S, Huberman S, Zhang C, Zhang Z, Chen G, and Ross C. Dependence of the thermal conductivity of bifeo3 thin films on polarization and structure. *Phys. Rev. Appl*, 8:54049, 2017. 70

[135] Langenberg E, Saha D, Holtz M, Wang J.-J, Bugallo D, Ferreiro-Vila E, Paik H, Hanke I, Ganschow S, Muller D, Chen L.-Q, Catalan G, Domingo N, Malen J, Schlom D, and Rivadulla F. Ferroelectric domain walls in pbtio3 are effective regulators of heat flow at room temperature. *Nano Lett*, 19:7901–7907, 2019. 70

[136] Torres P, Iniguez J, and Rurali R. Giant electrophononic response in pbtio3 by strain engineering. *Phys. Rev. Lett*, 123:185901, 2019. 70

[137] Oh D.-W, Ravichandran J, Liang C.-W, Siemons W, Jalan B, Brooks C, Huijben M, Schlom D, Stemmer S, Martin L, Majumdar A, Ramesh R, and Cahill D G. Thermal conductivity as a metric for the crystalline quality of srtio3 epitaxial layers. *Applied Physics Letters*, 98, 2011. 70

[138] Sarantopoulos A, Saha D, Ong W.-L, Magén C, Malen J, and Rivadulla F. Reduction of thermal conductivity in ferroelectric srtio3 thin films. *Physical Review Materials*, 4:54002, 2020. 70

[139] Katsufuji T, Saiki T, Okubo S, Katayama Y, and Ueno K. Thermal conductivity of srvo3srtio3 thin films: Evidence of intrinsic thermal resistance at the interface between oxide layers. *Physical Review Materials*, 2:51002, 2018. 71

[140] Bugallo D, Langenberg E, Carbó-Argibay E, Varel Dominguez N, Fumega A O, Pardo V, Lucas I, Morellón, and Rivadulla F. Tuning coherent-phonon heat transport in lacoo3/srtio3 superlattices. *The Journal of Physical Chemistry Letters*, 12:11878–11885, 2021. 71

[141] Kumar SRS, Barasheed A Z, and Alshareef H N. High temperature thermoelectric properties of strontium titanate thin films with oxygen vacancy and niobium doping. *ACS Applied Materials and Interfaces*, 5:7268–7273, 2013. 71

[142] Yu C, Scullin M L, Huijben M, Ramesh R, and Majumdar A. Thermal conductivity reduction in oxygen-deficient strontium titanates. *Applied Physics Letters*, 92:191911, 2008. 71

[143] Foley B, Brown-Shaklee H, Duda J, Cheaito R, Gibbons B, Medlin D, Ihlefeld J, and Hopkins P. Thermal conductivity of nano-grained srtio3 thin films. *Applied Physics Letters*, 101:231908, 2012. 71

[144] Breckenfeld E, Wilson R, Karthik J, Damodaran A, Cahill D, and Martin L. Effect of growth induced (non)stoichiometry on the structure, dielectric response, and thermal conductivity of srtio3 thin films. *Chemistry of Materials*, 24:331–337, 2012. 72

[145] Zhang L, Li N, Wang H.-Q, Zhang Y, Ren F, Liao X.-X, Li Y.-P, Wang X.-D, Huang Z, and Dai Y. Tuning the thermal conductivity of strontium titanate through annealing treatments. *Chinese Physics B*, 26:016602, 2017. 72

[146] Wiedigen S, Kramer T, Feuchter M, Knorr I, Nee N, Hoffmann J, Kamlah M, Volkert C, and Jooss C. Interplay of point defects, biaxial strain, and thermal conductivity in homoepitaxial srtio3 thin films. *Applied Physics Letters*, 100:061904, 2012. 72

[147] Fumega A, Fu Y, Pardo V, and Singh D. Understanding the lattice thermal conductivity of srtio 3 from an ab initio perspective. *Physical Review Materials*, 4:33606, 2020. 72

[148] Martelli V, Jiménez J, Continentino M, Baggio-Saitovitch E, and Behnia K. Thermal transport and phonon hydrodynamics in strontium titanate. *Physics Review Letters*, 120:125901, 2018. 72

[149] Mckee R, Walker F, and Chisholm M. Crystalline oxides on silicon: the first five monolayers. *Physical Review Letters*, 81:3014–3017, 1998. 72

[150] Kumah D, Ngai J, and Kornblum L. Epitaxial oxides on semiconductors: from fundamentals to new devices. *Advanced Functional Materials*, 30:1901597, 2020. 72

[151] Lim Z, Quackenbush N, Penn A, Chrysler M, Bowden M, Zhu Z, Ablett J, Lee T.-L, Lebeau, Woicik J, Sushko P, Chambers S, and Ngai J. Charge transfer and built-in electric fields between a crystalline oxide and silicon. *Physical Review Letters*, 123:026805, 2019. 72

[152] Muthaiah R, Annam R, Tarannum F, Gupta A, Garg J, and Arafin S. Length dependence thermal conductivity of zinc selenide (znse) and zinc telluride (znte)–a combined first principles and frequency domain thermoreflectance (fdtr) study. *Physical Chemistry Chemical Physics*, 24:28814–28824, 2022. 76

[153] Pamato M, Wood I, Dobson D, Hunt S, and Vočadlo L. The thermal expansion of gold: point defect concentrations and pre-melting in a face-centred cubic metal. *Journal of Applied Crystallography*, 51:470–480, 2018. 76

[154] Coughlin J and Orr R. High temperature heat contents of meta-and orthotitanates of barium and strontium. *J. Am. Chem. Soc*, 75:530–531, 1953. 78

[155] De Ligny D and Richet P. High-temperature heat capacity and thermal expansion of srtio3 and srzro3 perovskites. *Phys. Rev. B*, 53:3013–3022, 1996. 78

[156] Mccalla E, Gastiasoro M, Cassuto G, Fernandes R, and Leighton C. Low-temperature specific heat of doped : Doping dependence of the effective mass and kadowaki-woods scaling violation. *Physical Review Materials*, 3:022001, 2019. 78

[157] Malen J, Baheti K, Tong T, Zhao Y, Hudgings J, and Majumdar A. Optical measurement of thermal conductivity using fiber aligned frequency domain thermoreflectance. *Journal of Heat Transfer*, 133:081601, 2011. 80

[158] Shen X, Ahmadi-Majlan K, Ngai J, Wu D, and Su D. Interfacial structure in epitaxial perovskite oxides on (001) ge crystal. *Applied Physics Letters*, 106:32903, 2015. 82

[159] Chrysler M, Gabel J, Lee T.-L, Penn A, Matthews B, Kepaptsoglou D, Ramasse Q, Paudel J, Sah R, Grassi J, Zhu Z, Gray A, Lebeau J, Spurgeon S Chambers S, Sushko P, and Ngai J. Tuning band alignment at a semiconductor-crystalline oxide heterojunction via electrostatic modulation of the interfacial dipole. *Physical Review Materials*, 5:104603, 2021. 82

[160] Shiau F Y, Cheng H C, and Chen L J. Localized epitaxial growth of crsi2 on silicon. *Journal of Applied Physics*, 59:2784–2787, 1986. 86

[161] Fathauer R W, Grunthaner P J, Lin T L, Chang K T, Mazur J H, and Jamieson D N. Molecular-beam epitaxy of crsi2 on si(111). *Journal of Vacuum Science Technology B*, 6:708–712, 1988. 86

[162] Vining C B. *Proceedings of 9th ICT, Pasadena*, page 249, 1990. 86

[163] Tanaka K, Inui H, Ohba T, Tsutsui S, and Mizumaki M. Crystallographic features of rhenium disilicide. *MRS Online Proceeding Library*, 793:332–337, 2003. 86, 87

[164] Rowe D M. Crc handbook of thermoelectrics. *CRC Press*, 1995. 86

[165] Nolas G, Cohn J L, Slack G A, and Schujman S B. Semiconducting ge clathrates: Promising candidates for thermoelectric applications. *Applied Physics Letters*, 73:178–180, 1998. 86

[166] Nolas G S, Sharp J, and Goldsmid J. Thermoelectrics: basic principles and new materials developments. *Springer Science & Business Media*, 2001. 86

[167] Becker J P, Mahan J E, and Long R G. Resi2 thin-film infrared detectors. *Journal of Vacuum Science & Technology A: Vacuum, Surfaces, and Films*, 13:1133–1135, 1995. 86

[168] Nesphor V S and Samsonov G V. *Physics of Metals and Metallography*, 11:146, 1960. 86, 87

[169] Jorda J L, Ishikawa M, and Muller J. Phase relations and superconductivity in the binary re-si system. *Journal of the Less Common Metals*, 13:27–35, 1982. 86, 87

[170] Siegrist T, Hulliger F, and Travaglini G. The crystal structure and some properties of resi2. *Journal of the Less Common Metals*, 92:119–129, 1983. 86, 87

[171] Gottlieb U, Lambert-Andron B, Nava F, Affronte M, Laborde O, Rouault A, and Madar R. Structural and electronic transport properties of resi2 single crystals. *Journal of applied physics*, 78:3902–3907, 1995. 86, 87

[172] Gu J J, Kuwabara K, Inui H Tanaka K, Yamaguchi M, Yamamoto A, Ohta T, and Obara H. Crystal structure and thermoelectric properties of resi1.75 silicide. *Materials Research Society Symposium Proceedings*, pages 501–506, 2003. 86, 87

[173] Long R G, Bost M C, and Mahan J E. Optical and electrical properties of semiconducting rhenium disilicide thin films. *Thin Solid Films*, 162:29–40, 1988. 86

[174] Bhattacharyya B K, Bylander D M, and Kleinman L. Fully relativistic energy bands and cohesive energy of resi2. *Physical Review B*, 33:3947, 1986. 86

[175] Ito S. *Material Science Engineering*, B36:37, 1990. 86

[176] Kuwabara K, Inui H, and Yamaguchi M. Microstructure and electrical properties of thin films of resi1. 75 produced by co-sputtering. *Intermetallics*, 10:129–138, 2002. 87

[177] Misra A, Chu F, and Mitchell T E. Incommensuration and other structural anomalies in rhenium disilicide. *Philosophical Magazine A*, 79:1411–1422, 1999. 87

[178] Shaposhnikov V L, Krivosheeva A V, Ivanenko L I, Filonov A B, Borisenko V E, Rebien M, Henrion W, Migas D B, Miglio L, Behr G, and Schumann J. Structural, electronic and optical properties of semiconducting rhenium silicide. *Journal of Physics: Condensed Matter*, 16:303, 2004. 87

[179] Decocq V. Doping effects on transition-metal silicides: Crystal structures and physical properties of aluminium doped rhenium silicide. *Graduate Theses/Dissertations. 3563. https://bearworks.missouristate.edu/theses/3563*, 2020. 87, 88

[180] Xie W, Gustin L, and Bian G. 111-type semiconductor regasi follows 14e–rules. *Inorganic Chemistry*, 59:5165–5172, 2017. 88

[181] Mihalkovič M, Krajčí M, and Widom M. Prediction of stable insulating intermetallic compounds. *Physical Review B—Condensed Matter and Materials Physics*, 87:100201, 2012. 88

[182] Wu Li, Jesús Carrete, Nebil A. Katcho, and Natalio Mingo. ShengBTE: a solver of the Boltzmann transport equation for phonons. *Comp. Phys. Commun.*, 185:1747–1758, 2014. 89

[183] Scudder M R, He B, Wang Y, Rai A, Cahill D G, Windl W, Heremans J P, and Goldberger J E. Highly efficient transverse thermoelectric devices with re4si7 crystals. *Energy & Environmental Science*, 14:4009–4017, 2021. 102

[184] Imada M, Fujimori A, and Tokura Y. Metal-insulator transitions. *Rev. Mod. Phys*, 70:1039–1263, 1998. 109

[185] Coey J, Viret M, and Molnár S. Mixed-valence manganites. *Advances in Physics*, 48:167–293, 1999. 109

[186] Lee P A, Nagaosa N, and Wen X G. Doping a mott insulator: Physics of high-temperature superconductivity. *Reviews of modern physics*, 78:17–85, 2006. 109

[187] Hwang H Y, Iwasa Y, Kawasaki M, Keimer B, Nagaosa N, and Tokura Y. Emergent phenomena at oxide interfaces. *Nature Materials*, 11:103–113, 2012. 109

[188] Anisimov V I, Aryasetiawan F, and Lichtenstein A I. First-principles calculations of the electronic structure and spectra of strongly correlated systems: the lda+ u method. *Journal of Physics: Condensed Matter*, 9:1997, 2012. 109

[189] Kalinin S V and Spaldin N A. Functional ion defects in transition metal oxides. *Journal of Physics: Condensed Matter*, 341:858–859, 2013. 109

[190] Zhang K H, Du Y, Sushko P V, Bowden M E, Shutthanandan V, Qiao L, Cao G X, Gai Z, Sallis S, Piper L F, and Chambers S A. Electronic and magnetic properties of expitaxial perovskit srcro3 - 0 0 1. *Journal of Physics: Condensed Matter*, 27:245605, 2015. 119